Deliverable D8.9:

“Behaviour of doped UO_2-based model materials as analogues for spent nuclear fuel under interim storage conditions”

Work Package WP8

This project has received funding from the European Union’s Horizon 2020 research and innovation programme under grant agreement N°847593.

Document information

Project Acronym	**EURAD**
Project Title	**European Joint Programme on Radioactive Waste Management**
Project Type	**European Joint Programme (EJP)**
EC grant agreement No.	**847593**
Project starting / end date	**1st June 2019 – 30 May 2024**
Work Package No.	**8**
Work Package Title	**Spent Fuel Characterization and Evolution Until Disposal**
Work Package Acronym	**SFC**
Deliverable No.	**8.9**
Deliverable Title	**Behaviour of doped UO_2-based model materials as analogues for spent nuclear fuel under interim storage conditions**
Lead Beneficiary	**CIEMAT**
Contractual Delivery Date	**M60**
Actual Delivery Date	**M60**
Type	**Report**
Dissemination level	**PU**
Authors	**N. Rodríguez-Villagra (CIEMAT), N. Dacheux (ICSM / CNRS); D. Prieur (HZDR); M. France Barthe (CEMHTI/CNRS); M.L. Amany (CEMHTI/CNRS); L. Anta (CIEMAT); L.J. Bonales (CIEMAT); E. De Bona (HZDR, JRC); L. Claparède (ICSM / CNRS); P. Desgardin (CEMHTI/CNRS); S. Durán (CIEMAT); J.M. Elorrieta (CIEMAT); S. Fernández-Carretero (CIEMAT); H. Galán (CIEMAT); L. Gutiérrez (CIEMAT); C. Hennig (HZDR); H. Imbert (ICSM / CNRS); J. Joseph (CEMHTI/CNRS); J. Lomonaco (CEMHTI/CNRS); A. Milena-Pérez (CIEMAT) A. Núñez (CIEMAT); R. Podor (ICSM / CNRS); D. Popov (CEMHTI/CNRS); T. Sauvage (CEMHTI/CNRS); R. Sarrazin (CEMHTI/CNRS); S. Szenknect (ICSM / CNRS); O. Walter (JRC);O. Wendling (CEMHTI/CNRS)**

To be cited as:

Rodríguez-Villagra, N. et al. (2024): Behaviour of doped UO_2-based model materials as analogues for spent nuclear fuel under interim storage conditions. Final version as of 31.05.2024 of deliverable D8.9 of the HORIZON 2020 project EURAD. EC Grant agreement no: 847593.

Disclaimer

Acknowledgement

This document is a deliverable of the European Joint Programme on Radioactive Waste Management (EURAD). EURAD has received funding from the European Union's Horizon 2020 research and innovation programme under grant agreement No 847593.

Status of deliverable		
	By	Date
1st draft	Mª Nieves Rodriguez-Villagra (CIEMAT) Nicolas Dacheux (CNRS) Damien Prieur (HZDR) Marie-France Barthe (CNRS-orleans)	24/10/2023
2nd draft	Mª Nieves Rodriguez-Villagra (CIEMAT) Damien Prieur (HZDR) Marie-France Barthe (CNRS-orleans) Nicolas Dacheux (CNRS)	12/02/2024
1st Review	Mª Nieves Rodriguez-Villagra (CIEMAT) Damien Prieur (HZDR) Marie-France Barthe (CNRS-orleans) Nicolas Dacheux (CNRS)	18/04/2024
Delivered (Lead Beneficiary)	CIEMAT	12/02/2024
Verified (WP Leader)	SKB	31/05/2024
Approved (PMO)	Paul Carbol	19/04/2024
Submitted to EC	Andra (Coordinator)	03/06/2024

Executive Summary

The broader scope of the work package 8 “Spent Fuel Characterization” (SFC) is to reduce uncertainties in spent fuel properties in predisposal phase. Particularly, it aims to understand the behaviour of fuel and ageing effect under normal and postulated accident scenarios until disposal, in order to identify relevant or typical bounding cases at time of reconditioning and predisposal activities (treatment, conditioning and transport).

According to currently available SNF interim storage concepts in Europe, the subtask 3.2 concentrates on the study of two experimental systems, in either dry-type” (casks, silos, niches and vaults)” or “wet-type” (pools)“[1]. These R&D activities are of crucial importance and allow to study the impact of the operation of short (few decades) and long-term (several decades to a few hundred years) storage conditions expected in SNF matrix behaviour, especially regarding high burnup and MOX spent fuels [1].

The subtask 3.2 focuses on the behaviour of simulated SNF pellets both under (ab-) normal dry interim storage conditions and under conditions of water contact, *i.e.* container or cladding failure scenarios, respectively. The main concern is to contribute on the operational safety of interim storage facilities by providing new insights on the ageing and degradation mechanisms of the SNF (*e.g.* He build-up, oxidation of the SNF, influence of the various fission products, etc.). The potential evolution of the SNF in case of mal operations conditions (*e.g.* moisture, aqueous dissolution of the UO_2 matrix, corrosion of the SNF, etc.) is also considered. Cutting-edge synchrotron methods at the Rossendorf beamline (*i.e.* high-resolution diffraction, x-ray absorption spectroscopy and x-ray emission spectroscopies) is performed to understand these degrading mechanisms at the atomic level.

Thus, obtaining quantitative data about ageing and degradation processes of the SNF is a particularly important issue. Different organisations are involved in this subtask: Centro de Investigaciones Energéticas, Medioambientales y Tecnológicas (CIEMAT), Institut de chimie séparative de Marcoule / Centre national de la recherche scientifique (ICSM/CNRS), Helmholtz-Zentrum Dresden-Rossendorf (HZDR) and Conditions Extrêmes et Matériaux : Haute Température et Irradiation / Centre national de la recherche scientifique (CEMHTI/CNRS).

This deliverable gives a detailed overview of information available about the following experimental campaigns:

- Dry storage experiments:
    - UO_2 and Eu-doped UO_2 experiments under dry conditions performed by CIEMAT and running up to 900 °C and at isothermal (300 °C) under 1 and 21% O_2 (section 2).
    - UO_2 and SIMFUEL experiments under dry conditions performed by HZDR and running for 1 week at 300 °C under 21% O_2 (section 4).

- UO_2 and Ln-doped UO_2 (Ln ≡ La and La-Nd-Gd) experiments under dry conditions performed by CEMTHI/CNRS and running at different temperatures, from 300 to 1100 °C under Ar-H_2 (10%) (Section 5).

- Wet storage experiments:
  - UO_2 and Eu-doped UO_2 dissolution experiments under wet conditions performed by CIEMAT and running under H_3BO_3 (1600 - 3500 ppm) at room temperature (section 2).
  - UO_2, Ln-doped UO_2 (Ln ≡ Y-La-Pr-Ce-Nd) PGM/UO_2 (PGM ≡ Ru-Rh-Pd) dissolution experiments under wet conditions performed by ICSM/CNRS and running under H_3BO_3 (0 - 2500 ppm) at 50 – 70 °C (section 3).

The findings and outcomes reached from these investigations constitute a comprehensive study of spent nuclear fuel alteration during interim storage that should be accounted by different stakeholders including research organisations, decision-makers, WMOs, regulators and the broader public in Europe. It is demonstrated, that the effect of grain size, the composition, the synthesis route of surrogate samples, the presence of lanthanides and the ^3He release affect the integrity and oxidation of fuel matrix during dry storage conditions. Our findings also indicate relatively low dissolution rates of uranium in those samples where lanthanides are present at all conditions of boric acid concentrations, in air, at different temperatures (25 ˚C, 50 °C and 70 °C). Furthermore, analyses performed on "model materials" based on UO_2 illustrate the importance of research on surrogate specimens, maintaining certain degree of conservatisms, in order to describe the different isolated effects and synergistic phenomena occurring during predisposal activities of SNF assemblies, which may affect the later final disposal stage. However, some questions and uncertainties remain. Firstly, this work does not aim to accurately reproduce all features and experimental behaviour of SNF, but allows to estimate effects of dopant, microstructure and He effects on fuel pellet durability to degradation by oxidant gases or water. To bridge the gap between "model materials" and the complex real SNF systems, inter-comparative analysis should be done to definitively verify the experimental conclusions reached and with associated uncertainties, or data obtained could be validated through the response of predictive models applied for irradiated fuel. Secondly, from our knowledge, we are sure that with these empirical data combined with computational approaches handling both kinetics and thermodynamics, we have progressed towards an understanding of the role of trivalent lanthanides and microstructure within the context of traditional LWR fuels interim storages. At this stage, it is not possible to conclude the agreement between the empirical tests by using model materials, the real SNF and the predictions of chemical codes. The quantitative reproduction of the large experimental data with the conceptual models would help to explain key chemical reaction mechanisms. Overall, it is emphasized the need to be further addressed on reliable behaviour characterisation of SNF at long-term in different environments.

Table of content

Executive Summary 4

Table of content 6

List of figures 8

List of Tables 11

Glossary 12

1. INTRODUCTION AND GOALS 15

1.1. Background of subtask 3.2 15

1.2. Objectives of subtask 3.2 18

1.3. Report structure 21

2. CIEMAT 22

2.1 Samples preparation and solutions 22

2.1.1 Pellets 22

2.1.2 Powders 26

2.1.3 Aqueous phase 27

2.2 Results on the behaviour of UO_2 under dry and wet interim storage conditions 28

2.2.1 Dry oxidation behaviour of Eu doped UO_2-based model material as analogue for spent nuclear fuel 28

2.2.2 Dissolution behaviour of Eu doped UO_2-based model material as analogue for spent nuclear fuel 30

2.3 Discussion and outcomes 33

3. ICSM/CNRS 35

3.1 Samples preparation, solutions and method 35

3.1.1 Preparation of sintered samples of UO_2, $(U,Ln)O_2$, UO_2: PGM and UO_2: PGM+Mo 35

3.1.2 Characterization of powdered and sintered samples of UO_2, $(U,Ln)O_2$, UO_2: PGM and UO_2: PGM+Mo 35

3.1.3 Dissolution tests of sintered samples of UO_2, $(U,Ln)O_2$, UO_2: PGM and UO_2: PGM+Mo 36

3.2 Results on the behaviour of UO_2, $(U,Ln)O_2$, UO_2: PGM and UO_2: PGM+Mo under wet interim storage conditions 38

3.2.1 Synthesis and characterisation of sintered samples 38

3.2.2 Long-term behaviour of sintered samples 40

3.2.3 Saturation experiments: characterization of neoformed phases and speciation calculations 44

3.3 Discussion and outcomes 48

4. HZDR 51

4.1 Synthesis of SIMFUEL 51

4.2 Characterization methods 51
4.2.1 SP-XRD 51
4.2.2 XAS: XANES and EXAFS 51
4.3 Results on the behaviour of SIMFUEL and UO_2 under dry interim storage conditions 51
4.3.1 Characterization of as-synthesized SIMFUEL compounds 51
4.3.2 Oxidation of SIMFUEL 53
4.3.3 Effect of the grain size on the oxidation of UO_2 55
4.4 Discussion and outcomes 57
5. CEMHTI/CNRS 59
5.1 Samples 59
5.2 Characterisation techniques 59
5.2.1 Introduction of helium by ^{3}He implantation 60
5.2.2 Positron Annihilation Spectroscopy (PAS) 60
5.2.3 Nuclear reaction analysis (NRA) 62
5.3 Results on the Helium release in UO_2 under interim storage conditions 62
5.3.1 PAS characterizations of Ln doped uranium oxides 62
5.3.2 Microstructure and chemical composition 68
5.3.3 He release measurements 74
5.4 Discussion and outcomes 77
6. Summary of results 79
6.1 Dry-type experiments 79
6.1.1 CIEMAT 79
6.1.2 HZDR 79
6.1.3 CEMHTI/CNRS 80
6.2 Wet-type experiments 80
6.2.1 CIEMAT 81
6.2.2 ICSM/CNRS 81
7. General conclusions 83
8. Acknowledgements 86
References 87

List of figures

Figure 1 Overview of Nuclear fuel cycle (adapted from [14, 15]. 16

Figure 2 Schematic representation of the microstructure of SNF pellet and the distribution of FP, Pu and MAs after irradiation in a reactor. Figure taken from Ewing [18] and adapted from [16, 17]. 17

Figure 3 SEM images of the prepared samples: a) UO_2, b) 0.02 $^w/_o$ Eu_2O_3 - UO_2, c) 0.2 $^w/_o$ Eu_2O_3 - UO_2, and d) 2 $^w/_o$ Eu_2O_3 - UO_2. 23

Figure 4 XRD patterns (a), zoom on the (111) reflection (b), and lattice parameter evolution (c) of the sintered pellets: UO_2, UO_2-0.02 $^w/_o$ Eu_2O_3, UO_2-0.2 $^w/_o$ Eu_2O_3, UO_2-2 $^w/_o$ Eu_2O_3. Y= (– 1.9756 ± 0.0001) x + (0.5472 ± 0.0001). 25

Figure 5 UO_2-2 $^w/_o$ Eu_2O_3 sintered pellet a) before and b) after being manually milled in an agate mortar prior to thermogravimetric oxidation. 26

Figure 6 Normalised Raman spectra of UO_2, UO_2-0.02 $^w/_o$ Eu_2O_3, UO_2-0.2 $^w/_o$ Eu_2O_3, UO_2-2 $^w/_o$ Eu_2O_3, pre-ground prior to the oxidative treatments. 27

Figure 7 Weight change curves at 21%O_2 (a) and 1%O_2 (c), and reaction rates at 21%O_2 (b) and 1%O_2 (d) of: UO_2, UO_2-0.02 $^w/_o$ Eu_2O_3, UO_2-0.2 $^w/_o$ Eu_2O_3, and UO_2-2 $^w/_o$ Eu_2O_3. 29

Figure 8 Total U concentrations as a function of time: (a, b) in 1600 ppm H_3BO_3 and (c, d) in 3500 ppm H_3BO_3 experiments at a temperature of 20 ± 3 °C, for UO_{2-x} $^w/_o$ Eu_2O_3 (x = 0, 0.02, 0.2, 2). U concentrations are presented in filtered (a, c) and ultrafiltered (b, d) analysed samples. Symbol code: line = blank test, red = pure UO_2 samples, green = UO_2-0.02 $^w/_o$ Eu_2O_3 samples, dark blue = UO_2-0.2 $^w/_o$ Eu_2O_3, light blue = UO_2-2 $^w/o$ Eu_2O_3. Grey lines correspond to the background U concentration in the reference solutions. 31

Figure 9 a) Normalised dissolution rate of U, R_L(U), as a function of time, and b) final values (after 48 days of dissolution experiment) of R_L(U) as a function of Eu content, for Eu-doped and undoped UO_2 dissolved in 1600 ppm and 3500 ppm H_3BO_3. 32

Figure 10 SEM image of a UO_2-2 $^w/_o$ Eu_2O_3 pellet surface after 1 month of dissolution experiment in (a) 1600 ppm and (b) 3500 ppm H_3BO_3. 33

Figure 11 Schematic representation of the dissolution tests protocol performed on sintered pellets. .. 37

Figure 12 X-EDS mapping recorded at the surface of sintered samples of UO_2:PGM (a) and (U,Ln)O_2 (b). 40

Figure 13 Dissolution test of UO_2 (reference material) obtained at 50 °C, at pH =7, in the presence of H_3BO_3 and LiOH. 40

Figure 14 Dissolution test of (U,Ln)O_2 (with 2, 6, 10, 25 mol % Ln) obtained at 50 °C, at pH =7, in the presence of H_3BO_3 and LiOH. 41

Figure 15 Dissolution test of UO_2: PGM obtained at 50 °C, at pH =7, in the presence of H_3BO_3 and LiOH. 41

Figure 16 Dissolution test of UO_2:PGM+Mo obtained at 50 °C, at pH =5, in the presence of H_3BO_3 ... 42

Figure 17 Dissolution test of UO_2:PGM+Mo+Ln obtained at 50 °C, at pH =5.3, in deionized water 43

Figure 18 Operando monitoring of the evolving surface of (U,Ln)O_2 obtained at 50 °C, at pH =7, in the presence of H_3BO_3 and LiOH. 45

Figure 19 Operando monitoring of the evolving surface of UO_2:PGM obtained at 50 °C, at pH =7, in the presence of H_3BO_3 and LiOH. 46

Figure 20 Characterization of the neoformed phase obtained during dissolution tests of UO_2:PGM obtained at 50 °C, at pH =7, in the presence of H_3BO_3 and LiOH (t > 400 days). 47

Figure 21 Characterization of the neoformed phase obtained during dissolution tests of UO_2:PGM obtained at 50 °C, at pH =5, in the presence of H_3BO_3 (t > 550 days). 48

Figure 22 SP-XRD patterns of the as-synthesized SIMFUEL samples (right plot is zoom area of the left plot). 52

Figure 23 U L_3-edge $k^3.\chi(k)$ EXAFS signals of the as-synthesized SIMFUEL samples. 52

Figure 24 U L_3-XANES of the as-synthesized SIMFUEL samples. 53

Figure 25: UL_3-XANES of oxidized SIMFUEL sample. 54

Figure 26: SP-XRD patterns of the oxidized SIMFUEL samples obtained by both solid-state route (ox mixing) and liquid method (ox co-precipitation). 54

Figure 27 SEM SE images of the microstructures of the as-sintered materials. The grain sizes are 3.08 ± 0.06 µm for the micro UO_2 obtained by regular SPS (70 MPa, 10 min, 1600 °C), 478 ± 17 nm for the sub-µ UO_2 produced by 2S-SPS (70 MPa, 3 s at 650 °C, 100 min at 550 °C), and 163 ± 9 nm for the nano-UO_2 prepared by HP-SPS (500 MPa, 30 s, 660 °C). 55

Figure 28 (Up) Evolution of the HT-XRD pattern of the micro-grained UO_2 sample in the first 620 s of the isothermal oxidative treatment. (Down) Evolution of the different phases in the three samples during the oxidative treatments (grouped by sample). 56

Figure 29 Comparison of the SR-XRD patterns for the three samples before and after the oxidation treatment. Contrary to the micro and sub-µ UO_2 samples, no U_3O_8 was detected in the nano-sized compounds after 21 h in air at 300 °C. The main diffraction reflexes of U_3O_8 are marked with a blue star. 57

Figure 30 a) sample arrangement on the implantation sample holder for the first NRA campaign; b) implantation profile of mono-kinetic positrons and of ^{3}He atoms and damage profiles in UO_2 with a density of 10.76 g·cm^{-3} 60

Figure 31 Schematic view of the DIADDHEM set-up used to measure the ^{3}He content in UO_2. 62

Figure 32 a) Low momentum fraction S and High momentum fraction W as a function of probing positron's energy; b) S as a function of W measured in the ten as-received La (6%) doped UO_2 of the set 2 compared to UO_2 reference samples and with the three La (15%) doped UO_2 annealed at 1600 °C/2h/Ar-H_2 (10%) of the set 1 . The half-full symbols correspond to the average of S and W in the 8-12 keV energy range and the full ones to the 18-25 keV range. The green star is the S_{HeSat} W_{HeSat} point and the D1 line is characteristic of annihilations at Vu related complexes. 63

Figure 33 S as a function of W measured in the Ln doped UO_2 of the 3 sets in as-received state for the set 2 (La (6 mol %)) and Set 3 (La, Nd and Gd, 6-25 mol %) and after annealing at 1600 °C/2h/Ar-H_2 (10%) for the set 1 compared to UO_2 reference samples. The symbols correspond to the average of S and W in the 18-25 keV energy range. The green star is the S_{HeSat} W_{HeSat} point and the D1 line is characteristic of annihilations at Vu related complexes. 64

Figure 34 S as a function of W measured in the La 6 and 15 mol % doped UO_2 of the Set 1 and 2 after annealing at 1500 °C/5h/Ar-H_2 (10%) with unintentional H_2O leakage compared to UO_2 reference samples. The symbols correspond to the average of S and W in the 18-25 keV energy range. The green star is the S_{HeSat} W_{HeSat} point and the D1 line is characteristic of annihilations at Vu related complexes. The pink triangle correspond to the SW values recorded for an intentionally over-oxidized $UO_{2.21}$ sample [99]. 64

Figure 35 a) Low momentum fraction S as a function of probing positron's energy; b) S as a function of W measured in the La (6% and 15 mol %) doped UO_2 of the set 1 and 2 after the second annealing at 1500 °C/5h/Ar-H_2 (10%) compared to UO_2 reference samples. The symbols correspond to the average

of S and W in the 18-25 keV energy range. The green star is the S_{HeSat} W_{HeSat} point and the D1 line is characteristic of annihilations at Vu related complexes. 65

Figure 36 S as a function of W measured in the La 6 and 15 mol % doped UO_2 of the Set 1 and 2 a) after implantation with 1MeV ^{3}He at $1{\cdot}10^{16}$ cm^{-2} (full circle) compared with the as-received state (crossed open circle) and the as-annealed state (after the second annealing at 1500 °C/5h/Ar-H_2 (10%), half-full circles) and to UO_2 reference samples; b) after implantation and annealing at 400°C/1h/Ar-H_2 (10%). The symbols correspond to the average of S and W in the 18-25 keV energy range. The green star is the S_{HeSat} W_{HeSat} point and the D1 line is characteristic of annihilations at Vu related complexes..... 67

Figure 37 Some examples of the general aspects of the Ln doped UO_2. 68

Figure 38 Grain size distribution and mean size in the La doped UO_2 of the set1 and 2. 68

Figure 39 Raman spectra in the La doped samples from a) set 1 in as-received state and b) from set 2 after annealing at 1600 °C/2h/Ar-H_2 (10%). 69

Figure 40 Raman spectra in the La doped UO_2 samples from sets 1 and 2 after annealing at 1500 °C/5h/Ar-H_2 (10%) a) first annealing with unintentional oxidation, b) second annealing in reducing conditions..... 71

Figure 41 Raman spectra measured in La doped UO_2 from sets 1 and 2 after annealing at 1500 °C/5h/Ar-H_2 (10%) and implantation with 1 MeV ^{3}He ions at RT and a fluency of $1{\cdot}10^{16}$ cm^{-2} 72

Figure 42 T_{2g} position (a), width (b) and intensity (c) in La doped UO_2 as a function of the La concentration in a.p.f.u (atomic proportion per formula *unit).* 73

Figure 43 ^{3}He amount remaining in the (a) La doped UO_2 from the set 1 and 2 after annealing in Ar-H_2 (10%) atmosphere at increasing temperature during 1 to 6 hours and compared to UO_2 samples and (b) Ln doped UO_2 from the sets 1, 2 and 3 after annealing in Ar-H_2 (10%) atmosphere at increasing temperature during 1 hour. 75

List of Tables

Table I Summary of the experimental approaches by the different organisations for studying nuclear fuel behaviour on simulated interim storage. 20

Table II Specifications of the as-sintered Eu-doped and undoped UO_2 pellets used for the dissolution experiments. 23

Table III Aqueous media composition. 28

Table IV Data for the oxidation of each studied material at 21% O_2 and at 1% O_2. 29

Table V Conditions of thermal conversion of the starting hydroxide precursors. SSA and unit cell parameters of the powders obtained after conversion at 700 °C. 38

Table VI Sintering conditions as well as density and SSA of the final sintered pellets. 39

Table VII Results of dissolution tests performed at T = 50 °C. All the normalized dissolution rates are expressed in $g \cdot m^{-2} \cdot d^{-1}$. t_{TOT} corresponds to the global duration of the leaching time, t_1 corresponds to the time at which a break in slope is observed (when observed). Normalized dissolution rate obtained before and after t_1 are indicated in bold or italic, respectively. 43

Table VIII Conditions associated to the potential saturation of the solution based on macroscopic analysis in solution and associated U concentrations at equilibrium. 44

Table IX Sets of Ln doped UO_2: the synthesis of powder, sintering conditions and heat treatment of the disks (*nominal concentration specified by the manufacturer). 59

Table X List of samples chosen for the first He release experiment campaign. (*) the concentration of dopant measured in samples from the same group using SEM/EDX is given in brackets (see section 5.3.2.2). 66

Table XI SEM/EDX analysis in Ln doped UO_2. 74

Table XII List of samples chosen for the second He release experiment campaign. (*) nominal concentration of dopant as expected from the sample preparation 76

Glossary

AFM	Atomic Force Microscopy
apfu	Atomic proportion per formula unit
BSD or BSE	Backscattered Electron Detector or Back Scattered Electrons
BET	Brunauer–Emmett–Teller theory
CEMTHI/CNRS	Conditions Extrêmes et Matériaux : Haute Température et Irradiation / Centre national de la recherche scientifique
CIEMAT	Centro de Investigaciones Energéticas, Medioambientales y Tecnológicas (english: The Center for Energy, Environmental and Technological Research), Spanish public research institution in energy and the environment
AFM	Atomic Force Microscopy
dpa	displacement per atom
EDX /EDS	Energy Dispersive X-ray Spectroscopy
ESEM	Environmental Scanning Electron Microscope
EXAFS	Extended X-ray Absorption Fine Structure
FP	Fission Product
FWHM	Full Width at Half Maximum
HLW	High Level Waste
IAEA	International Atomic Energy Agency
ICP-AES	Inductively coupled plasma atomic emission spectroscopy
ICP-MS	Inductively Coupled Plasma – Mass Spectrometry
ICP-OES	Inductively coupled plasma optical emission spectroscopy
ICSM/CNRS	Institut de chimie séparative de Marcoule / Centre national de la recherche scientifique
HBS	High Burnup Structure
HERFD	High Energy Resolution Fluorescence Detected
HZDR	Helmholtz-Zentrum Dresden-Rossendorf
HT-SRXRD	High-Temperature Synchrotron Radiation X-Ray Diffraction
Ln	Lanthanide

MA	Minor Actinides
MOX	Mixed Oxide Fuel
NPP	Nuclear Power Plant
PAS	Positron Annihilation Spectroscopy
PALS	Positron Annihilation Lifetime Spectroscopy
ppb	Parts per billion
ppm	Parts per million
PGM	Platinum Group Metals
PXRD	Powder X-ray Diffraction
TMS	Root Mean Square
RT	Room Temperature
RWM	Radioactive Waste Management
SD	Standard Deviation
SEM/EDX	Scanning electron microscopy / Energy dispersive X-ray spectroscopy
SE	Secondary Electron detector
SESAM	Study of Evolving Surface Area by Microscopy
SFC	Spent Fuel Characterization
SIMFUEL	Simulated nuclear fuel consisting of UO_2 doped with inactive lanthanides and other fission products, including metallic particles, in proportions corresponding to the simulated burnup
SNF	Spent Nuclear Fuel
SPB-DB	Slow Positron Beam coupled to a Doppler Broadening spectrometer
SP-XRD	Synchrotron powder X-ray diffraction
SRIM	The Stopping and Range of Ions in Matter
SSA	Specific Surface Area
TD	Theoretical Density
TGA	Thermal Gravimetric Analysis
TRU	Transuranic elements (actinide elements with atomic numbers greater than U, 92)

UO_2	Uranium dioxide
WMOs	Waste Management Organisations
w/o	Weight percentage
WP	Work Package
XANES	X-ray Absorption Near Edge Structure
XAS	X-ray Absorption Spectroscopy
XES	X-ray Emission Spectroscopies
XPS	X-ray Photoelectron Spectroscopy
XRD	X-Ray Diffraction

1. INTRODUCTION AND GOALS

The broader scope of the work package 8 "Spent Fuel Characterization" (SFC) is to reduce uncertainties of Spent Nuclear Fuel (SNF) properties in predisposal phase and particularly, to understand the behaviour of fuel and ageing effect under normal and postulated accident scenarios until disposal, in order to identify relevant or typical bounding cases at time of conditioning and predisposal activities. According to the IAEA, predisposal management of radioactive waste involves all the phases in the management of radioactive waste from its production after being irradiated in Nuclear Power Plants up to disposal, "including processing (pre-treatment, treatment and conditioning), storage and transport" [2, 3]. All these predisposal steps (timescale of a few decades or even few centuries) are directly linked with final disposal (typically of the order of thousands up to a million years) [4].

Within the SFC work programme, **task 3 "Behaviour of nuclear fuel and cladding after discharge"** aims to understand and describe the behaviour of SNF under conditions of extended interim storage, transportation and storage in a final disposal system. This objective is achieved by involving experimental works and modelling studies, and is organised under three subtasks:

- The thermo-mechanical-chemical properties of SNF rods and cladding (Subtask 3.1).
- The behaviour and ageing of SNF pellets under interim storage conditions (Subtask 3.2).
- Fuel-cladding chemical interaction (FCCI) (Subtask 3.3).

1.1. Background of subtask 3.2

The SNF behaviour has been studied in many previous projects funded by Euratom (SFS (2001-2004), NF-PRO (2004-2007), MICADO (2006-2009), REDUPP (2011-2014) and FIRST-Nuclides (2012 - 2014) and DISCO (2017-2021)) [5-10]; however, all of them were focused in the quantitative understanding of key processes affecting the SNF in geological repository conditions. The main objective of subtask 3.2 is to improve the description of the most relevant processes driving the chemical evolution of SNF at the interim storage conditions (*e.g.* wet and dry) based on new experimental data that may have an impact on final disposal. The study of the different intrinsic (specific to SNF attributes) and extrinsic (environmental storage conditions) parameters that can affect SNF matrix integrity evolution is of extreme interest for irradiated fuel under operational and accidental scenarios during the early stages of back-end of the nuclear fuel cycle (Figure 1) such as handling, transporting and storing. To ensure SNF integrity under whatever considered scenarios (*e.g.* moisture, aqueous dissolution of the UO_2 matrix, corrosion of the SNF, etc.), systematic identification of events and their consequential effects, that are still not well understood, should be considered in the safety assessment [11-13].

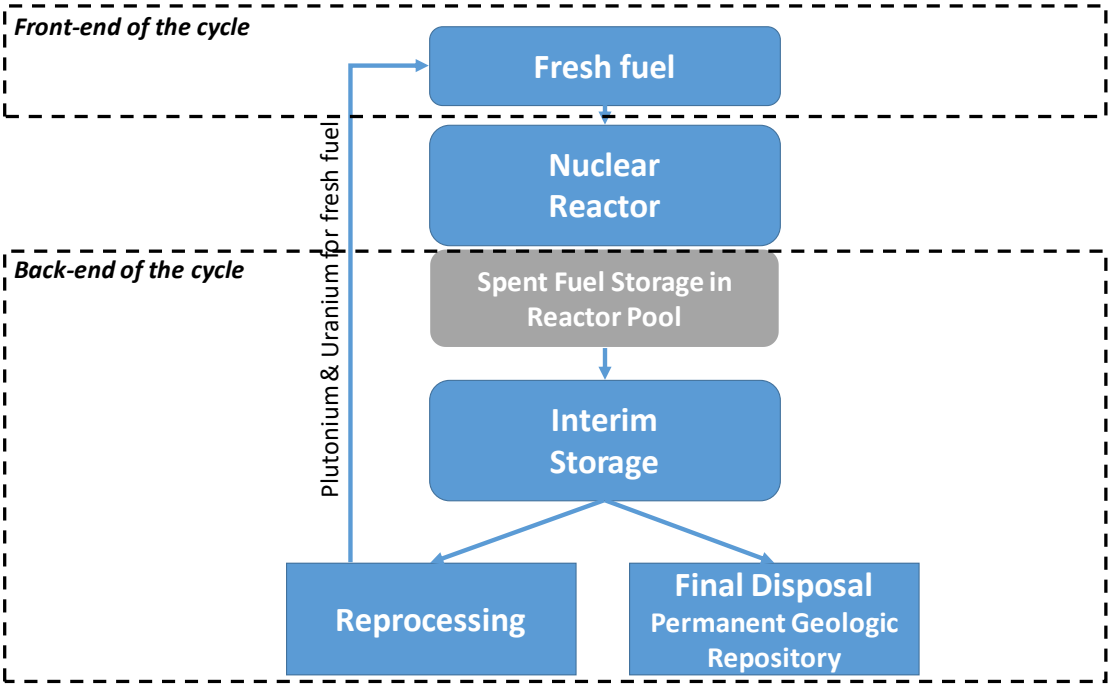

Figure 1 Overview of Nuclear fuel cycle (adapted from [14, 15].

The experimental work with SNF is a challenging matter, inherently difficult and expensive because of its radiological constraints and requirements, added to its physico-chemical complexity that can steadily change with time (Figure 2) [16-20]. In fact, the SNF is one of the most complex materials in terms of chemical composition in different phases and states. After the operation of nuclear fuel in LWR reactor, it results in cracked fuel pellets; production of fission gases (Cs, Rb, Te, I), solid fission products, transuranic elements (*e.g.* Pu, Cm and Am), and activation products; thermal expansion and cladding creep resulting in gap closure; and radioactivity [18, 19, 21-24]. Before direct disposal of SNF in a deep underground repository, and after being discharged from the reactor, the SNF is stored in cooling pools at the reactor site to allow for the decay of the heat capacity (related to very short-lived nuclides decay) below a specific level. Then, the used fuel may be transferred (transport) to wet or dry long-term interim storage for periods from 30 years up to 100 years, because of the lack of geologic repositories [11, 18, 21, 23, 24]. The SNF is theoretically able to resist long-term interim storage without important changes of its features; however, some elementary processes need to be further addressed.

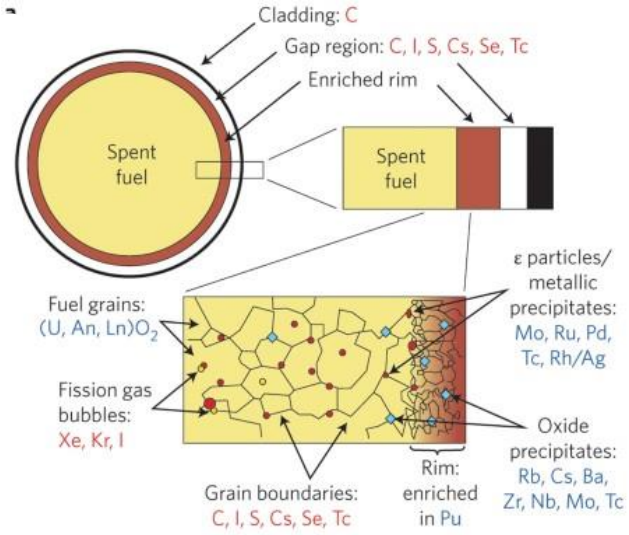

Figure 2 Schematic representation of the microstructure of SNF pellet and the distribution of FP, Pu and MAs after irradiation in a reactor. Figure taken from Ewing [18] and adapted from [16, 17].

A deep understanding of complex phenomena occurring in this material is a requirement for building predictive models including all back-end stages at short, medium and long-time scales in safety assessments of SNF. The above-mentioned constraints and the fact that U is essentially the main element present in SNF matrix (in the form of UO_2) are consequently motivation for research of surrogate systems (using non-irradiated nuclear fuel and model U-based materials) that can show some of the important behaviours of the irradiated fuel. Knowing that working with SNF is more representative of the realistic scenario, the results are complicated to interpret and make a full understanding of the systems difficult. In order to gain knowledge on separate and synergic effects and also to develop/conduct fundamental research, the use of non-irradiated alternatives is important before carrying out experimentation on real irradiated systems presenting radiological risks that must be handled with particular care (in hot-cells which capability is limited to some countries). The experimental research proposed in this report has been performed by means of various "model materials" that can represent some physico-chemical properties maintaining certain degree of conservatisms. However, from the chemical point of view, knowing the real nuclide inventory of activation products and long-lived FP as a function of burnup and time is essential to study the impact of long-term alteration of SNF on the biosphere [25, 26]. Note that within SFC Task 2, one of the main objectives is to produce experimentally verified and validated procedures for estimating not only the radionuclide inventory of SNF but also its decay heat composition [25, 26]. As it has been previously described, physicochemical changes in fuel pellet properties are influenced by various factors, which will be examined in this subtask.

Oxidising gas intrusion such as air into a breached cladding SNF rod may cause a SNF **matrix oxidation** up to U_3O_8, associated with a ~36% volumetric expansion with respect to the initial UO_2 [27, 28], and turn out with spallation and pulverization of material [13, 27]. This may pose a safety issue for SNF management as it could imply a confinement failure and hence dispersion of radionuclides into the environment [29]. Moreover, the solubility of U(VI) is significantly higher (~2-3 orders of magnitude)

than that of U(IV), resulting in faster migration in aqueous media [30]. It is generally assumed that the fluorite-type lattice of UO_2 matrix is stabilized at intermediate oxidation states (U_4O_9/U_3O_7) during oxidation with the presence of dopants [31-36]. Some efforts are needed to improve the knowledge about the effect of these dopants or impurities in the fuel oxidation resistance to U_3O_8, and in particular of trivalent lanthanides formed due to the nuclear fission reactions and SIMFUEL [12]. Additionally, during reactor operation, the high-burnup structure (HBS) starts to form at the peripheral rim of the fuel pellets, characterised by the restructuring of the initial 10−15 µm grains into 100−300 nm ones [23]. With regard to physico-chemical evolution of the spent fuel in a closed system (as referred by Ferry et al. [37, 38] "without external exchange of matter") specifically due to the high α-decay, this process is associated with helium production and accumulated damage of the ordered UO_2 structure. **Helium build-up** and diffusion induces fuel swelling and changes of the fuel pellet properties over time (*e.g.* micro-cracks). The long-term consequences of He in the SNF microstructure is one of the main uncertainties concerning the evolution of SNF in a closed system that need further assessment [37, 38]. It is known to strongly interact with vacancy defects in UO_2, thus the impact of the lanthanides on the defects distribution should be investigated.

In wet storage facility, pools of water containing boron for criticality control are used for SNF storage in at-reactor operational pools that offer both radiation shielding and a thermal sink. Also for some European countries, it is the option for interim storage during one-hundred-year operational lifetime, and may or may not be built at reactor site. Special attention should be taken on fuel degradation and the consequent potential radioactivity leakage in this period. Assuming cladding failure, water can reach the fuel during pool storage. The fuel matrix dissolution will depend on its own attributes, including chemical composition. For this reason, it is important to have a good understanding of the role of trivalent fission products (produced during irradiation) on the UO_2 **matrix corrosion** and fuel chemical durability. The assumption of undetected damage of cladding during the fuel handling and loading in the pools, although it is expected to be minimal, should be considered in the safety analysis of a spent fuel storage pool. Under normal circumstances, the borated water temperature of the pool is kept below 50 – 70 °C to prevent boiling of the cooling water at longer storage times.

Thus, quantitative data about environmental impact of spent fuel storage in dry storage installations or storage pool facilities are needed for the stage following the period of the reactor operating license, not only during normal operations, but in the event of potential accidents or when the SNF will be eventually unloaded [14].

1.2. Objectives of subtask 3.2

This deliverable produced under SFC Task 3 summarises the results and outcomes of Subtasks 3.2. The efforts to improve the fuel characterisation in storage systems are focused on reducing uncertainties about the alteration, corrosion and dissolution behaviour of SNF by means of advanced techniques, materials and methods. The chemical and structural complexity of SNF and the associated radiation fields complicate answering still open questions from experiments with SNF. Thus, corrosion studies within this subtask was studied using systematically prepared and precisely characterised UO_2-based model materials to understand several single and linked effects on SNF behaviour under relevant

conditions of interim storage. A detailed characterisation and behaviour of SNF is a particularly important issue in order to ensure that these storage systems provide adequate confinement and maintain fuel integrity when stored. The experimental programme is intended (1) to examine the integrity and performance of the nuclear fuel pellet and (2) to provide new experimental data on fuel behaviour during storage and handling until disposal. Individual and linked effects were studied to simulate complex scenarios. The ultimate goal is to enhance the knowledge on the fundamental processes and mechanisms for predictive model calculations on the dependence of the corrosion of UO_2(s) with the presence of FP, TRU and some other elements in different phases. More specifically, subtask 3.2 seeks to:

1. Contributing on the operational safety of interim storage facilities by providing new insights and reliable data on the ageing and degradation mechanisms of the SNF (*e.g.* in-pile nominal conditions, accidental scenarios and long-term behaviour of the stored fuel), during dry storage and wet pool storage. This was achieved by examining various effects:
    - The role of fission products, mainly trivalent lanthanides (Eu, La, Nd, Gd), covering a range of concentrations, on microstructure and behaviour properties of UO_2.
    - Matrix corrosion under several environment conditions representative of interim storage.
    - The He build-up influence on the formation of vacancy defects in SNF.
2. Applying advanced methodologies and techniques to characterize SNF (*e.g.* cutting-edge synchrotron methods [39], spectroscopic methods, etc.) to understand the degrading mechanisms at the multiscale level, including atomic.
3. Developing new synthesis methods and detailed characterization of model materials to support SNF corrosion studies.

Different organisations are involved in this subtask: CIEMAT, CNRS/ICSM, HZDR and CNRS/CEMHTI. Table I shows the systems that have been studied by the different organisations. More details on the studies carried out by the different partners, and the respective experimental protocols are given in the following sections.

Table I Summary of the experimental approaches by the different organisations for studying nuclear fuel behaviour on simulated interim storage.

Organisation	Materials used	Measurement / Type of experiment	Techniques	Outcomes
CIEMAT	UO_2 Eu-doped UO_2: 0.02; 0.2; 2 $^w/_o$ Eu_2O_3-UO_2 **Synthesis and sintering** • Pellet, dry route, Sintering: 1675 °C, 4h, N_2/H_2 (4.7%) • Powder	**Dry: oxidation behaviour** T: RT to 900 °C $O_2(N_2)$ conc.: 0.1-21% **Wet: Aqueous dissolution test** H_3BO_3: 1600 and 3500 ppm pH: ~ 5.2 RT	• Solid: TGA, SEM-EDX, BET, XRD, Raman • Analysis in solution: pH, redox, ICP-MS	Effect of Ln dopants on the oxidation kinetics of UO_2 matrix as a function of potential O_2 intrusion in Dry Conditions. Chemical durability of the matrix dissolution on UO_2 -Eu_2O_3 under relevant pool storage conditions.
CNRS-ICSM	UO_2 $(U,Ln)O_2$: • Ln: 2, 6, 10 and 25 mol % • Ln: Y (7%), La (13%), Ce (26%), Pr (12%) and Nd (42%) UO_2 + 3 mol % PGM • UO_2 + 3 mol % PGM + 2 mol % Mo • UO_2 + 3 mol % PGM% + 2 mol % Mo + 3 mol % Ln **Synthesis and sintering** Hydroxide precipitation. Conversion at 700 °C, 4 h, Ar-H_2 4% Sintering: • $(U,Ln)O_2$: 1600 °C, 4h, Ar/H_2 • UO_2+PGM: 1500 °C, 4h, Ar/H_2	**Wet: Dissolution tests** H_3BO_3: 2500 and 0 ppm pH: 5 or 7 T: 50 °C or 70 °C	• Solid: SEM, EDX, BET, XRD, Raman, Geometrical density, He-pycnometry • Analysis in solution: pH, Eh, ICP-OES, ICP-MS • Speciation: Phreeqc modeling • Solid/solution interface: ESEM, Raman, XRD	Solid/liquid interface in contact with the solution ➔ reactive surface area during dissolution and the dissolved preferential zones (grain boundaries, triple junctions, pores, …) for dissolution/altered materials
HZDR	UO_2 pellet (by JRC, dry route) SIMFUEL pellet (different compositions & storage time ➔ burnup) **Synthesis** - solid-state route - liquid method: oxalate precipitation - Spark Plasma Sintering HBS (UO_2)	**Dry: oxidized in furnace** T < 350 °C O_2: Air Time: several days (depending on the grain size and the FP content)	SEM, TEM. EPMA, XRD. Synchrotron methods (XANES, EXAFS, XES, XRD) Scattering techniques (XRD, RAXR, CTR), HERFD-EXAFS, Synchrotron	Effect of chemical composition, microstructure and irradiation damages on the evolution of spent fuel separately (not possible by using spent fuel)
CNRS-CEMHTI	Ln-UO_2 (by CNRS ICSM, wet route) • 1, 5 and 20 mol % La • 6 - 20 mol % Nd • 6 – 20 mol % Gd	**Dry: isochronal heating** T: 100 - 600 °C O_2: non defined Time: 1 – several tens of hours	PAS PALS SPB-DB Raman spectroscopy	He behaviour (induced defects) in simulated spent fuel as a function Ln content in doped UO_2, annealing temperature and duration

1.3. Report structure

The first part of this document describes the studies proposed by different organisations participating in WP8 SFC Task 3, subtask 3.2 on corrosion studies to understand several effects affecting SNF behaviour under conditions relevant of interim storage. This report has the following structure:

- Section 2 summarises the materials, methodology and results from CIEMAT.
- Section 3 summarises the materials, methodology and results from CNRS/ICSM.
- Section 4 summarises the materials, methodology and results from HZDR.
- Section 5 summarises the materials, methodology and results from CNRS/CEMHTI.
- Section 6 provides an overview of Subtask 3.2 including the resulting summary.
- Section 7 captures Subtask 3.2 conclusions.

2. CIEMAT

2.1 Samples preparation and solutions

At CIEMAT, a series of Eu-doped and undoped UO_2 pellets (UO_2, UO_2-0.02 $^w/_o$ Eu_2O_3, UO_2-0.2 $^w/_o$ Eu_2O_3 and UO_2-2 $^w/_o$ Eu_2O_3) were manufactured by pressing the powder mixtures of precursor oxide powders in weighted amounts. Europium oxide of 99.99 % purity supplied by Aldrich and natural UO_2 obtained via Ammonium Di-Uranate (ADU) precipitation and oxidation/reduction [28] were the powders used for preparing the samples. The procedure through which the target pellets were fabricated consisted of mechanical dry blending of the ceramic powders (together with the binder EBS (N,N'-Ethylenebisoctadecanamide), followed by a cold compaction at 700 MPa (uniaxial press) to obtain green pellets. The latter were then calcined at three temperature steps (100, 300 and 500 °C) and sintered at 1675 °C for 4 h. Both treatments were conducted under a reducing atmosphere in an alumina tubular furnace. Thermal annealing was subsequently carried out to reveal the grains, once the sintered pellets were polished. This fabrication procedure is described in more detail in our earlier articles [40-42].

Once sintered, a detailed characterisation of the pellets was carried out. Thereafter, most of the as-prepared pellets were directly used for dissolution tests. However, one pellet representative of each composition of Eu-doped (and undoped) UO_2 was manually milled in an agate mortar prior to being subjected to dry oxidation experiments. These powdered samples were likewise characterised.

All these solids characterisation outcomes, as well as the description of the aqueous phase used for the pellet dissolution experiments, are hereunder described.

2.1.1 Pellets

An overview of the determined specifications and characteristics of the as-sintered Eu-doped and undoped UO_2 pellets are given in Table II.

The specific surface area (SSA) was geometrically calculated (without roughness factor) and measured by N_2 BET method (ASAP 2020, Micromeritics) [43]. This is a key parameter to understand the alteration processes. There is a consensus that SSA values based on geometrical consideration underestimate the real surface area caused by surface roughness and porosity. On the contrary, values based on the BET method overestimate the effective surface area for materials in which the porosity does not allow water to enter (*i.e.*, typically small mesopores), as the N_2 used in this sorption isotherm method can penetrate deeper than the leaching solution inside the solid phase [38, 44]. Because there is no reliable method to quantify the surface area, both BET and geometric approaches are included in Table II. In these samples, all the SSA values are in the same order of magnitude for each method.

The surface morphology of the pellets was examined by scanning electron microscopy (SEM) (TM4000 Plus, HITACHI), revealing a homogeneous grain structure and isolated porosity, as can be observed in the images of Figure 3. From these images, the average grain size of the different samples was estimated via the linear intercept method [45]. The grain size of the pellets doped with 0.02 $^w/_o$ Eu_2O_3

remains unchanged for undoped UO_2; however, this value increases a little for the 0.2 $^w/_o$ Eu_2O_3 doped sample and then slightly decreases for the highest dopant amount, *i.e.* 2 $^w/_o$ Eu_2O_3 (see Table II and Figure 3) [46].

Table II Specifications of the as-sintered Eu-doped and undoped UO_2 pellets used for the dissolution experiments.

SAMPLE	UO_2	0.02 $^w/_o$ Eu_2O_3-UO_2	0.2 $^w/_o$ Eu_2O_3-UO_2	2 $^w/_o$ Eu_2O_3-UO_2
SSA BET ($m^2 \cdot g^{-1}$)	0.43 ± 0.01	0.55 ± 0.02	0.26 ± 0.01	0.21 ± 0.01
SSA GEOM ($m^2 \cdot g^{-1}$)	0.00022 ± 0.00001	0.00021 ± 0.00001	0.00020 ± 0.00001	0.00020 ± 0.00001
Grain size (µm)	6.9 ± 0.8	6.7 ± 0.5	11 ± 1	5 ± 1
Density immersion ($g \cdot cm^{-3}$)	9.8 ± 0.1	9.6 ± 0.1	9.3 ± 0.2	9.3 ± 0.8
Density geom. ($g \cdot cm^{-3}$)	9.6 ± 0.3	10.0 ± 0.7	9.7 ± 0.1	9.8 ± 0.3
Lattice param. (nm)	Fm-3m a=b=c=0.54724(2)	Fm-3m a=b=c=0.54723(2)	Fm-3m a=b=c=0.54719(4)	Fm-3m a=b=c=0.54684(3)

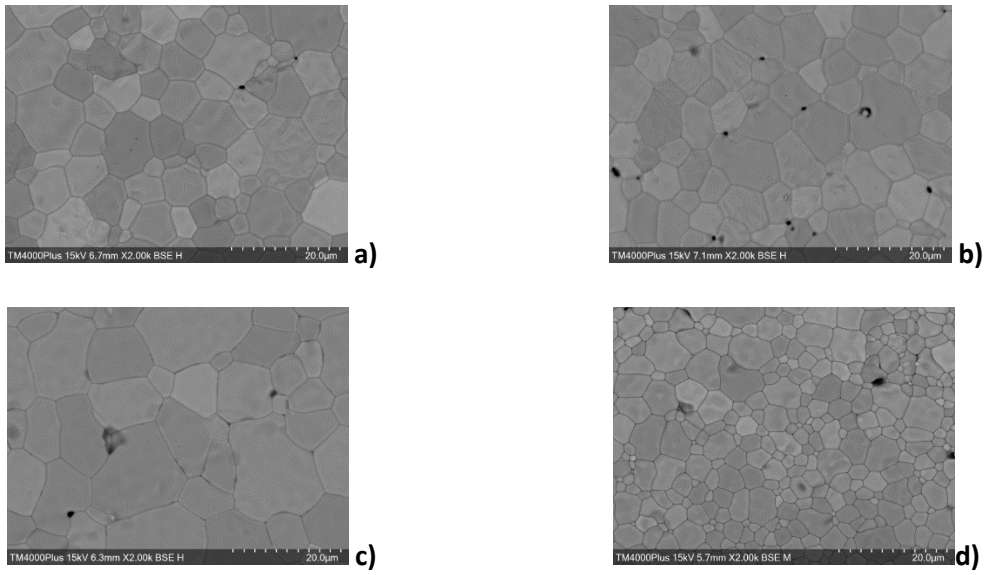

Figure 3 SEM images of the prepared samples: a) UO_2, b) 0.02 $^w/_o$ Eu_2O_3 - UO_2, c) 0.2 $^w/_o$ Eu_2O_3 - UO_2, and d) 2 $^w/_o$ Eu_2O_3 - UO_2.

The density of the pellets was estimated using two different methods: 1) geometric density based on the pellet dimensions, which includes both open and closed porosity and assumes perfect cylindrical pellets; 2) immersion density measurement by Archimedes method (Sartorius kit), which allows more precise measurements. Both, grain size and density errors were calculated using mean SD (± 1σ). The density values obtained by both methods, of about 9.5-10 $g \cdot cm^{-3}$ for the different samples, are in good agreement. The theoretical density values for UO_2 and Eu_2O_3 are 10.97 and 7.4 $g \cdot cm^{-3}$, respectively. Thus, given that the density of Eu_2O_3 dopant is lower than UO_2 density, a decrease in density as a function of Eu content can be expected.

Moreover, X-ray diffraction (XRD) was used to analyse the crystalline structure of the samples. The equipment employed was a Bruker D8 Advance Eco diffractometer using Cu Kα radiation (λ = 1.54056 Å) at 40 kV and 25 mA, with a Bragg-Brentano configuration. The XRD patterns were recorded in the range 20˚<2θ<120˚. Calibration was carried out by using an alumina standard. The lattice parameter of each sample was calculated by a Rietveld refinement process using the DIFFRAC.TOPAS program (Bruker Analytical X-Ray Systems), considering the Fm-3m #225 space group. The XRD patterns of the Eu-doped and undoped UO_2 pellets are shown in Figure 4.

The patterns of UO_2 fuel containing 0.02 $^w/_o$, 0.2 $^w/_o$ and 2 $^w/_o$ Eu_2O_3 also correspond to a fluorite-type structure (Figure 4a), meaning that they conform a $(U,Eu)O_2$ solid solution, which is in agreement with the literature [47-49]. No segregated Eu_2O_3 is observed in any of the samples, implying that the dopant is well dissolved into UO_2 grains. Comparison of XRD patterns of the undoped material with Eu-doped samples indicates that the presence of increasing content of the Eu additive does not affect the crystalline structure significantly. The only observable change is a continuous slight decrease in the lattice parameter (see the steady shift in (111) reflection in Figure 4b with increasing Eu content. The lattice parameter (a), calculated by the Rietveld refinement, is plotted as a function of Eu content in Figure 4c. It shows a linear decrease (Vegard's law) with increasing Eu content, where the Eu_2O_3 content was ≤ 2 $^w/_o$, similar to what has been previously observed in this kind of samples [49] and when UO_2 is doped with other trivalent elements [50, 51]. Based on the measured results, a regression analysis was performed on the measured lattice parameters of Eu -doped UO_2 solid solution. It can be expressed as:

$$a = (-1.9756 \pm 0.0001) \cdot x + (0.5472 \pm 0.0001) \quad (1)$$

where *a* is the lattice parameter in nm, and *x* is the Eu_2O_3 content by weight ($^w/_o$) in Eu_2O_3-doped UO_2. The coefficients of eq. *(1)* are determined by using a least-squares method with the relative coefficient is 0.99921.

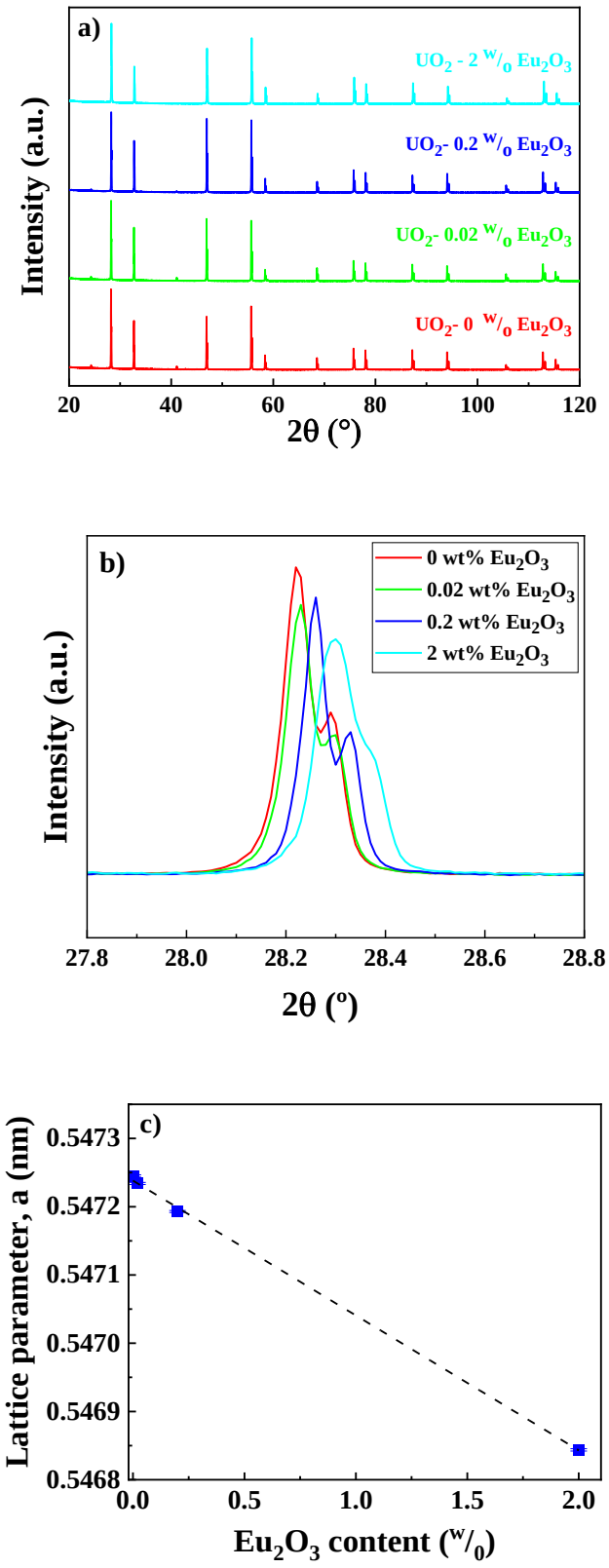

Figure 4 XRD patterns (a), zoom on the (111) reflection (b), and lattice parameter evolution (c) of the sintered pellets: UO_2, UO_2-0.02 $^w/_o$ Eu_2O_3, UO_2-0.2 $^w/_o$ Eu_2O_3, UO_2-2 $^w/_o$ Eu_2O_3. Y= (– 1.9756 ± 0.0001) x + (0.5472 ± 0.0001).

2.1.2 Powders

As already mentioned, samples were prepared, before the dry oxidation experiments in the thermogravimetric equipment, by manually milling in an agate mortar a replica of the sintered pellets for each Eu composition (UO_2, UO_2-0.02 $^w/_o$ Eu_2O_3, UO_2-0.2 $^w/_o$ Eu_2O_3 and UO_2-2 $^w/_o$ Eu_2O_3) (see an example in Figure 5).

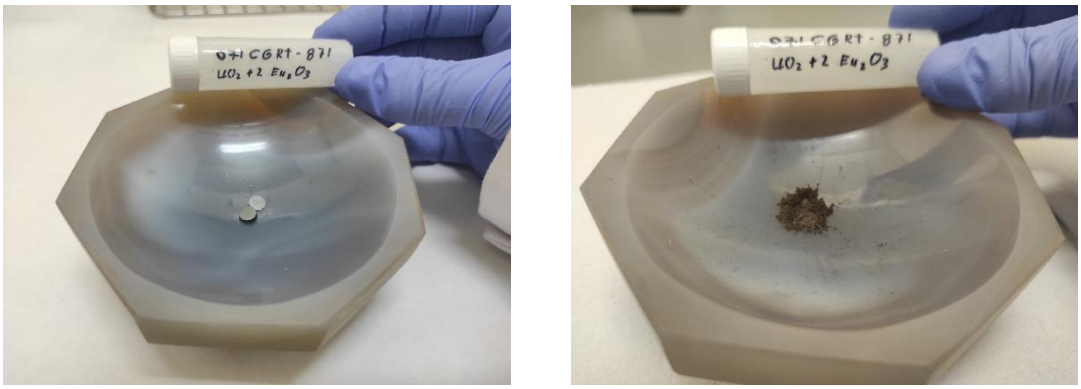

a) **b)**

Figure 5 UO_2-2 $^w/_o$ Eu_2O_3 sintered pellet a) before and b) after being manually milled in an agate mortar prior to thermogravimetric oxidation.

The obtained powders were once again characterised by XRD (results not shown), to check both the bulk homogeneity of the pellets and the lack of alteration due to the milling process. Also in this case, only peaks derived from a single fluorite-type phase (Fm-3m) were identified, which proves the $(U,Eu)O_2$ solid solution formation.

In addition, Raman spectroscopy characterisation was performed on these powders. The equipment used was a LabRAM HR Evolution spectrometer (Horiba Jobin Yvon Technology) with a He-Ne laser excitation source (λ=632.8 nm) and an adapted Olympus BX41 microscope. Raman spectra were acquired at room temperature with the 50x objective, at a power of 1 mW (5% nominal power filter) and an acquisition time of 50 s and in the 50–2200 cm^{-1} range. Spectra were calibrated by using the emission lines of a Ne arc-lamp. Typically, 10 spectra were acquired and summed for each sample. It has been recognised that Raman spectroscopy is capable of distinguishing defects of the O sublattice in UO_2 [41, 51, 52], thus, a Raman analysis could allow us to identify oxygen vacancies (due to Eu^{3+} incorporation) present in each of the prepared Eu-doped samples.

The acquired Raman spectra on the Eu-doped and undoped UO_2 samples are shown in Figure 6. Raman spectrum of undoped UO_2 sample pellet shows the typical fingerprint of a fluorite structure: the T_{2g} band at ~445 cm^{-1}, assigned to U-O symmetric stretching mode in the fluorite structure [41] and a broad peak at ~1150 cm^{-1}, the 2LO band, ascribed to the first overtone of the longitudinal optical phonon mode [53]. The broad feature at 500 - 650 cm^{-1}, mainly formed by the peak centered at ~530 cm^{-1} is interpreted as a “defects band” due to oxygen-vacancy-induced lattice distortion associated with the presence of trivalent cations. The intensity of this peak remains low at 0 and 0.02 $^w/_o$ Eu_2O_3, but it noticeably increases with increasing Eu loading, as shown in similar cases like Gd-, Nd- and La-doped UO_2 [51, 52, 54] for similar doping level. The other band featured in that region, at ~575 cm^{-1}, has been attributed to the first-order longitudinal optical (LO) phonon mode [41, 54-56] and it is

related to structure distortions. This band behaves equivalently to that at ~530 cm^{-1}. This behaviour can be interpreted as due to the Eu_2O_3 incorporation into the cubic lattice of UO_2, which is also in good agreement with XRD results. The intensity of the 2LO band is retained at 0-0.2 $^w/_o$ Eu_2O_3, but significantly decreases at 2 $^w/_o$, as a result of the distortion of the fluorite lattice structure induced by doping. These observations are consistent with those of Talip *et al*. [52] and Lee *et al*. [51], who observed similar results analysing La- and Gd-doped UO_2 samples, *i.e.* an intensity decrease of the 2LO band when increasing the La or Gd content, respectively.

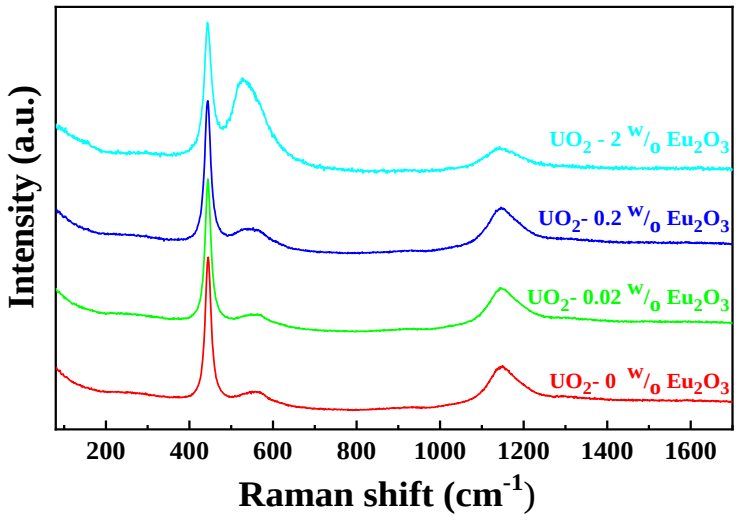

Figure 6 Normalised Raman spectra of UO_2, UO_2-0.02 $^w/_o$ Eu_2O_3, UO_2-0.2 $^w/_o$ Eu_2O_3, UO_2-2 $^w/_o$ Eu_2O_3, pre-ground prior to the oxidative treatments.

2.1.3 Aqueous phase

The SNF is stored underwater in the spent fuel pool for up to 10 years [57], depending on the fuel design and burnup, for initial cooling. Thereafter, depending on the strategy followed by each country, it may continue at wet interim (pool) storage or it may be stored under dry interim (cask) storage conditions, for the next decades before final disposal. Boron is a neutron absorber added to the water coolant, which is required during the wet storage of SNF. Introduced in the form of boric acid (H_3BO_3) in the pool, it ensures adequate sub-criticality following a contingency principle [58]. A specified minimum boron concentration must be maintained, especially during spent fuel loading operations [58]. In this study, we compare the corrosion behaviour of Eu-doped UO_2 in two simulated pool waters, representing two different boric acid concentrations nominally containing 1600 and 3500 ppm boron, respectively. The surface corrosion behaviour is discussed from the perspective of the microstructure of the pellets.

Dissolution tests were performed in a boric acid (H_3BO_3) solution prepared from pure H_3BO_3 (99.9995%, PURATRONIC, ThermoScientific). To simulate pool storage conditions, the experiments were carried out in non-deaerated solutions in which the pH was 5.5. Details of analytical element concentration of prepared aqueous leaching solutions are shown in Table III. U Limit Of Quantification (LOQ) for all solutions, defined as the smallest concentration that can be quantified with acceptable

accuracy under certain conditions, was determined as follows: LOQ = 10 x SD (standard deviation) of the matrix blank measured by ICP-MS (inductively coupled plasma mass spectrometer). Measured conductivity, redox and pH of the two leaching solutions are also reported.

Table III Aqueous media composition.

	H_3BO_3 1600 ppm	H_3BO_3 3500 ppm
[B], mol·L^{-1}	$2.8 \cdot 10^{-2}$	$6 \cdot 10^{-2}$
[Eu], mol·L^{-1}	< LOD	< LOD
[U], mol·L^{-1}	< LOD	< LOD
Conductivity, µS/cm	3.0	3.6
Redox (Eh), V	0.500 ± 0.001	0.500 ± 0.001
pH	5.3 ± 0.1	5.1 ± 0.1

2.2 Results on the behaviour of UO_2 under dry and wet interim storage conditions

2.2.1 Dry oxidation behaviour of Eu doped UO_2-based model material as analogue for spent nuclear fuel

To assess the oxidation resistance of the prepared and ground doped fuel samples, thermal studies were carried out by thermogravimetric analysis (TGA) by using a TGA Q50 thermobalance (TA Instruments) under an O_2/N_2 flow rate of 60 mL min^{-1}. Two different O_2/N_2 gas mixtures were used during the experiments: one for low oxygen availability using 1% O_2–99% N_2 (from now on referred as 1% O_2); and the second was synthetic air 20 ± 1% O_2 – 80% N_2 (named as 21% O_2), both supplied by the company Air Liquide. The calibration of the TGA was performed for both, weight (with standard weight) and temperature (with magnetic standards [59]). Oxidations were conducted by heating the samples from room temperature up to 900 °C with a heating rate of 10 °C·min^{-1}, to obtain the complete conversion to U_3O_8 and study the overall reaction. Thermogravimetric curves were analysed by using the Universal Analysis software (TA Instruments).

In the present work, a detailed TGA of the oxidation reactions in both a synthetic air atmosphere and a low oxygen concentration up to 900 °C is reported and discussed, to show the influence of the Eu_2O_3 amount present in the sintered pellets on the oxidation kinetics. The initial Eu_2O_3 powder was analysed by the same procedure as the samples (900 °C), and no weight change was observed (Δw = 0.16 %), as expected. Additionally, pure UO_2 powder was evaluated and used as a reference. Complete oxidation TGA measurements were performed by triplicate to include uncertainties (SDs) of all mean values of the total weight change (%), oxidation onset temperatures (OOTs), maximum reaction temperatures (MRTs), and reaction rate at the maximum reaction temperature (RR_{MRT}), in addition to ensuring the repeatability and reliability of the TGA results [28, 60]. TGA oxidation curves of all the materials at the two aforementioned oxygen partial concentrations are given in Figure 7.

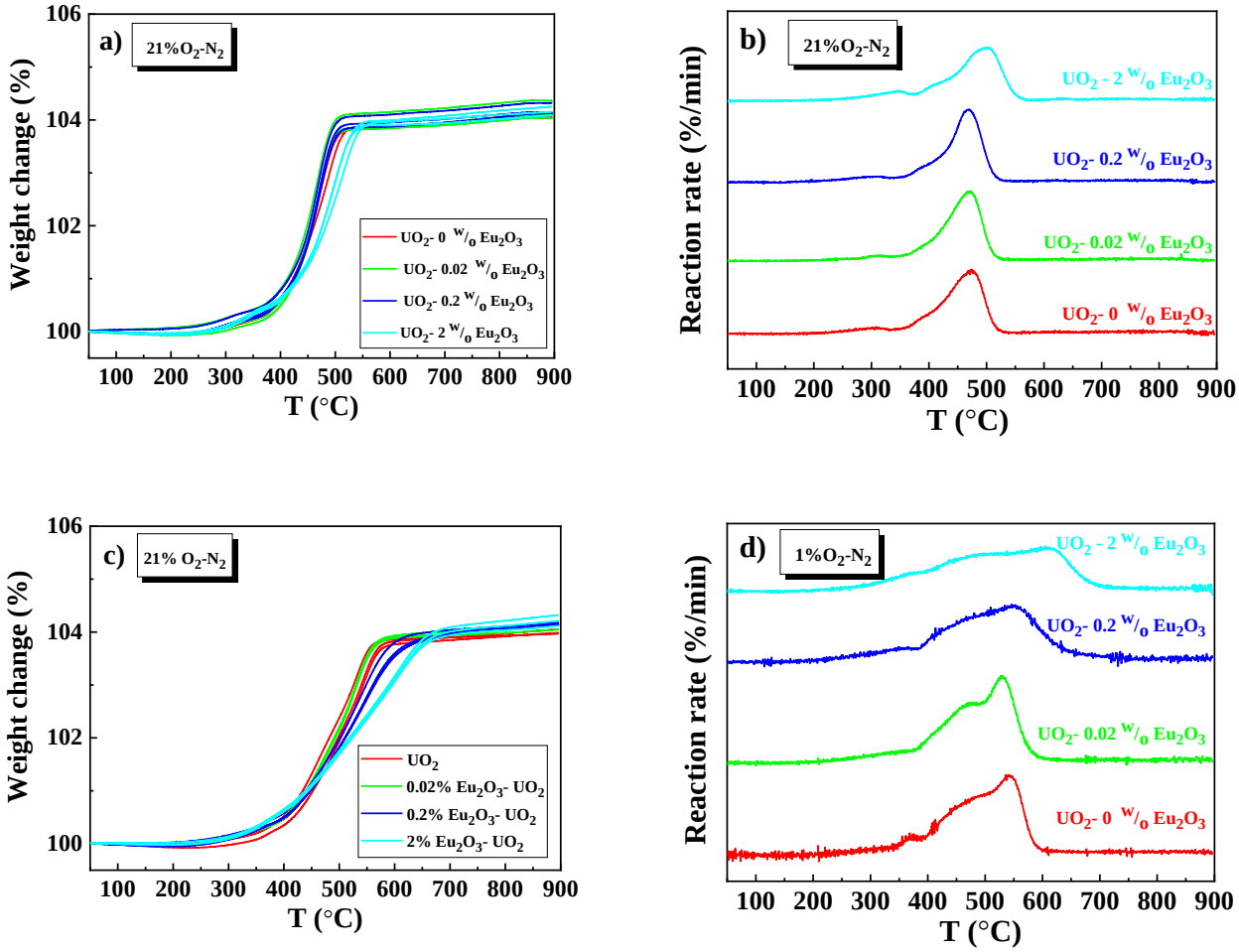

Figure 7 Weight change curves at 21%O_2 (a) and 1%O_2 (c), and reaction rates at 21%O_2 (b) and 1%O_2 (d) of: UO_2, UO_2-0.02 $^w/_o$ Eu_2O_3, UO_2-0.2 $^w/_o$ Eu_2O_3, and UO_2-2 $^w/_o$ Eu_2O_3.

Complete oxidation experiments were performed (from UO_2 to U_3O_8) by TGA. Between 350 and 600 °C, the derivative weight signal under 1 %O_2 displays a broader oxidation peak than that under 21% O_2, indicating a slower reaction rate. The calculated values from the TGA curves, *i.e.* total weight change (%), OOTs, MRTs and RRM_{RT}, are described in Table IV.

Table IV Data for the oxidation of each studied material at 21% O_2 and at 1% O_2.

MATERIAL		UO_2	0.02 $^w/_o$ Eu_2O_3-UO_2	0.2 $^w/_o$ Eu_2O_3-UO_2	2 $^w/_o$ Eu_2O_3-UO_2
21%O_2	Δm_{total} (%)	4.08 ± 0.04	4.2 ± 0.2	4.2 ± 0.1	4.2 ± 0.1
	OOT (°C)	407 ± 1	410.5 ± 0.4	415 ± 1	419 ± 2
	MRT1 (°C)	294 ± 15	293 ± 17	296 ± 11	342 ± 5
	MRT2 (°C)	479 ± 9	470 ± 2	468 ± 2	508 ± 9
	RR_{MRT} 1(%·min^{-1})	0.04 ± 0.01	0.03 ± 0.01	0.033 ± 0.003	0.07 ± 0.01
	RR_{MRT} 2 (%·min^{-1})	0.40 ± 0.03	0.45 ± 0.01	0.47 ± 0.02	0.32 ± 0.01
1%O_2	Δm_{total} (%)	4.00 ± 0.04	4.1 ± 0.1	4.15 ± 0.02	4.2 ± 0.1
	OOT (°C)	422 ± 10	425 ± 2	406± 6	388 ± 5
	MRT1 (°C)	367 ± 7	337 ± 15	350 ± 4	357 ± 2

MATERIAL		UO_2	0.02 $^w/_o$ Eu_2O_3-UO_2	0.2 $^w/_o$ Eu_2O_3-UO_2	2 $^w/_o$ Eu_2O_3-UO_2
	MRT2 (°C)	538 ± 8	530 ± 3	546 ± 2	603 ± 3
	RR_{MRT} 1(%·min^{-1})	0.06 ± 0.01	0.035 ± 0.001	0.052 ± 0.006	0.07 ± 0.02
	RR_{MRT} 2 (%·min^{-1})	0.282 ± 0.001	0.30 ± 0.02	0.21 ± 0.02	0.161 ± 0.004

Uncertainty interval represent ± 1σ from triplicate samples. The relatively low uncertainties associated with the total oxidation's onset temperature demonstrate reliability [61]. From the analysed data, it can be seen that the addition of 2 $^w/_o$ of Eu_2O_3 delays the MRT of the second oxidation stage from UO_2 to U_3O_8, when compared to pure UO_2. This effect, attributed to the dopant, is more marked with lower oxygen concentration (as low as 1% O_2).

2.2.2 Dissolution behaviour of Eu doped UO_2-based model material as analogue for spent nuclear fuel

Dissolution tests were performed under static conditions (without stirring) in PEEK vessels. The as-prepared doped UO_2 pellets were submerged in 20 mL of boric acid solutions at the two previously cited concentrations from one day up to one month and a half (48 days) to follow the progress of the reaction under air conditions and at room temperature. A high surface to volume ratio was used (S/V ~ 3700 - 8900 m^{-1}). Aliquots of the leachate were taken at different pre-defined times. A part of each aliquot was microfiltered (GHP Acrodisc, PALL, 0.22 µm) and the other part was ultrafiltered (Amicon Ultra-4 3k Millipore 1-2 nm). Both aliquots of solutions were diluted and acidified with 10% HNO_3 solution prior to the measurement.

The concentration of U in the aqueous solution was monitored by ICP-MS (Thermo Fischer Sci ICAP-Qc with QCell and KED modes). Blank tests containing only leaching solution were run under the same conditions to check for possible cross-contamination. The precise concentrations were determined using standard solutions prepared by dilution of U from a certified solution (Inorganic Ventures) of 100.14 ± 0.51 µg·L^{-1} in 1.4% v/v nitric acid. The elemental concentration was determined from three replicates and the intrinsic uncertainty was ± 15%. The normalised dissolution rates of U (R_L(U)), expressed in mg·m^{-2}·d^{-1}, were calculated from concentration data and BET surface area to calculate an elemental mass loss normalised to the SSA, following the formula given in [62].

2.2.2.1 Leachate analysis

Figure 8 shows the total U concentration as a function of time for the different model materials at 1600 ppm H_3BO_3 (Figure 8a filtered; Figure 8b ultrafiltered) and at 3500 ppm H_3BO_3 (Figure 8c filtered; Figure 8d ultrafiltered). Red symbols represent experiments with pure UO_2 and green, dark blue and light blue colours indicate that the samples used for the experiments were Eu-doped at increasing contents. The black line represents the U concentration in solution of a blank experiment.

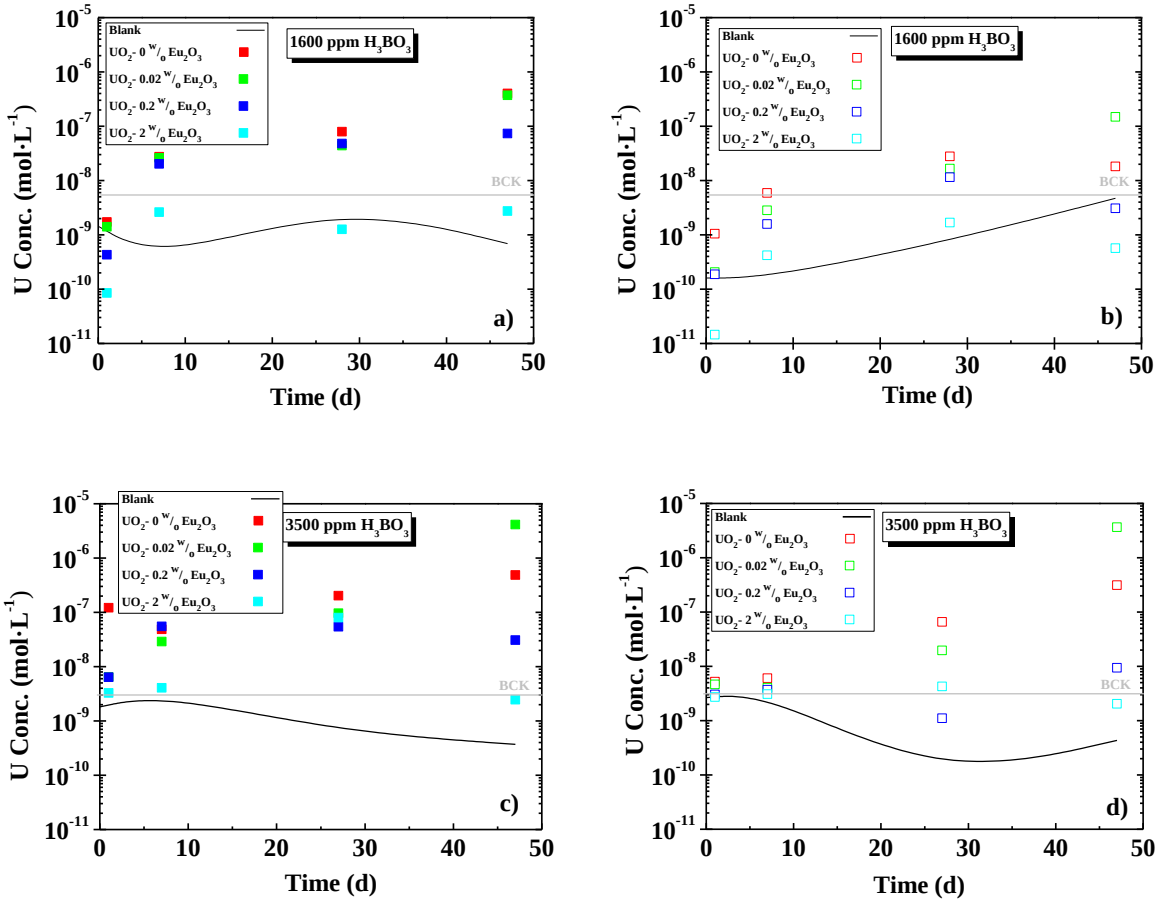

Figure 8 Total U concentrations as a function of time: (a, b) in 1600 ppm H_3BO_3 and (c, d) in 3500 ppm H_3BO_3 experiments at a temperature of 20 ± 3 °C, for UO_{2-x} $^w/_o$ Eu_2O_3 (x = 0, 0.02, 0.2, 2). U concentrations are presented in filtered (a, c) and ultrafiltered (b, d) analysed samples. Symbol code: line = blank test, red = pure UO_2 samples, green = UO_2-0.02 $^w/_o$ Eu_2O_3 samples, dark blue = UO_2-0.2 $^w/_o$ Eu_2O_3, light blue = UO_2-2 $^w/o$ Eu_2O_3. Grey lines correspond to the background U concentration in the reference solutions.

As can be seen, within the first 24 h a significant increase of the U concentration, up to $(4.4 – 8)\cdot10^{-8}$ M for UO_2 and Eu-UO_2 is observed, while after 24 h the U concentration slightly decreases and stabilises after 7 days (Figure 8). The presence of Eu seems to affect the U concentration over the entire test duration. This suggests an oxidative dissolution resistance of Eu, similar to previous findings found in the literature where other trivalent dopants like Gd are known for stabilising the UO_2 matrix towards oxidative dissolution [63, 64]. In most cases, the U concentration in the ultra-filtered samples (Figures 6b and d) represents less than 47% of the total U concentration. This difference corresponds to the formation of U bearing- colloids and it also increases after 7 days, possibly as precursors of a U secondary phase formation, which is notably emphasised at 3500 ppm H_3BO_3.

Figure 9a shows the U dissolution rate (R_L) in solution normalised to the BET surface area during the dissolution experiments. The exposed surface area was initially measured by BET (N_2) and assuming that it remains constant along the duration of the dissolution tests. Overall, the R_L(U) decreases with increasing Eu content, except the sample doped with 0.02 $^w/_o$ Eu_2O_3. The R_L(U) of undoped UO_2 was also higher than for Eu-doped UO_2. This would suggest that the presence of Eu improves the durability of UO_2, at these leachant concentrations. However, at 3500 ppm of H_3BO_3, the addition of 0.02 $^w/_o$

Eu_2O_3 seemed even to exceed the $R_L(U)$ of the undoped UO_2. In fact, the dissolution rates of the 2 $^w/_o$ Eu-doped solids at 1600 and 3500 ppm of H_3BO_3 are as low as $4 \cdot 10^{-6}$ $mg \cdot m^{-2} \cdot d^{-1}$, more than ~80 times lower than that of non-doped UO_2 in the same operating conditions (see Figure 9a).

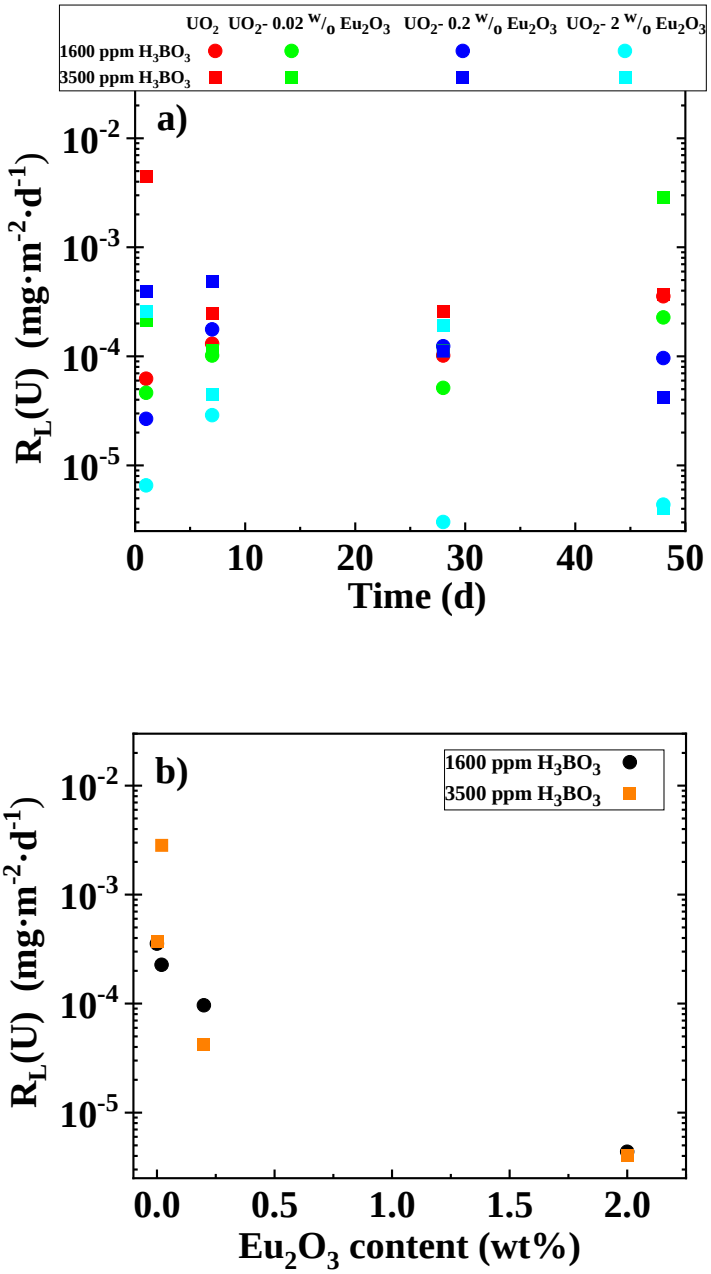

Figure 9 a) Normalised dissolution rate of U, $R_L(U)$, as a function of time, and b) final values (after 48 days of dissolution experiment) of $R_L(U)$ as a function of Eu content, for Eu-doped and undoped UO_2 dissolved in 1600 ppm and 3500 ppm H_3BO_3.

Indeed, as can be seen, the presence of Eu has an important impact on the rate of oxidation of U(IV) to U(VI). It can be hypothesised that this reduction in rate with increasing Eu is a result of a slowdown of this oxidation due to the presence of trivalent elements, which promotes and stabilises the formation of oxygen vacancy clusters (in order to maintain charge neutrality) [65], as in the case of Gd_2O_3-doped UO_2 [51, 61, 65, 66]. This effect is particularly well emphasised in Figure 9b, where final values of $R_L(U)$ (at 48 days) are plotted vs. the Eu_2O_3 concentration added. Values of the sample of UO_2

doped with 2 $^w/_o$ Eu_2O_3 are clearly the lowest, thus indicating that the presence of such quantities of Eu makes UO_2 significantly less susceptible to oxidative dissolution than those undoped or with lower Eu content under both considered H_3BO_3 concentrations.

2.2.2.2 Surface analysis of the post-leached samples

The surface of the leached samples was analysed by SEM and compared to that of not leached samples (Figure 1). No remarkable alteration was detected for undoped, 0.02 and 0.2 $^w/_o$ Eu_2O_3-UO_2 (images not shown). Conversely, examination of the 2 $^w/_o$ Eu_2O_3-UO_2 pellets surfaces revealed the presence of some kind of aggregates (Figure 10), which appeared to be formed on the pellet surface even after 1 day of dissolution experiment under both leaching solutions (1600 and 3500 ppm H_3BO_3). The evident higher abundance of these structures as a function of time and, especially, at the samples leached at 3500 ppm H_3BO_3, leads us to think that it might be related to the boric acid concentration. In addition, the fact that they were only detected for the samples with 2 $^w/_o$ Eu_2O_3 content suggests that the Eu^{3+} trivalent plays a key role in the formation of such aggregates.

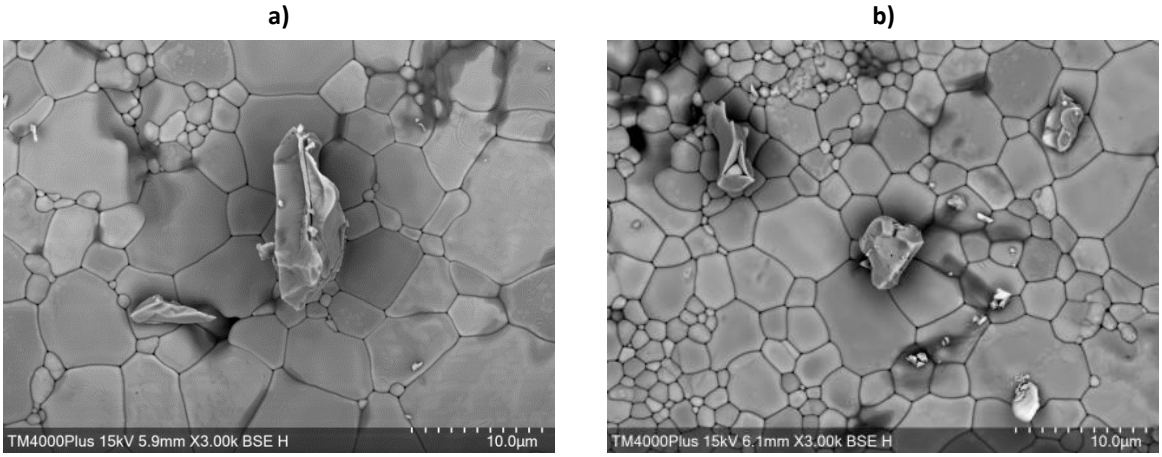

Figure 10 SEM image of a UO_2-2 $^w/_o$ Eu_2O_3 pellet surface after 1 month of dissolution experiment in (a) 1600 ppm and (b) 3500 ppm H_3BO_3.

2.3 Discussion and outcomes

A series of UO_2 pellets doped with different amounts of Eu_2O_3 (0–2 $^w/_o$) have been sintered, and analysed by XRD, BET, and SEM. In agreement with prior studies, our XRD data show that an increase in Ln dopant concentration produces a contraction of the fluorite structure possibly due to the joint effects of smaller cation size of Eu and shorter U/Eu-O bonds and/or by hypo-stoichiometry [67], showed by the Rietveld-refined lattice parameters. After characterisation, some of the pellets were crushed and milled for dry oxidation experiments, while others remained untouched for dissolution experiments. Powdered samples were also analysed by XRD, finding no differences concerning the initial pellets. Additionally, powders were also characterised by Raman spectroscopy, which confirmed the presence of oxygen vacancies in the structure as a consequence of Eu doping, demonstrated by increasing intensity of the so-called “defects band” with Eu concentration.

On the one hand, we investigated the effects of Eu doping on the thermal stability of UO_2. For this purpose, powdered samples were subjected to a thermal treatment consisting of a heating ramp up to 900 °C at two oxygen concentrations (1% and 21% O_2). These studies showed that adding Eu to UO_2

slightly retards oxidation to orthorhombic U_3O_8. Kinetic data confirm this trend, and likewise verify that lowering the oxygen concentration available delays the oxidation.

On the other hand, we studied the chemical durability of the pellets under two boric acid concentrations (1600 and 3500 ppm), mimicking some relevant wet storage conditions (spent fuel pools). The trend and values of both U concentrations and SSA normalized dissolution rates for U are similar for both leaching media, a decrease of dissolution rate with increasing Eu content in the solid solution. Post-leaching examinations by SEM of the pellets´ surface reveal that, for the samples containing 2 $^{w}/_{o}$ Eu_2O_3, some kind of aggregates appears for both boric acid concentrations, even after 1 day of dissolution. These phases formed onto the surface of the pellet need further characterisation. Nevertheless, the results point out that the trivalent dopant is directly related to the formation of such aggregates.

3. ICSM/CNRS

3.1 Samples preparation, solutions and method

3.1.1 Preparation of sintered samples of UO_2, $(U,Ln)O_2$, UO_2: PGM and UO_2: PGM+Mo

The UO_2 samples and UO_2 doped with FP (PGM, Ln, Mo) samples were prepared by using wet chemistry route, *i.e.* hydroxide precipitation. This synthesis route was developed by Martinez et al [68]. It involved a mixture of concentrated U(IV) chloride solution with PGM or Ln solutions. U (IV) chloride solution was prepared by dissolving U metal chips in 6 mol·L^{-1} HCl. The concentration of the solution was finally estimated to 0.62 ± 0.01 mol.L^{-1}. PGM solution (0.1 mol·L^{-1}) was obtained by dissolution of ruthenium (III), rhodium (III) or palladium (II) chloride in 1 mol·L^{-1} HCl. The Ln stock solutions (0.5 mol·L^{-1}) were prepared by dissolving trivalent lanthanum, cerium, praseodymium, neodymium or yttrium chloride salts in 1 mol·L^{-1} HCl whereas that of molybdenum (0.05 mol·L^{-1}) was prepared by dissolving molybdenum (III) chloride salt in 1 mol·L^{-1} HCl.

The associated elemental concentrations were determined by ICP-AES. The PGM elements were introduced to the U (IV) solution considering a global content of 3 mol % and with a distribution representative from SNF, *i.e.* Rh (10%), Pd (36%) and Ru (54%). This mixture was then added in an excess of 400% ammonia. For Ln elements, which account for nearly 1 mol % in SNF [69, 70], we chose a representative distribution, *i.e.* Nd (42%), Ce (26%), La (13%), Pr (12%) and Y (7%). In order to enhance the impact of these elements on the chemical durability of UO_2 and to make easier the characterization of the solid phases, several mole loadings were considered, *i.e.* 2, 6, 10 and 25 mol % (these later values being deliberately higher than those encountered in SNF).

After stirring at room temperature, the hydroxide precipitates were separated from the supernatant by centrifugation. Then, they were washed twice with water and once with ethanol, and finally dried in air. Hydroxide based precursors were converted to oxide by heating at 700 °C for 4 hours under reducing atmosphere (Ar – 4% H_2). The powder (≈ 200 mg) was then shaped by uniaxial pressing (500 MPa) and finally sintered at 1500 °C (for UO_2 samples containing PGM) or at 1600 °C (for UO_2 and $(U,Ln)O_2$ samples) during 4 hours under reducing atmosphere (Ar – 4% H_2) to prepare dense pellets.

3.1.2 Characterization of powdered and sintered samples of UO_2, $(U,Ln)O_2$, UO_2: PGM and UO_2: PGM+Mo

The contents of each elements was determined in the starting precursors by ICP-OES after the full dissolution of a small quantity of powder (≈ 10 mg) in 4 mol·L^{-1} HNO_3. Each resulting solution was diluted with 0.2 mol·L^{-1} HNO_3 before performing the analysis. The SSA of all the prepared powders was characterized before sintering by N_2 (g) or Kr(g) adsorption using the BET method.

The samples were characterized by PXRD using a Bruker D8 diffractometer equipped with a Lynx-eye detector adopting the parallel geometry (reflection mode) and using Cu $K\alpha_{1,2}$ radiation (λ = 1.54184 Å). The patterns were recorded at room temperature ($10° < 2\theta < 60°$, step: 0.02°, total counting time: 2.0 hours). All the PXRD patterns were refined by the Rietveld method using the Cox-Hastings pseudo-

Voigt profile function implemented in the Fullprof_suite program. The samples were also often characterized by Raman spectrometry by the means of a Horiba-Jobin Yvon Aramis apparatus equipped with an edge filter. The acquisition of the spectra was performed at λ = 633 nm with a D = 0.6 filter in order to avoid any degradation of the sample.

The microstructure of the sintered samples was studied by SEM using a FEI Quanta 200 environmental (ESEM) equipment with a SE or BSD detectors under vacuum conditions. An accelerating voltage of 25 kV and several magnifications were considered. Moreover, cationic homogeneity was evaluated at the surface of the pellets by SEM-EDX.

Open porosity was determined by helium pycnometry using a Micrometrics – AccuPyc II 1340 apparatus, whereas geometrical determinations were conducted using an electronic calliper to access the global porosity, thus also the closed porosity. SEM micrographs recorded at low magnification were used to evaluate the initial SSA (S_{SA}, expressed in $m^2\ g^{-1}$) of the pellets using the SESAM method [71]. For this, five images of 92 μm × 62 μm were binarized using the FiJi software to determine the surface area of the pores observed in the investigated domains. The pore diameter distributions were evaluated from these images using the "analyse particles" plugin. Then, the surface area associated to the pores was obtained assuming that the pore size distribution of the analysed domain was representative of the whole sample and that the pores were cylindrical. Moreover, the depth of the pores was determined in order to respect the open porosity developed by all the open pores (obtained by helium pycnometry). Then, the resulting surface area was divided by the mass of the sample in order to access to the SSA. For each sample, an average value of the SSA was deduced from the analysis of the five images recorded at low magnification.

3.1.3 Dissolution tests of sintered samples of UO_2, $(U,Ln)O_2$, UO_2: PGM and UO_2: PGM+Mo

Dissolution tests were carried out at 50 °C or at 70 °C under static conditions with mechanical stirring, using 125 mL PFA reactors (Savillex). For each studied system, half of a pellet (about 100 mg) was placed in 60 mL of a 2500 ppm boric acid solution ($2.3 \cdot 10^{-4}$ mol L^{-1} H_3BO_3) at pH = 5 and the other half pellet was put in contact with 60 mL of a solution composed of boric acid ($2.3 \cdot 10^{-1}$ mol·L^{-1}). Lithine LiOH ($5.0 \cdot 10^{-4}$ mol·L^{-1}) was introduced in a series of the leaching solutions in order to adjust the pH to 7. Both boric acid and lithine solutions were prepared by dissolving H_3BO_3 and LiOH, respectively.

At regular time intervals (once a week for the first 150 days and then once a month for longer dissolution times), 6 mL of solution was withdrawn then replaced by the same volume of fresh solution. The samples were then acidified to reach a concentration of 0.2 mol·L^{-1} HNO_3 in the analysed samples. The elementary U concentrations were analysed in the samples by ICP-AES. Calibration was obtained using standard solutions prepared by dilution of a certified standard solution of 1000 mg U L^{-1} in 0.2 mol L^{-1} HNO_3. The U concentration was then calculated as the average of the three replicates at each wavelength. The experimental uncertainty was estimated to be twice the SD of nine U elemental concentration measurements. The elemental concentrations of PGM elements (ruthenium, rhodium and palladium) and Ln elements were measured by an ICP-MS calibrated for the isotopes ^{99}Ru, ^{101}Ru, ^{102}Ru, ^{103}Rh, ^{105}Pd, ^{106}Pd, ^{108}Pd, ^{89}Yu, ^{139}La, ^{141}Pr, ^{140}Ce, ^{143}Nd, ^{144}Nd, ^{145}Nd and ^{146}Nd using several standard solutions prepared by diluting 1000 mg.L^{-1} in 0.2 mol·L^{-1} HNO_3. In addition, ^{193}Ir and ^{209}Bi were

used as internal standards. Elemental concentrations were calculated from the average mass of three replicates. Experimental uncertainties were estimated as twice the SD of the measurements.

The relative mass of dissolved material at a given time t, $\Delta m_i/m_0$ (in wt %) was calculated using the elemental concentration as follows:

$$\Delta m_i(t)/m_0 = \frac{m_i(t)}{f_i \times m_0} \times 100 = \frac{C_i(t) \times V}{f_i \times m_0} \times 100 \qquad (2)$$

where $m_i(t)$ corresponds to the total amount of the element *i* released in the solution for a given time t, calculated from the elementary concentration, $C_i(t)$ (g L^{-1}), and the volume of solution in contact with the solid, V (L). In this expression, f_i (g.g^{-1}) is the mass fraction of the element *i* in the solid and m_0 is the initial mass of the pellet (g).

According to literature, the normalised weight losses, $N_L(i)$ (g.m^{-2}) were calculated from the elemental concentrations as follows:

$$N_L(i) = \frac{m_i(t)}{f_i \times m_0 \times S_{SA}} \qquad (3)$$

Where S_{SA} (m^2.g^{-1}) denotes the initial SSA of the solid measured by images analysis. It is worth noting that f_i and S_{SA} (m^2.g^{-1}) were considered to remain constant during the dissolution tests. The normalized dissolution rate, R_L(i) (g.m^{-2}.d^{-1}), is defined as the time-derivative of the normalized mass loss, *i.e.*:

$$R_L(i,t) = \frac{d\,N_L(i,t)}{d\,t} \qquad (4)$$

The overall protocol of the dissolution tests is summarized in Figure 11.

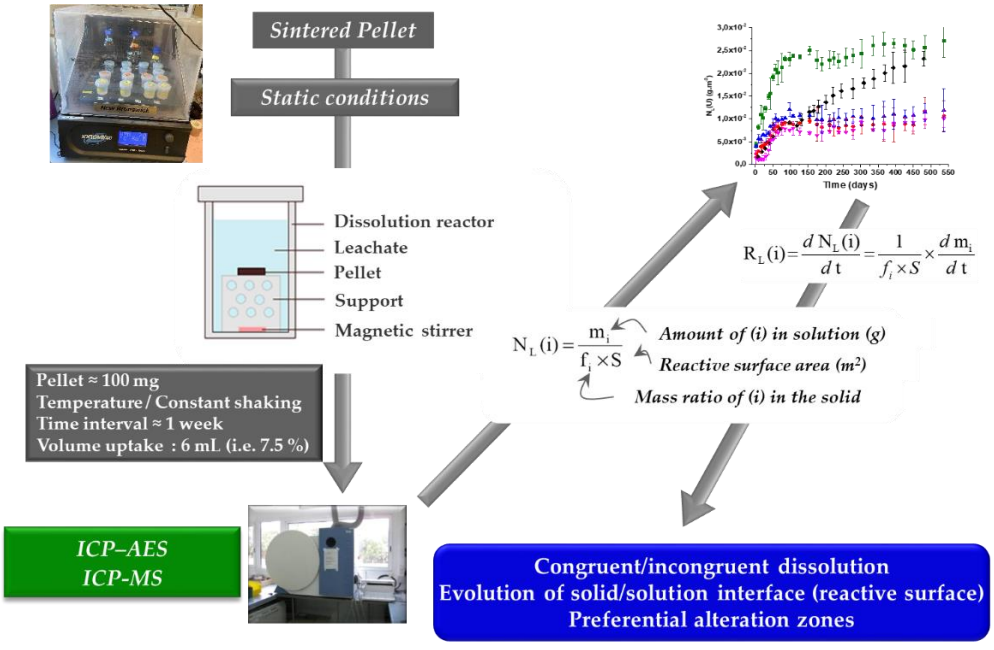

Figure 11 Schematic representation of the dissolution tests protocol performed on sintered pellets.

From the concentration of the elements present in the dissolved reactor, calculations of saturation index of the U phases were finally carried out via the PHREEQC software (version 3.3.8.11728) associated with the ThermoChimie database (version 10a) developed by ANDRA [72] . All the

calculations were developed taking in account the absence of carbonate ions in the leaching solution.

3.2 Results on the behaviour of UO_2, $(U,Ln)O_2$, UO_2: PGM and UO_2: PGM+Mo under wet interim storage conditions

3.2.1 Synthesis and characterisation of sintered samples

For all the elements considered, the precipitation of hydroxide precursor was quantitative except for Y, leading to the preparation of sintered samples with the expected compositions. As instance, the recovery yields were found near to 99.9 % for U and Ln elements and ranged between 85 and 100 % for the PGM elements. After precipitation then drying, the precipitate was found to be highly reactive [68] (120-150 $m^2 \cdot g^{-1}$) and composed of crystallites of 2-5 nm in size. Heating the powders at 700 °C for 4 hours under reducing conditions, led to powders rather appropriate for sintering purpose, with SSA (13 to 22 $m^2 \cdot g^{-1}$) prior to the final sintering step. From refinement of XRD patterns, the unit cell parameters of the powders were in agreement with that expected. First, for UO_2:PGM sample, the obtained value (a = 5.462 Å) did not differ significantly from that determined for UO_2 (a = 5.469 Å) which appears in agreement with the fact that PGM elements were not incorporated in the fluorite structure and formed separated phases (which were found to be metallic alloys from X-EDS mapping). (Figure 12). On the contrary, the incorporation of Ln elements in the fluorite structure induced a slight decrease of the unit cell parameter (from a = 5.469 Å to a = 5.444 Å when incorporating about 25 mol % of the Ln mixture). This is also in agreement with the recent results reported in literature during the synthesis of $(U,Nd)O_2$ solid solutions [73]. Finally, the unit cell parameters obtained for the samples containing molybdenum is slightly lower (a = 5.445 Å) which underlines that at this temperature, the powdered samples remain slightly hyper-stoichiometric, which surely results from the storage conditions (air) of the initial precipitate or during the heating treatment. The hyper-stoichiometry of powder prepared by this chemical way of synthesis was recently reported on $(U,Ce)O_2$ samples or on $(U,Ln)O_2$ samples [74, 75]. Several physico-chemical properties of the powders obtained after thermal conversion at 700 °C are reported in Table V, whereas that of the sintered pellets prepared at 1500 or 1600 °C are gathered in Table VI.

Table V Conditions of thermal conversion of the starting hydroxide precursors. SSA and unit cell parameters of the powders obtained after conversion at 700 °C.

System	Synthesis route	Thermal conversion	SSA ($m^2.g^{-1}$)	Unit cell parameter (Å)
UO_2	Hydroxide precipitation	T = 700 °C t = 4 hours Atmosphere: Ar – 4% H_2	17	5.469
$(U,Ln)O_2$, 2 mol % Ln			15	5.455
$(U,Ln)O_2$, 6 mol % Ln			17	5.451
$(U,Ln)O_2$, 10 mol % Ln			17	5.446
$(U,Ln)O_2$, 25 mol % Ln			22	5.444
UO_2 + 3 mol % PGM			13	5.462
UO_2 + 3 mol % PGM + 2 mol % Mo			13	5.445
UO_2 + 3 mol % PGM + 2 mol % Mo + 3 mol % Ln			13	5.444

From Table VI, it appears that the densification rate was high for UO_2 and $(U,Ln)O_2$ samples, with relative density ranging from 93 % to 97 % of the value calculated from XRD. At this operating

temperature (1600 °C), the sintering was thus complete. On the contrary, due to the presence of palladium in the PGM mixture (which volatilization is near to 1600 °C), the temperature of sintering was reduced to 1500 °C for UO_2:PGM materials. This temperature decrease induced a decrease of the relative densification rate, with value decreasing to 88 - 90%. Simultaneously, the SSA of the prepared pellets was evaluated by the SESAM method. It was found between $2 \cdot 10^{-2}$ $m^2 \cdot g^{-1}$ for the more densified pellets and 10^{-1} $m^2 \cdot g^{-1}$ for the less densified materials. Such values are higher by two decades than the pure geometrical SSA value (about $3 \cdot 10^{-4}$ $m^2 \cdot g^{-1}$). X-EDS mapping of the sintered pellets were also performed to check the distribution of FP at the surface of unpolished sintered pellets of UO_2:PGM and $(U,Ln)O_2$. The results are presented in Figure 12. They clearly showed that Ln elements are well distributed in the $(U,Ln)O_2$ pellet, leading to homogeneous materials. On the contrary, PGM elements are forming metallic particles, which correspond to Rh-Ru-Pd alloys and are comparable to the ε particles observed in SNF [23]. Both results are in good agreement with the data obtained by PXRD, showing the incorporation of Ln in the fluorite structure, which is not the case for PGM elements.

Table VI Sintering conditions as well as density and SSA of the final sintered pellets.

System	Sintering step	Density (%)	SSA ($m^2.g^{-1}$)
UO_2	Uniaxial pressing: 500 MPa T = 1600 °C t = 4 hours Atmosphere: Ar – 4% H_2	95 ± 2	$2.0 \cdot 10^{-2}$
$(U,Ln)O_2$, 2 mol % Ln		96 ± 2	$2.0 \cdot 10^{-2}$
$(U,Ln)O_2$, 6 mol % Ln		96 ± 2	$2.0 \cdot 10^{-2}$
$(U,Ln)O_2$, 10 mol % Ln		97 ± 2	$2.0 \cdot 10^{-2}$
$(U,Ln)O_2$, 25 mol % Ln		93 ± 2	$2.1 \cdot 10^{-2}$
UO_2 + 3 mol % PGM		89 ± 2	$8.0 \cdot 10^{-2}$
UO_2 + 3 mol % PGM + 2 mol % Mo		90 ± 2	$8.0 \cdot 10^{-2}$
UO_2 + 3 mol % PGM + 2 mol % Mo + 3 mol % Ln		90 ± 2	$1.0 \cdot 10^{-1}$

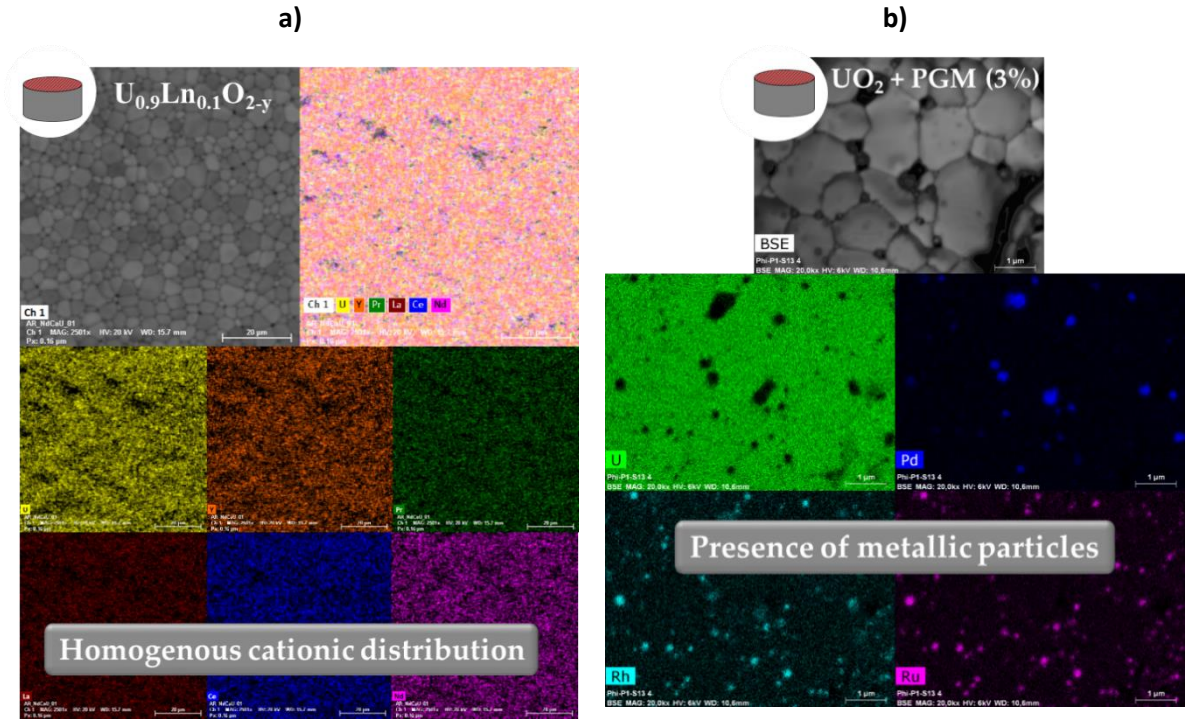

Figure 12 X-EDS mapping recorded at the surface of sintered samples of UO_2:PGM (a) and (U,Ln)O_2 (b).

3.2.2 Long-term behaviour of sintered samples

All the prepared sintered samples were submitted to long-term dissolution tests in deionized water, in a solution containing boric acid (2500 ppm, *i.e.* $2.3 \cdot 10^{-4}$ mol·L^{-1} H_3BO_3, pH = 5) and in a solution containing boric acid and lithin ($2.3 \cdot 10^{-4}$ mol·L^{-1} H_3BO_3, LiOH, pH = 7). Two temperatures (50 °C and 70 °C) were considered. All the normalised dissolution rates determined at 50 °C are gathered in Table VII, whereas several examples of associated dissolution curves obtained are presented for: UO_2 (H_3BO_3 + LiOH, pH = 7) (Figure 13); (U,Ln)O_2 (H_3BO_3 + LiOH, pH = 7) (Figure 14); UO_2: PGM (H_3BO_3 + LiOH, pH = 7) (Figure 15) ; UO_2: PGM+Mo (H_3BO_3, pH = 5) (Figure 16); and (U,Ln)O_2: PGM+Mo+Ln (deionized water) (Figure 17).

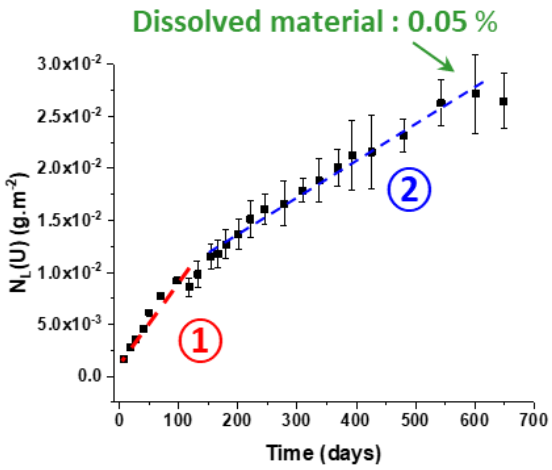

Figure 13 Dissolution test of UO_2 (reference material) obtained at 50 °C, at pH =7, in the presence of H_3BO_3 and LiOH.

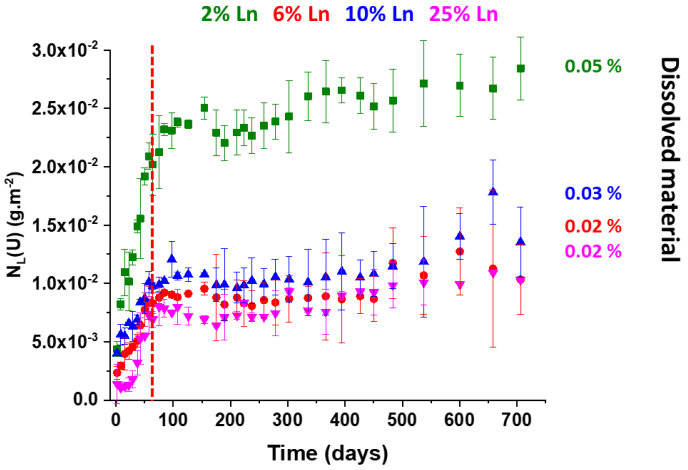

Figure 14 Dissolution test of $(U,Ln)O_2$ (with 2, 6, 10, 25 mol % Ln) obtained at 50 °C, at pH =7, in the presence of H_3BO_3 and LiOH.

First, the dissolution tests performed on UO_2 and $(U,Ln)O_2$ at pH = 7 (Figure 13 and Figure 14) revealed the existence of a slope break when plotting the evolution of the normalized weight loss $N_L(U)$. The associated normalized dissolution rates decreased by a factor of 3 for UO_2 for dissolution times longer than 100 days. This break appeared earlier for $(U,Ln)O_2$ (*i.e.* for t > 60 days) and was stronger (decrease by a factor of 12 to 30), leading to very low normalized dissolution rates (typically in the range of 5-8·10^{-6} $g \cdot m^{-2} \cdot d^{-1}$). This suggest a beneficial impact of Ln elements on the chemical durability of the ceramics for the three conditions examined. This decrease could be attributed to the formation of neoformed phase at the surface of the $(U,Ln)O_2$ solid solutions. The associated U concentration at saturation reached 6.7·10^{-7} $mol \cdot L^{-1}$. For UO_2, normalized dissolution rate was found to be slower by a factor of 5 at pH = 7 than at pH = 5. This difference was reduced for Ln doped UO_2 materials. One possible factor is that the higher dissolution rates observed at the early beginning of the dissolution could result from less durable zones of the material (including hyper-stoichiometric domains, crystal defects potentially present in the grains boundaries).

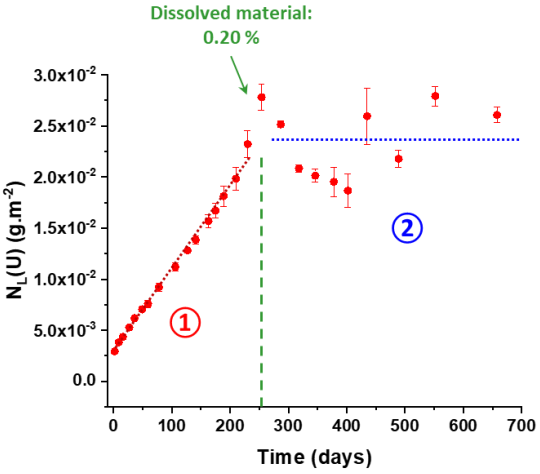

Figure 15 Dissolution test of UO_2: PGM obtained at 50 °C, at pH =7, in the presence of H_3BO_3 and LiOH.

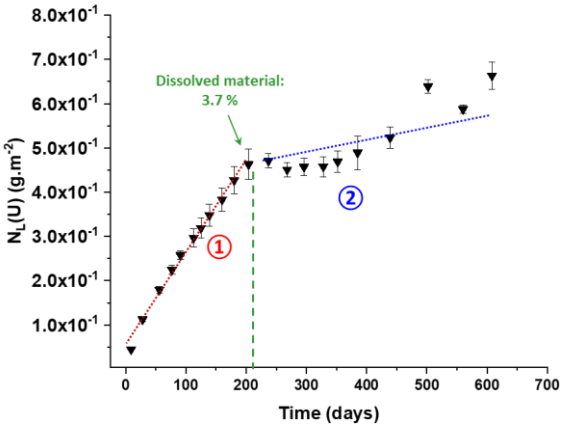

Figure 16 Dissolution test of UO_2:PGM+Mo obtained at 50 °C, at pH =5, in the presence of H_3BO_3.

For UO_2:PGM ceramics (Figure 15), no slope break was observed until 250 days of dissolution time. Above this dissolution time, a plateau was clearly observed suggesting the formation of neo-formed phase. The beginning of this plateau corresponds of a relative dissolution mass of the material equal to 0.20 wt % and then to a U concentration at saturation of $7.5 \cdot 10^{-6}$ mol·L^{-1}. The direct comparison of the results obtained for UO_2 and UO_2:PGM showed no effect of PGM elements when leaching at pH =7, while a factor of 4 to 5 was obtained at pH = 5 (Figure 16). As observed for pure UO_2, UO_2:PGM dissolved 25 to 30 times more slowly at pH = 7, compared to pH ≈ 5, whatever the presence (or not) of boric acid in the leaching solution. Moreover, for this kind of materials, normalized dissolution rates were almost similar in the presence (or not) boric acid. According to the literature, PGM elements are very often associated with the existence of catalytic phenomena, leading in particular to the oxidation of U (IV) to U (VI) [76, 77]. It is important to point out that this results in a much higher concentration of U at saturation than in the case of (U,Ln)O_2 solid solutions. Finally, the dissolution rate of sintered samples of UO_2:PGM increases by a factor less than 1.5 at pH = 7, than 4 at pH = 5 in the presence of boric acid, and 7 in deionized water compared to pure UO_2.

Comparison of the results of dissolution of UO_2:PGM with that of UO_2:PGM+Mo in the three studied media did not reveal any significant impact of molybdenum while the normalized dissolution rates were almost the same (less than a factor of 2 was noted). Additionally, the comparison of the results obtained at pH = 5 in the presence of boric acid and in deionized water confirmed that boric acid did not affect significantly the normalized dissolution rates of the ceramics.

Contrarily to molybdenum and as it has been noticed for (U,Ln)O_2 samples, the presence of Ln elements leads to the significant decrease of the normalized dissolution rate. Indeed, the direct comparison of the dissolution tests performed for UO_2:PGM+Mo, on the one hand and for UO_2:PGM+Mo + Ln on the other hand revealed that the normalized dissolution rates were reduced by about one decade for the three studied leaching solutions. This effect could result from the U speciation in the sintered materials, which is strongly affected by the presence of Ln elements.

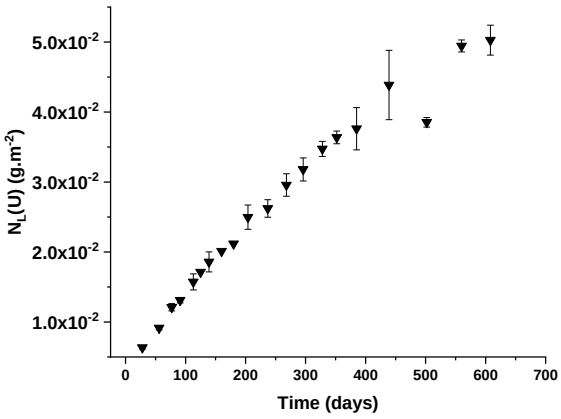

Figure 17 Dissolution test of UO_2:PGM+Mo+Ln obtained at 50 °C, at pH =5.3, in deionized water.

Table VII Results of dissolution tests performed at T = 50 °C. All the normalized dissolution rates are expressed in $g \cdot m^{-2} \cdot d^{-1}$. t_{TOT} corresponds to the global duration of the leaching time, t_1 corresponds to the time at which a break in slope is observed (when observed). Normalized dissolution rate obtained before and after t_1 are indicated in bold or italic, respectively.

System	H_3BO_3 (2500 ppm) + LiOH pH = 7		H_3BO_3 (2500 ppm) pH = 5	H_2O pH = 5.3	
UO_2	t_{TOT} = 887 d	t_1 = 100 d	t_{TOT} = 887 d	t_{TOT} = 887 d	
	$R_L(U) = 1.0 \cdot 10^{-4}$		$R_L(U) = 5.0 \cdot 10^{-4}$	$R_L(U) = 2.0 \cdot 10^{-4}$	
	$R_L(U) = 3.0 \cdot 10^{-5}$				
$(U,Ln)O_2$ 2%	t_{TOT} = 944 d	t_1 = 60 d	t_{TOT} = 944 d $R_L(U) = 5.0 \cdot 10^{-4}$	t_{TOT} = 944 d	t_1 = 400 d
	$R_L(U) = 2.0 \cdot 10^{-4}$			**$R_L(U) = 1.0 \cdot 10^{-4}$**	
	$R_L(U) = 8.0 \cdot 10^{-6}$			*$R_L(U) = 4.0 \cdot 10^{-5}$*	
$(U,Ln)O_2$ 6%	t_{TOT} = 944 d	t_1 = 60 d	t_{TOT} = 944 d $3.0 \cdot 10^{-6} \leq R_L(U) \leq 8.0 \cdot 10^{-6}$	t_{TOT} = 944 d	t_1 = 200 d
	$R_L(U) = 1.0 \cdot 10^{-4}$			**$R_L(U) = 3.0 \cdot 10^{-4}$**	
	$R_L(U) = 5.0 \cdot 10^{-6}$			*$R_L(U) = 2.0 \cdot 10^{-4}$*	
$(U,Ln)O_2$ 10%	t_{TOT} = 944 d	t_1 = 60 d		t_{TOT} = 944 d	t_1 = 400 d
	$R_L(U) = 1.0 \cdot 10^{-4}$			**$R_L(U) = 1.0 \cdot 10^{-4}$**	
	$R_L(U) = 8.0 \cdot 10^{-6}$			*$R_L(U) = 4.0 \cdot 10^{-5}$*	
$(U,Ln)O_2$ 25%	t_{TOT} = 944 d	t_1 = 60 d		t_{TOT} = 944 d	
	$R_L(U) = 1.0 \cdot 10^{-4}$			$R_L(U) = 6.0 \cdot 10^{-6}$	
	$R_L(U) = 6.0 \cdot 10^{-6}$				

System	H_3BO_3 (2500 ppm) + LiOH pH = 7		H_3BO_3 (2500 ppm) pH = 5		H_2O pH = 5.3	
UO_2 + 3 % PGM	t_{TOT} = 895 d	t_1 = 250 d	t_{TOT} = 895 d	t_1 = 100 d	t_{TOT} = 895 d	t_1 = 100 d
	$R_L(U) = 1.0 \cdot 10^{-4}$		**$R_L(U) = 2.5 \cdot 10^{-3}$**		**$R_L(U) = 2.9 \cdot 10^{-3}$**	
	$R_L(U) = 2.0 \cdot 10^{-5}$		*$R_L(U) = 6.0 \cdot 10^{-4}$*		*$R_L(U) = 5.0 \cdot 10^{-4}$*	
UO_2 + PGM + Mo	t_{TOT} = 846 d		t_{TOT} = 846 d	t_1 = 200 d	t_{TOT} = 846 d	t_1 = 200 d
	$R_L(U) = 5.0 \cdot 10^{-5}$		**$R_L(U) = 2.1 \cdot 10^{-3}$**		**$R_L(U) = 1.3 \cdot 10^{-3}$**	
			$R_L(U) = 6.0 \cdot 10^{-4}$		*$R_L(U) = 3.0 \cdot 10^{-4}$*	
UO_2 + PGM + Mo + Ln	t_{TOT} = 846 d		t_{TOT} = 846 d		t_{TOT} = 846 d	
	$R_L(U) = 8.0 \cdot 10^{-6}$		$R_L(U) = 5.0 \cdot 10^{-5}$		$R_L(U) = 8.0 \cdot 10^{-5}$	

3.2.3 Saturation experiments: characterization of neoformed phases and speciation calculations

For several leaching conditions and leached materials, the formation of neoformed phases was suggested by the existence of a plateau, which was finally observed when plotting the evolution of the normalised weight loss. The experimental conditions that led to saturation phenomena in the solution are listed in Table VIII. Especially, these results clearly underline that dissolution tests performed at pH = 7 are favourable to the rapid establishment of saturation conditions for $(U,Ln)O_2$ (t > 60 days) and UO_2:PGM (t > 250 days) sintered pellets. Moreover, saturation conditions have been also reached for this latter system when performing the dissolution tests at pH = 5 in the presence of 2500 ppm boric acid and in deionized water. This observation has to be connected to the higher dissolution rates obtained for UO_2:PGM compared to the other systems, leading more rapidly to the saturation concentration of U in solution (and surely to the slight difference in terms of microstructure between UO_2 and UO_2:PGM sintered samples). Finally, it is also worth noting that no saturation conditions have been reached for pure UO_2 even after almost 900 days of dissolution time in the three studied media.

Table VIII Conditions associated to the potential saturation of the solution based on macroscopic analysis in solution and associated U concentrations at equilibrium.

System	H_3BO_3 (2500 ppm) + LiOH pH = 7	H_3BO_3 (2500 ppm) pH = 5	H_2O pH = 5.3
UO_2	No saturation		
$(U,Ln)O_2$ 2%	Saturation – t ≥ 60 days $[U]_{saturation} = 7.8 \cdot 10^{-7}$ M	No saturation	
$(U,Ln)O_2$ 6%	Saturation – t ≥ 60 days $[U]_{saturation} = 6.7 \cdot 10^{-7}$ M	No saturation	

System	H_3BO_3 (2500 ppm) + LiOH pH = 7	H_3BO_3 (2500 ppm) pH = 5	H_2O pH = 5.3
$(U,Ln)O_2$ 10%	Saturation – t ≥ 60 days $[U]_{saturation} = 8.8 \cdot 10^{-7}$ M	No saturation	
$(U,Ln)O_2$ 25%	Saturation – t ≥ 60 days $[U]_{saturation} = 5.5 \cdot 10^{-7}$ M	No saturation	
UO_2 + 3 % PGM	Saturation – t ≥ 250 days $[U]_{saturation} = 7.5 \cdot 10^{-6}$ M	Saturation – t ≥ 250 days $[U]_{saturation} = 1.1 \cdot 10^{-4}$ M	Saturation – t ≥ 160 days $[U]_{saturation} = 3.1 \cdot 10^{-5}$ M
UO_2 + PGM + Mo	No saturation	Saturation – t ≥ 200 days $[U]_{saturation} = 1.2 \cdot 10^{-4}$ M	Saturation – t ≥ 180 days $[U]_{saturation} = 6.5 \cdot 10^{-5}$ M
UO_2 + PGM + Mo + Ln	No saturation		

The saturation conditions suggested by elemental analysis of concentrations in the leachate were confirmed with the help of operando monitoring by ESEM of the solid/solution interface. To this end, a pellet was placed in contact with the leaching solution for a given time, and then extracted from the solution before being rinsed with water to stop the dissolution reaction. Excess water was removed by contact with absorbent paper. The pellet was then characterized by SEM. It was then re-contacted in the same medium to continue dissolving the sample. Wherever possible, the same zone was followed during sample leaching. Two examples are presented for $(U,Ln)O_2$ and UO_2:PGM sintered samples leached at pH = 7 (*i.e.* in the presence of 2500 ppm H_3BO_3 + LiOH) in Figure 18 and in Figure 19, respectively.

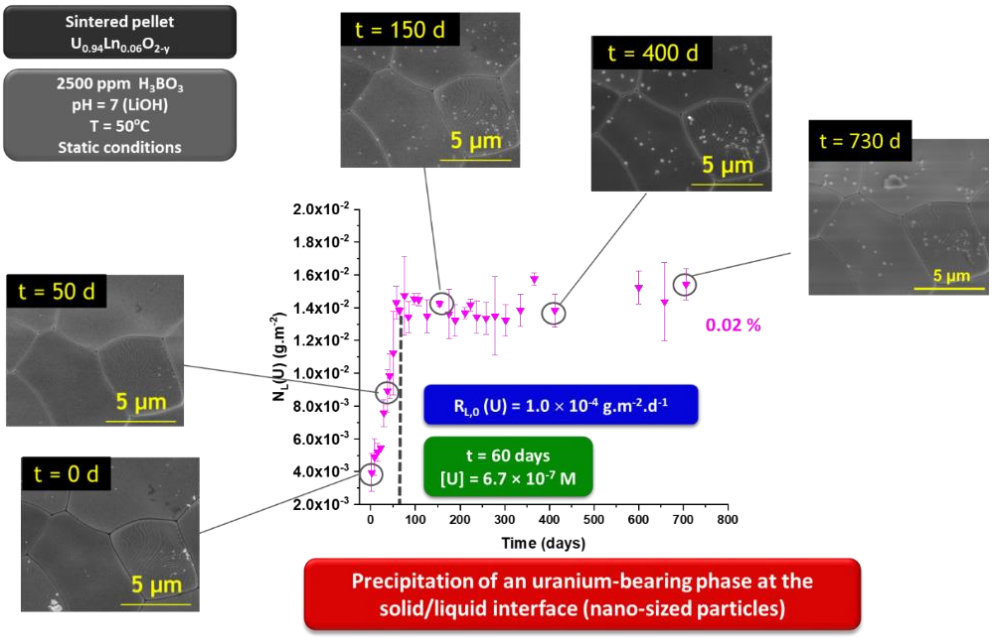

Figure 18 Operando monitoring of the evolving surface of $(U,Ln)O_2$ obtained at 50 °C, at pH =7, in the presence of H_3BO_3 and LiOH.

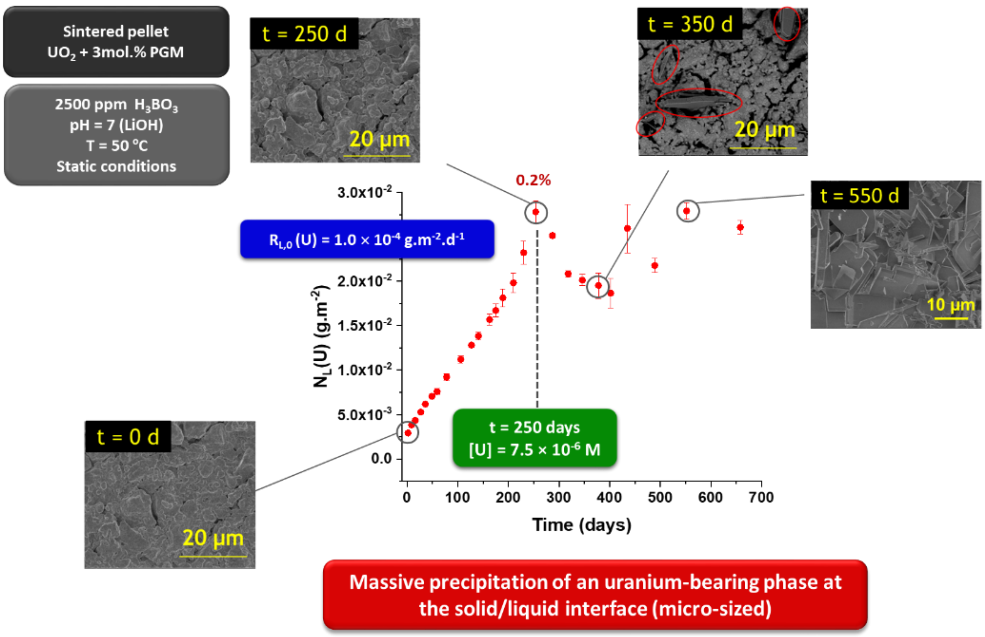

Figure 19 Operando monitoring of the evolving surface of UO_2:PGM obtained at 50 °C, at pH =7, in the presence of H_3BO_3 and LiOH.

Operando monitoring carried out during the dissolution of $(U,Ln)O_2$ solid solutions (with 6 mol % Ln) at 50 °C, pH = 7 and in the presence of boric acid and lithine (Figure 18) reveals that saturation conditions are reached as early as 60 days. After this time, a plateau is clearly observed, suggesting the existence of a neoformed phase containing U. At the same time, surface analyses revealed the existence of small nodules (less than a few tens of nanometres in size). However, the too small size of these nodules did not allow identifying this neoformed phase, even after 450 days of dissolution. It is worth noting that the quantity of neoformed nodules was not significantly increased when extending the dissolution time up to 730 days. Some complementary attempts to characterize these neoformed phases are now under progress.

Conversely, operando monitoring by ESEM during dissolution of UO_2:PGM samples at 50 °C, pH = 7 and in the presence of boric acid and lithine (Figure 19), highlighted the increase of the normalized weight loss up to 250 days. Beyond this dissolution time, a decrease in the U concentration was observed, indicating the clear existence of saturation phenomena. In this case, the crystals formed onto the surface of the leached material took the form of platelets and eventually covered the entire surface of the sample after 550 days of dissolution. The size as well as the crystalline state of the crystals neoformed enabled the complete characterization of this phase, as it will be shown later. The characterisation of the neoformed phase on the surface of UO_2:PGM was thus possible during dissolution tests performed at pH = 7 in the presence of boric acid and lithine and at pH = 5 in the presence of boric acid. The leached samples were thus characterised by XRD, ESEM and Raman spectroscopy.

When dissolving at pH = 7, XRD analysis of the fully covered surface suggested the formation of a neoformed phase comparable to becquerelite (Figure 20).

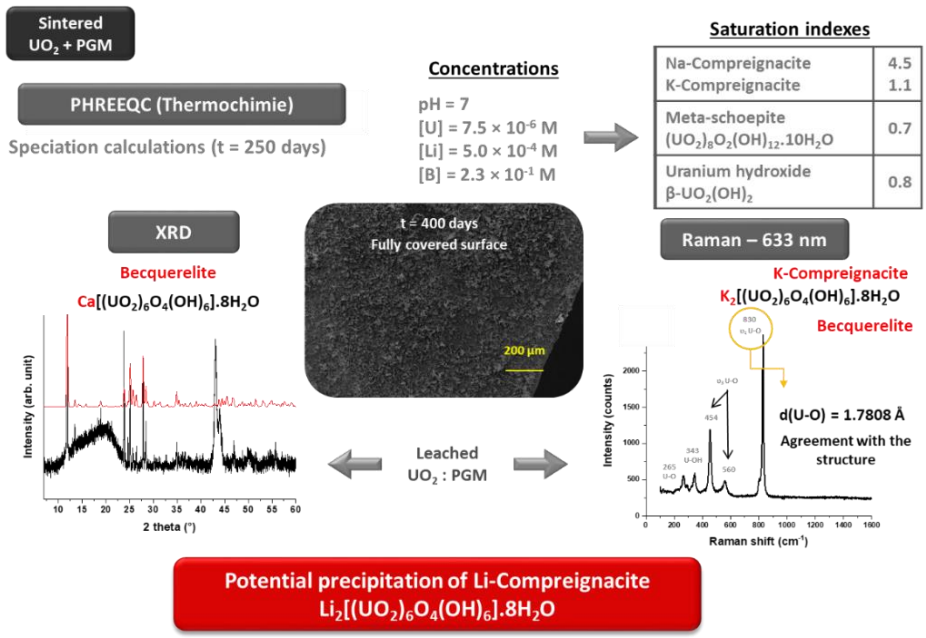

Figure 20 Characterization of the neoformed phase obtained during dissolution tests of UO_2:PGM obtained at 50 °C, at pH =7, in the presence of H_3BO_3 and LiOH (t > 400 days).

Since the leaching solution contains lithium cations instead of calcium and as the becquerelite structure looks like a multi-layered structure [78] in which the cations are present in the layers, one can suggest the formation of compreignacite (which falls in the same structure as becquerelite). The formation of this phase has been already reported for Na-compreignacite and K-compreignacite ($M_2[(UO_2)_6O_4(OH)_6].8H_2O$ (M = Na, K)). In these dissolution conditions, the formation of Li-compreignacite is thus expected. In order to confirm this point, Raman spectra were also recorded (Figure 20). All the bands associated to compreignacite were observed, especially than corresponding to the ν_3(U-O) vibration (830 cm^{-1}), characteristic of the uranyl group. From the correlation proposed by Bartlett *et al.* [79], the distance d('U-O) was evaluated to 1.7808 Å, which appears in good agreement with the value associated to the becquerelite structure.

Moreover, dissolution tests of UO_2:PGM performed at pH = 5 (Figure 21) revealed the formation of another neoformed phase, which fully covered the entire surface of the pellet for t > 550 days. The characterization of this phase by XRD suggested the formation of meta-shoepite $(UO_2)_8O_2(OH)_{12}.10H_2O$ or U hydroxide β-$UO_2(OH)_2$. The associated Raman spectrum obtained after dissolution confirmed this point with the existence of a strong doublet near to 860 cm^{-1}, characteristic of the uranyl group in the meta-shoepite structure. The crystal neoformed at the surface of the samples appeared bigger than that observed of Li-compreignacite.

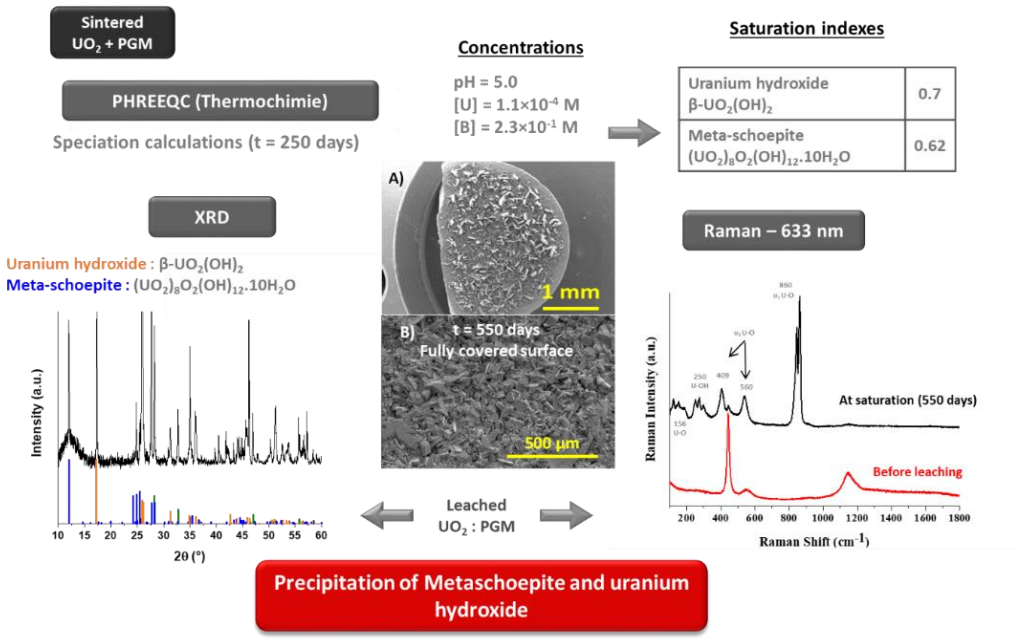

Figure 21 Characterization of the neoformed phase obtained during dissolution tests of UO_2:PGM obtained at 50 °C, at pH =5, in the presence of H_3BO_3 (t > 550 days).

For both systems, speciation calculations were performed taking into account the concentrations measured in the leachates. From this calculation, it clearly appears that both systems were oversaturation related to Compreignacite (saturation index of 4.5 considering the solubility constant of Na-Compreignacite, no data being available for Li-Compreignacite) on the one hand, and to meta-shoepite (saturation index of 0.6 to 0.7), on the other hand. These results confirm the existence of saturation conditions in the leaching solutions obtained.

3.3 Discussion and outcomes

As part of the experiments carried out in this work, several types of sintered materials representative of used fuels were prepared by wet chemistry route and then sintered at high temperature. The results showed that the lanthanide ions (Nd, Ce, La, Pr and Y) were incorporated quantitatively into the fluorite structure, leading to a slight decrease in the lattice parameter, in agreement with the average ionic radius of the incorporated lanthanide ions compared with that of uranium (IV) in the eight-fold coordination number. On the other hand, the platinum elements (Ru, Rh, Pd) and molybdenum were not incorporated into the structure. They formed metallic alloys inclusions that have been clearly revealed by X-EDS analysis. Using this method, dense samples with densification rates of between 89 and 97% of the calculated density were obtained. The developed surface areas, determined by image analysis (SESAM method) were between 2.10^{-2} and 10^{-1} $m^2 \cdot g^{-1}$. They were almost 100 times greater than the geometric surface area of the pellets (i.e. 3.10^{-4} $m^2 \cdot g^{-1}$).

All the prepared sintered samples (UO_2, $(U,Ln)O_2$, UO_2:PGM, UO_2:PGM+Mo and $(U,Ln)O_2$:PGM+Mo+Ln) were submitted to long-term dissolution tests in deionized water, in a solution containing boric acid (2500 ppm, *i.e.* $2.3 \cdot 10^{-4}$ mol L^{-1} H_3BO_3, pH = 5) and in a solution containing boric acid and lithin ($2.3 \cdot 10^{-4}$ mol L^{-1} H_3BO_3, LiOH, pH = 7). Two temperatures (50 °C and 70 °C) were

considered.

Dissolution tests performed on UO_2 and $(U,Ln)O_2$ at pH = 7 revealed the existence of a slope break when plotting the evolution of the normalised weight loss $N_L(U)$. The associated normalised dissolution rates decreased by a factor of 3 for UO_2 for dissolution times longer than 100 days. This break appeared earlier for $(U,Ln)O_2$ (*i.e.* for t > 60 days) and was stronger (decrease by a factor of 12 to 30), leading to very low normalised dissolution rates (typically in the range of $5\text{-}8\cdot10^{-6}$ $g\cdot m^{-2}\cdot d^{-1}$). This suggests a beneficial impact of Ln elements on the chemical durability of the ceramics for the three conditions examined. The associated U concentration at saturation reached $6.7\cdot10^{-7}$ $mol\cdot L^{-1}$. For UO_2, normalised dissolution rate was found to be slower by a factor of 5 at pH = 7 than at pH = 5. This difference was reduced for Ln doped UO_2 materials. These higher dissolution rates observed at the early beginning of the dissolution was surely due to less durable zones of the material (including hyper-stoichiometric domains, crystal defects potentially present in the grains boundaries -).

No slope break was observed until 250 days of dissolution time for UO_2:PGM ceramics. Above this dissolution time, a plateau was clearly observed suggesting the formation of neoformed phase. The beginning of this plateau corresponds of a relative dissolution mass of the material equal to 0.20 wt % and then to a U concentration at saturation of $7.5\cdot10^{-6}$ $mol\cdot L^{-1}$. The direct comparison of the results obtained for UO_2 and UO_2:PGM showed no effect of PGM elements when it dissolves at pH =7 and a factor of 4 to 5 at pH = 5. UO_2:PGM pellet dissolved 25 to 30 times more slowly at pH = 7 than at pH = 5 whatever the presence (or not) of boric acid in the leaching solution. Due to the catalytic properties of PGM elements, enhancing oxidation of U (IV) to U (VI) [69, 76, 77], a much higher concentration of U at saturation was obtained compared to that of $(U,Ln)O_2$ solid solutions. Moreover, dissolution rate of sintered samples of UO_2:PGM increases compared to pure UO_2, by a factor less than 1.5 at pH = 7 in the presence of boric acid, less than 4 at pH = 5 in the presence of boric acid, and by a factor of 7 in deionized water. Comparison of the results of dissolution of UO_2:PGM with that of UO_2:PGM+Mo in the three studied media did not reveal any significant impact of molybdenum. Additionally, the comparison of the results obtained at pH = 5 in the presence of boric acid and in deionized water confirmed that boric acid did not affect significantly the normalised dissolution rates of the ceramics. Finally, a direct comparison of the dissolution tests performed for UO_2:PGM+Mo and UO_2:PGM+Mo+Ln revealed that the normalised dissolution rates were reduced by about one decade for the three studied leaching solutions in the presence of Ln elements. This effect could result from the U speciation in the sintered materials, which is strongly affected by the presence of Ln elements.

Dissolution tests of $(U,Ln)O_2$ and UO_2:PGM sintered pellets, at pH = 7, revealed the formation of neoformed phases, that was suggested by the existence of a plateau when plotting the evolution of the normalised weight loss. This was confirmed with the help of operando monitoring by ESEM of the solid/solution interface. For $(U,Ln)O_2$ solid solutions (with 6 mol % Ln) leached at 50°C and pH = 7, it showed the formation of small nodules (less than a few tens of nanometres in size). Due to the too small size of these nodules, their identification remained impossible even after 450 days of dissolution. Some complementary attempts to characterize these neoformed phases are under progress.

Conversely, operando monitoring by ESEM during dissolution of UO_2:PGM samples at 50 °C and pH = 7 revealed the formation of platelets type crystals onto the surface of the leached material. These

crystals covered the entire surface of the sample after 550 days of dissolution. The characterisation of these crystals was performed with the help of XRD, ESEM and Raman spectroscopy. XRD analysis suggested the formation of Li-compreignacite $Li_2[(UO_2)_6O_4(OH)_6]\cdot 8H_2O$. All the bands associated to compreignacite were observed by Raman spectroscopy, especially that corresponding to the ν_3(U-O) vibration (830 cm^{-1}), characteristic of the uranyl group. From the correlation proposed by Bartlett *et al.* [79], the distance d(U-O) was evaluated to 1.7808 Å, which appeared in good agreement with the value associated to the becquerelite's family structure. Dissolution the samples at pH = 5 revealed the formation of meta-shoepite $(UO_2)_8O_2(OH)_{12}\cdot 10H_2O$ or U hydroxide β-$UO_2(OH)_2$. The associated Raman spectrum obtained after dissolution confirmed this point with the existence of a strong doublet near to 860 cm^{-1}, characteristic of the uranyl group in the meta-shoepite structure. The crystal neoformed at the surface of the samples appeared bigger than that observed for Li-compreignacite. Speciation calculations showed that both systems were oversaturation related to Compreignacite (saturation index of 4.5 considering the solubility constant of Na-Compreignacite, no data being available for Li-Compreignacite) on the one hand, and to meta-shoepite (saturation index of 0.6 to 0.7), on the other hand. These results confirmed the existence of saturation conditions in the leaching solutions obtained.

The dissolution tests are currently being extended to increase the quantity of neoformed phase for the several systems or to grow the crystals for others. Dissolution rates will be determined for longer dissolution times, while the neoformed phases will be further characterised. Finally, once they have been produced as pure phases, the solubility products of Li-compreignacite and meta-shoepite will be evaluated based on concentrations obtained under saturation conditions.

4. HZDR

4.1 Synthesis of SIMFUEL

In agreement with previous work [80], the targeted concentrations were 0.6 % wt for Mo, Zr and Ru, 0.3 % for Zr and Ba and 1 % wt for Nd. Several synthesis routes were studied to obtain a SIMFUEL microstructure as representative as possible of spent nuclear field (SNF). Here, we will present the two methods that gave the best results. On one hand, a solid-state route was employed in which UO_2 powder was mechanically mixed with commercials FPs powders. On the other hand, a liquid method, based on the coprecipitation of mixed oxalate, was used [81]. In both cases, the FP-produced powders were then sintered at 1600 °C using spark plasma sintering [81].

4.2 Characterization methods

XRD measurements were performed using a Rigaku Miniflex 600 in Bragg–Brentano geometry, with a ceramic copper source (40 kV, 15 mA) without monochromator (Kα1 = 1.5406 Å, Kα2 = 1.5444 Å), supplied with a Hy-Pix 400MF 2D HPAD detector. SEM images were acquired with a dual-beam focused ion beam ThermoFisher Scientific (ex FEI) Versa 3D SEM with field emission gun operated at 30 keV. More details about the employed characterization techniques can be found in this paper [82].

4.2.1 SP-XRD

Synchrotron powder X-ray diffraction data were recorded on the Rossendorf beamline using a Pilatus3X 2M detector (Dectris Ltd.), with a sensitive area of 253.7 × 288.8 mm^2 (width × height). The excitation energy was set to 17038 eV to avoid scattering background due to fluorescence above the U L_3 absorption edge at 17166 eV.

4.2.2 XAS: XANES and EXAFS

XANES and EXAFS data were recorded on the Rossendorf beamline [39] using a Si(111) double crystal-monochromator coupled with collimating and focusing Rh-coated mirrors, while the samples were held at 15K by a He-cooled cryostat. XAS data were collected in transmission mode using Ar/N_2 filled ionization chambers and in fluorescence mode with an electrically cooled (Cryo-Pulse 5 Plus) 18-element germanium detector (Ultra-LEGe, GUL0055, Mirion Technologies).

4.3 Results on the behaviour of SIMFUEL and UO_2 under dry interim storage conditions

4.3.1 Characterization of as-synthesized SIMFUEL compounds

4.3.1.1 Uranium matrix

SP-XRD have shown that for each compound only one FCC phase is present and is representative of the UO_2 matrix (Figure 22).

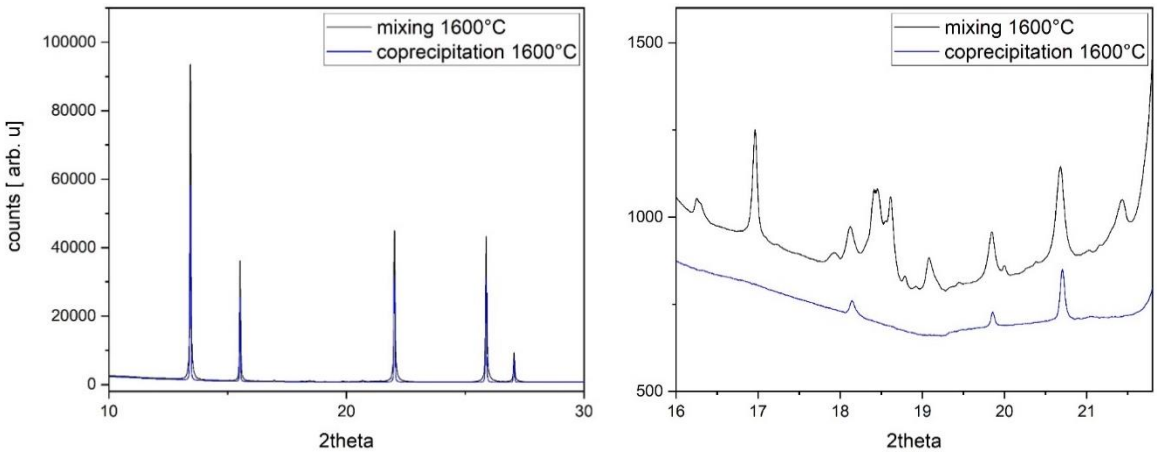

Figure 22 SP-XRD patterns of the as-synthesized SIMFUEL samples (right plot is zoom area of the left plot).

Additional non-FCC peaks have been observed but since they belong to the precipitates, they will be discussed in section 4.3.1.2. UL_{III} EXAFS confirms all the compounds are fluorite (Figure 23). In all samples, the first metallic distances are almost identical while changes have been detected in the first O shell, which is indicative of a slight modification of oxygen distribution within the anion sublattice.

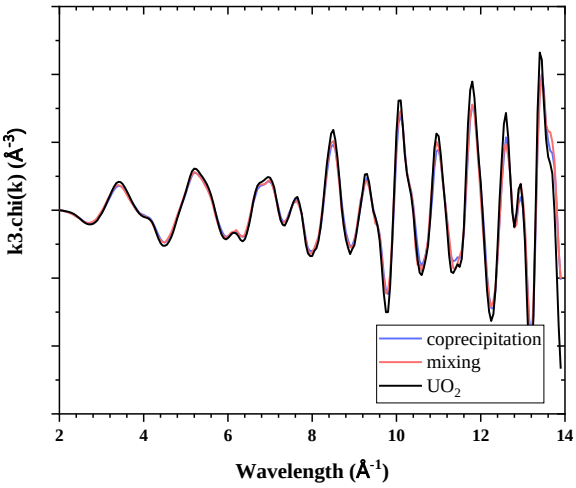

Figure 23 U L_3-edge $k^3.\chi(k)$ EXAFS signals of the as-synthesized SIMFUEL samples.

Figure 24 summarise the XANES results at the UL_{III} edge. First, we can observe that all sample are well aligned with the stoichiometric $UO_{2.00}$ reference, indicating that U remains predominantly U^{+IV}. By analogy with other FP doped system [83], one can assume the presence of U^{+V} to account for the incorporation of trivalent FP. However, this could not be observed here due to the high detection limit of conventional XANES. HERFD-XANES analysis was planned, but unfortunately not performed due to the global Covid-19 pandemic.

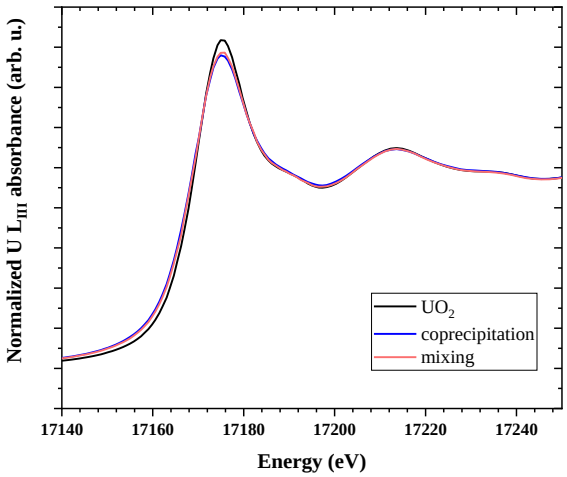

Figure 24 U L_3-XANES of the as-synthesized SIMFUEL samples.

4.3.1.2 Oxide and metallic precipitates

As for U, the valence state of Nd, Zr, Ru and Mo has been studied using XANES. Unfortunately, Barium could not be measured due to the lack of beamtime as a consequence of the Covid-19 pandemic. In agreement with the literature [84], one could assume though that Ba crystallises with Zr and Mo to form a perovskite-type phases typical of irradiated MOx fuel.

As expected, the Nd L_{III} XANES is compatible with the trivalent oxidation state and the eight-coordinated oxygen environment, indicating that Nd is completely accommodated within the UO_2 fluorite solid solution. Ru was found in a metallic state, which agrees with its expected behaviour to form metallic phases. According to Zr K XANES, Zr was found in both ZrO_2 and $BaZrO_3$ structures, which agrees with the results of SP-XRD. Mo was, however, found only in the solid-state as-prepared sample. Both metallic and oxide Mo-states were observed.

As briefly mentioned above, the samples were studied by SP-XRD as the higher photon energy allows the detection of the secondary phases, which are not observable with a laboratory diffractometer. The Figure 23 presents the SP-XRD patterns of both samples. As expected, a variety of different secondary phases can be observed. For the powder metallurgy synthesised samples, some of the XRD reflexes are attributable to metallic phases (mainly MoRu alloy) while others are representative of oxides phases like ZrO_2 and $BaZrO_3$. For the sample prepared by co-precipitation, similar oxide phases are observed. However, only metallic Ru phase was detected, which agrees with the absence of Mo observed in XANES.

4.3.2 Oxidation of SIMFUEL

Both afore mentioned sample have been oxidized in an oven under air at 300 ˚C during 1 week to simulate accidental scenarios during dry interim storage.

4.3.2.1 Uranium matrix

SP-XRD, XANES and EXAFS shows the oxidation of the uranium fluorite matrix. Indeed, as shown in Figure 25, the UL_{III} XANES spectra are clearly shifted toward higher energy. One can see that the sample prepared by a solid-state route looks like U_3O_8 while the wet route sample seems a bit less oxidized. This is actually in total agreement with SP-XRD, as the XRD patterns corresponds in the former case to a U_3O_8 structure and in the latter case to a mixture of both U_3O_7 and U_3O_8. This difference of oxidation behaviour needs further works to be totally understood but one can assume that it can be related to the difference of microstructure, grain size and Mo composition.

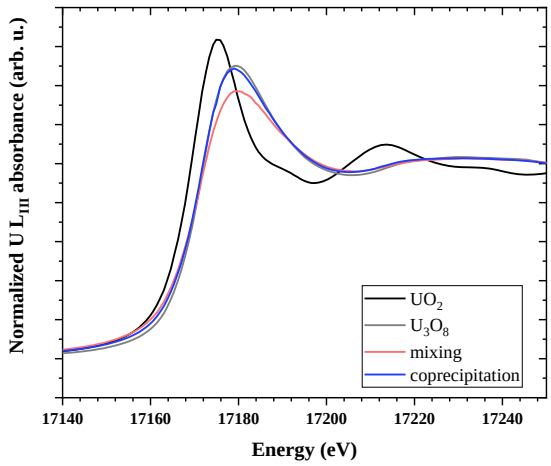

Figure 25: UL_3-XANES of oxidized SIMFUEL sample.

4.3.2.2 Secondary phases

SP-XRD (Figure 26) shows that both metallic and oxide phases are still present within both samples.

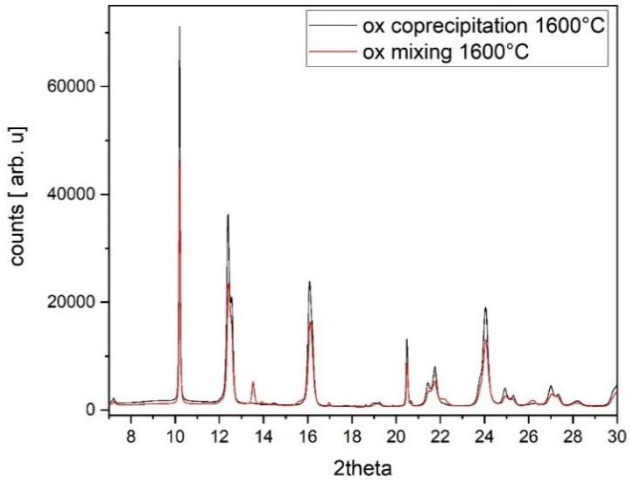

Figure 26: SP-XRD patterns of the oxidized SIMFUEL samples obtained by both solid-state route (ox mixing) and liquid method (ox co-precipitation).

According to XANES, Nd and Ru are not affected by the oxidative treatment, as they remain trivalent

and metallic, respectively. However, Zr K and Mo K XANES revealed oxidation of both Zr and Mo cations, which according to SP-XRD corresponds to higher contents of both ZrO_2 and $BaZrO_3$.

4.3.3 Effect of the grain size on the oxidation of UO_2

4.3.3.1 Sample preparation

The optimisation of the sample preparation in order to obtain dense (95% TD) UO_2 disks with final grain size close to the one of the HBS was already described in dedicated publications [82, 85]. Briefly, UO_2 nano-powders were produced by hydrothermal decomposition of U(IV) oxalate at 170 °C. The powders were sintered using Spark Plasma Sintering (SPS) with three different thermal treatments to obtain various grain sizes. A final annealing under Ar–H_2 (4% vol) at 600 °C was performed to reduce all the samples to the same $UO_{2.00}$ stoichiometry, without affecting their microstructures (the temperature of the annealing was lower than the maximum sintering temperatures in every SPS treatment). As seen in Figure 27, the average grain sizes of the investigated UO_2 samples are 3.08 ± 0.06 µm (micro), 478 ± 17 nm (sub-µ) and 163 ± 9 nm (nano).

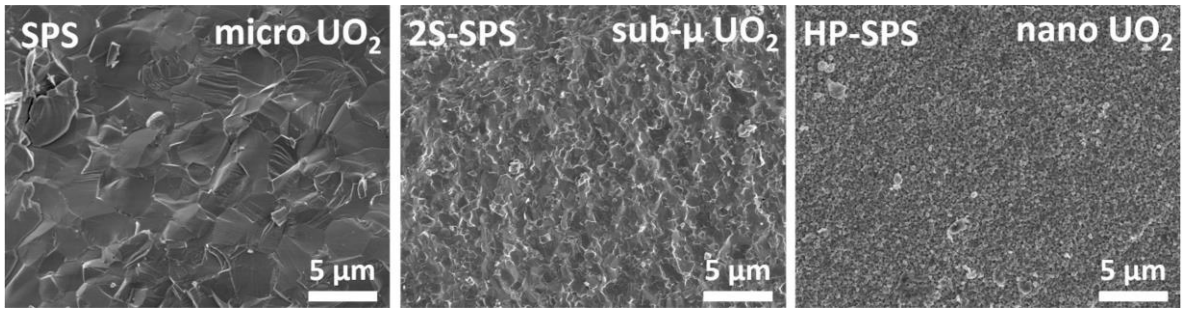

Figure 27 SEM SE images of the microstructures of the as-sintered materials. The grain sizes are 3.08 ± 0.06 µm for the micro UO_2 obtained by regular SPS (70 MPa, 10 min, 1600 °C), 478 ± 17 nm for the sub-µ UO_2 produced by 2S-SPS (70 MPa, 3 s at 650 °C, 100 min at 550 °C), and 163 ± 9 nm for the nano-UO_2 prepared by HP-SPS (500 MPa, 30 s, 660 °C).

4.3.3.2 Size-dependent oxidation behaviour

The as-sintered UO_2 materials with different grain sizes were then oxidised at 300 °C in air for 21 h to account for the various size distribution present within the SNF, and their structural evolution was monitored by HT-SRXRD [82]. The sampling frequency during the 21 h long oxidations allowed having a complete and comprehensive overview of the transformation ongoing in the samples. In HT-SRXRD, the build-up of the different compounds could be followed by the emergence or disappearance of peaks and shoulders over time or by their changes in shape and relative intensity (Figure 28). However, the coexistence of many phases and domains, each one developing interdependently, made it sometimes complicated to extract all the possible information.

Figure 28 show the evolution of the different phases during the oxidation of each samples. These volume fractions were calculated by Rietveld refinements using the crystallographic data found by Desgranges *et al*. [86]. As can be seen in Figure 28, in all three samples, the volumetric fraction of U_4O_9 remained constantly below 20 %. This can be understood by its prompt conversion to U_3O_7. After 10 min, this latter oxide constituted the largest volume fraction for all the samples. At this point, once U_3O_7 was the major phase, different oxidation behaviours were observed depending on the grain size.

In the micro sample, U_3O_8 was detected after 15 min, which corresponded to the maximum U_3O_7 volume fraction (ca. 60 %). Due to the large grain size, the complete conversion of the UO_2 in the bulk of the grains to U_3O_7 was significantly delayed with respect to the other samples (completed after about 10 h, instead of about 2.5 h as in the sub-µ and nano-grained samples). In the sub-µ UO_2 sample, the U_3O_7 volume fraction kept increasing up to 80 % (after about 30 min), and only then it started to be consumed by its transformation into U_3O_8. This oxidation then proceeded at the expenses of U_3O_7, while in turn, UO_2 was consumed and transformed to U_4O_9 and then U_3O_7. After about 11 h, no more U_4O_9 could be detected, and the sample was composed of 95 % of U_3O_8. For both the micro and the sub-µ samples, at the end of the experiment (21 h), U_3O_8 was the main phase, but a small share (below 3 %) of U_3O_7 was left. No U_3O_8 was detected in the nano-grained sample, where all the UO_2 was converted to U_4O_9 and U_3O_7 after 2.5 h, and U_4O_9 slowly disappeared throughout the rest of the oxidative treatment.

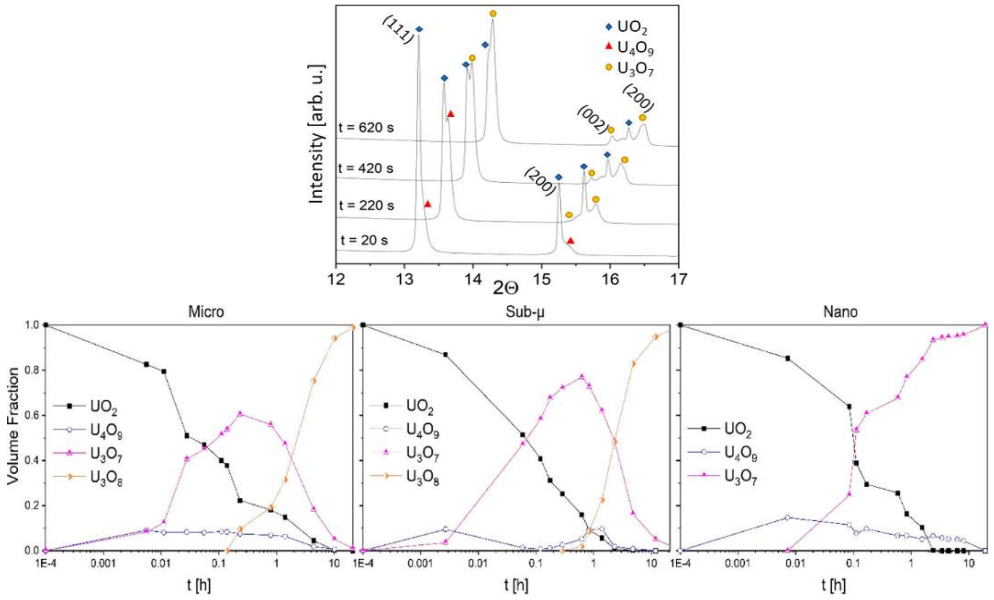

Figure 28 (Up) Evolution of the HT-XRD pattern of the micro-grained UO_2 sample in the first 620 s of the isothermal oxidative treatment. (Down) Evolution of the different phases in the three samples during the oxidative treatments (grouped by sample).

4.3.3.3 Nano-grains inhibit U_3O_8 formation

A comparison of the diffraction patterns of the initial and final states of the samples is shown in Figure 29, where the main U_3O_8 peaks are marked with a blue star. Clearly, the peaks of U_3O_8 could not be detected in the nano-grained sample. While the micro and sub-µ samples followed a similar behaviour, being almost fully converted to U_3O_8 after about 11 h of oxidative treatment, no U_3O_8 was detected in the nano-grained sample. This could have positive implications in the safety of SNF storage, as the formation of U_3O_8 involves a 36 % volume expansion, detrimental for the rod integrity, and is triggered by the cracking of the material. Such a finding is particularly interesting considering that the peripheral region of SNF is constituted of the HBS, whose grain size is in the order of magnitude of the nano-grained sample used in this work.

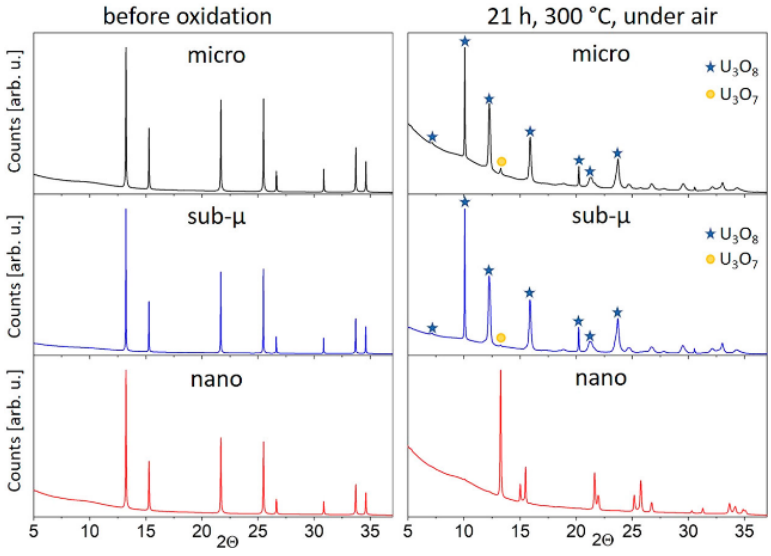

Figure 29 Comparison of the SR-XRD patterns for the three samples before and after the oxidation treatment. Contrary to the micro and sub-µ UO_2 samples, no U_3O_8 was detected in the nano-sized compounds after 21 h in air at 300 °C. The main diffraction reflexes of U_3O_8 are marked with a blue star.

4.3.3.4 Nano-grains oxidation beyond U_3O_7

Similar to what was reported in the literature for fine powders, oxidation proceeded to a certain extent beyond U_3O_7 [87, 88]. It was indeed found that, especially for extremely long thermogravimetric analyses (TGA) experiments, the sample oxidation did not stop with the formation of U_3O_7, but rather advanced orders of magnitude slower than for micrometric powders or sintered pellets (and possibly with a different weight gain curve shape). A similar mechanism could have taken place in the nano-grained sample analysed in this work, with the UO_3 phase remaining undetected in XRD, being amorphous, and instead being revealed by the XANES. The time frame of this experiment does not allow to draw conclusions on whether the O/M ratio of the sample reaches a plateau or if it would increase with extremely slow kinetics (such as for fine powders). It is worth noting that the kinetics of nucleation and growth of amorphous UO_3 could differ between the boundary of a nano-grain embedded in a dense material and the free surface of a loose powder nano-particle.

4.4 Discussion and outcomes

A comprehensive understanding of the spent fuel behaviour in various conditions (*e.g.* in-pile nominal conditions, accidental scenarios, final geological disposal, etc.) is mandatory for a nuclear installation handling SF, to obtain an operating license. However, studying irradiated fuel is very challenging due to its radiotoxicity and its chemical complexity as it contains dozens of fission products, which interaction changes its behaviour and properties. In order to overcome these issues, model U-based materials called SIMFUEL have been developed in the last decades. In this work, Mo, Ru, Ba, Zr and Nd were used as they belong to three different families of FP (those that are partially or completely soluble in the fuel matrix (Zr and Nd), those which form oxide precipitates (Ba and Zr) and those that form metallic precipitates (Mo and Ru)). In this context, this contribution has worked on three main objectives:

- New synthesis methods have been designed and investigated. The as-fabricated compounds have been characterised by several multi-scale techniques to study the secondary phases and both actinide and FP speciation.

- The as-synthesised materials have been subjected to oxidative environment to study the effect of the oxidation as this phenomenon could be detrimental for the fuel integrity in case of accidental scenario during its storage.

- Considering that the SNF presents a heterogeneous grain size distribution along its radius, the effect of the grain size on the oxidation behaviour has been studied.

The samples were synthesised and characterised by XRD and SEM at the European Commission Joint Research Centre in Karlsruhe. All synchrotron based-techniques (SP-XRD, XANES, EXAFS) were performed at the HZDR-operated Rossendorf beamline [39] of the European Synchrotron Research Facility.

5. CEMHTI/CNRS

5.1 Samples

Three sets of samples have been prepared in ICSM/CNRS-CEA Marcoule using a process that ensures homogeneous cation distribution (U and Ln) in the final compound (see Table IX). All the samples are doped with only one single lanthanide either La, Nd or Gd.

Table IX Sets of Ln doped UO_2: the synthesis of powder, sintering conditions and heat treatment of the disks (*nominal concentration specified by the manufacturer).

Set	Delivery	Dopants		Powder synthesis	Sintering	Annealing CEMHTI
		type	mol %*			
Set 1 MLA	March 2019	La	15	Oxalate [89] $U_{1-x}La_x(C_2O_4)_2{\cdot}2H_2O$ + conversion 700 °C/4h/Ar-H_2(4%)	1600 °C/ 5h /Ar-H_2 (4%)	1600 °C/ 2h / Ar-H_2 (10%) + 1500 °C/ 5h / Ar/H_2 (10%)
Set 2 JL	Oct. 2020	La	6	Oxalate [89] $U_{1-x}La_x(C_2O_4)_2{\cdot}2H_2O$ + conversion 700 °C/4h/Ar-H_2(4%)	1600 °C/ 4h//Ar-H_2 (4%)	1500 °C/ 5h / Ar-H_2 (10%)
Set 3 RS	April 2021	La, Nd, Gd	6, 15, 25 6, 15, 25 6, 15, 25	Hydroxide [90] $U_{1-x}Ln_x(OH)_4$ + drying 700 °C/4h/Ar-H_2(4%)	1600 °C/4h/Ar-H_2(4%) or 1600 °C/ 4h/ vacuum	1500 °C/ 5h / Ar-H_2 (10%)

The two first batches (sets 1 and 2) of lanthanum doped UO_2 samples were prepared by sintering powders obtained by oxalic co-precipitation [89], drying of the oxalate precursor at 90 °C and conversion to oxides by heat treatment at 700 °C for 4 h in an Ar/H_2(4%) reducing atmosphere.

This $U_{1-y}La_y O_{2\pm x}$ powder was pressed (uniaxial pressing at 500 MPa) to obtain green pellets with a relative density close to 50% TD. These pellets were then sintered by means of a 5-hour heat treatment at 1600 °C in a reducing Ar-H_2 (4%) atmosphere to obtain pellets with a density greater than 90% TD. These dense pellets were polished to remove any defects induced by the previous steps.

For the third batch, the Ln doped oxide powder was prepared using a new synthesis route [68, 90] allowing the production of hydroxides ($(U_{1-y}Ln_y)O_2 \cdot nH_2O$) precursors. All samples were polished in ICSM. Some Ln doped UO_2 samples were then annealed at CEMHTI for 2-5 hours at 1500-1600 °C under Ar-H_2 (10%).

5.2 Characterisation techniques

Various techniques are used in this study to characterise the microstructure and chemical composition of the samples: SEM/EDX, Raman, AFM. Positron annihilation spectroscopy (PAS) is used to characterise the point defects and nuclear reaction analysis (NRA) to measure the He release.

The SEM/EDX characterisations were performed using the JEOL - IT800SHL microscope at the MACLE Platform in Orléans (France). The majority of observations were performed at 20 kV. Secondary and backscattered electron images were acquired in order to characterize the microstructure. The chemical mapping is carried out with an EDS spectrometer equipped with an Ultim Max 100mm^2 SSD

detector.

Raman spectra were measured in two modes: (1) by focusing the laser beam in the centre of larger grains; and (2) using mapping on a surface sufficiently large to analyse several grains. An InVia Qontor instrument from Renishaw was used for these analyses. Spectra for individual map pixels were acquired in the streamline mode using a 633 nm laser and an 1800 line/mm grating centered at 950 cm^{-1}, such that each spectrum spanning from 327 to 1510 cm^{-1} was integrated for 90 seconds. The map data were recorded in Wire 5.3 software from Renishaw, which was also used to remove cosmic rays and then fit model spectra and visualize data. The model spectra contained four peaks: T_{2g}, which is the only Raman-active vibrational mode of perfect UO_2, and defect-related U1, U2 and U3. For the T_{2g} peak the fit parameters included the position, intensity and width, while the U1, U2 and U3 peaks were fixed at 525, 570 and 635 cm^{-1}, so that only their intensity and width were fitted.

5.2.1 Introduction of helium by ^{3}He implantation

^{3}He implantation is used to introduce Helium and to create damage (essentially point defects) in UO_2. The UO_2 disks have been implanted at room temperature (RT) with 1 MeV ^{3}He ions using the 3 MV Pelletron accelerator at CEMHTI Orléans (Figure 30.a). The implantation is carried out by focusing the beam (1×1 mm^2) and by sweeping it over the disk surface to ensure a homogeneous dose. For each NRA campaign all the disks were implanted during the same run, at a nominal fluency of $1 \cdot 10^{16}$ of $^3He^+ \cdot cm^{-2}$. The ^{3}He and damage (atomic displacements (dpa)) depth profiles were calculated using SRIM simulation code [91] in the so-called KP option (quick calculation with Kinchin Pease formalism). The displacement energy thresholds for oxygen and U atoms were set to 20 and 40 eV respectively [92]. The ^{3}He ions penetrate in UO_2 up to 2 µm (called the range). The He concentration is very low in the first 1 µm and increases up to a maximum value of 0.35 at % at 2 µm depth. The damage is roughly flat at an average value of 0.014 dpa in a region down to around 1µm in depth, corresponding to the area probed by the slow positrons (see Figure 30.**Erreur ! Source du renvoi introuvable.**b).

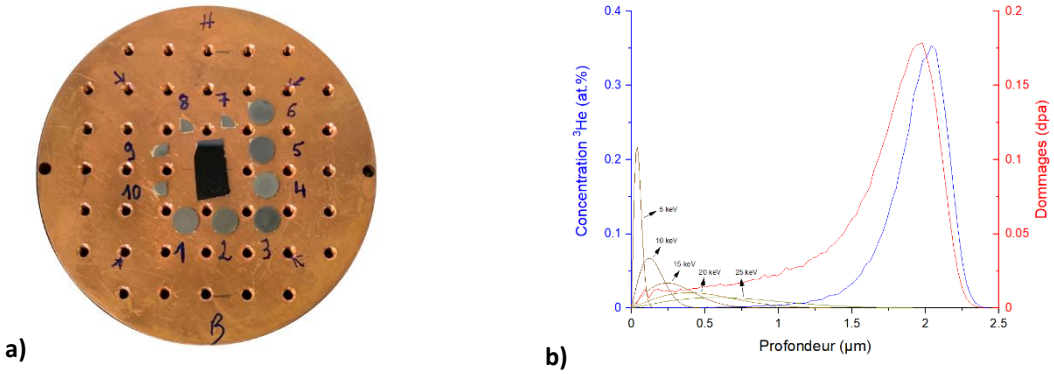

Figure 30 a) sample arrangement on the implantation sample holder for the first NRA campaign; b) implantation profile of mono-kinetic positrons and of ^{3}He atoms and damage profiles in UO_2 with a density of 10.76 g·cm^{-3}

5.2.2 Positron Annihilation Spectroscopy (PAS)

Positron annihilation spectroscopy is based on both fundamental properties of positron in solids: (1) it annihilates with electron leading to the emission of gamma rays at the energy of around 511 keV ; (2) it is trapped in vacancy defects where it annihilates allowing characterisation of vacancy

defects [93]. In this study, the samples were characterised by using a Slow Positron Beam coupled to a Doppler Broadening spectrometer (SPB-DB) available at the CEMHTI laboratory. A comprehensive description of the experimental setup and the basics of this powerful method are described in [94]. A mono-energetic positron mm beam was generated from a ^{22}Na source. The energy of the beam was varied in the range of 0.5 to 25 keV. The spectrum of the γ-ray annihilation photons (centred at 511 keV) is recorded using a high-resolution gamma spectrometer equipped with a germanium detector (1.24 keV resolution at 514 keV). This Doppler broadened spectrum is characterised by two line-shape parameters: *S* and *W*. *S*, defined as the ratio of counts in the central region of the spectrum to the total counts, represents the fraction of positron-electron pairs annihilated with low momentum and is related mostly to annihilations with valence electrons. *W*, the ratio of counts in the wing regions of the spectrum to the total counts, represents the fraction of positron-electron pairs annihilated with high momentum and hence is more specifically related to the annihilations of positrons with core electrons. For our experiments, the momentum ranges for the calculation of *S* and *W* correspond to ranges of energies of photons of [510.28–511.72 keV] for *S*, and [504.27–508.29 keV] and [513.71–517.73 keV] for *W*.

Each material exhibits specific S_L and W_L values, as a signature of the momentum distribution of electrons in the perfect lattice – *i.e.* without vacancy defects -. When positrons are trapped at vacancies, the annihilation with core electrons decreases and the positron-electron momentum distribution or annihilation line narrows, resulting in an increase of *S* and decrease of *W*. Each type of vacancy defects *j* is characterised by some specific values S_j and W_j. Generally, because *S* and *W* are also sensitive to the electronic environment of the positron when it annihilates, these parameters could detect the chemical decoration of vacancy defects [95].

For this study, *S(E)* and *W(E)* were recorded as functions of positron energy *E (*from 0.5 to 25 keV). Note that the FWHM of the implanted positron implanted profile increases with the energy, to reach ≈ 620 nm at 25 keV. At this energy, positrons probe up to ≈ 1400 nm depth below the UO_2 surface (see Figure 30.**Erreur ! Source du renvoi introuvable.**b). The *S* value measured at energy *E* depends on the defect distribution and diffusion properties of the positrons in the sample.

UO_2 samples were studied at room temperature in a previous study [94]. The *S(E)* and *W(E)* in UO_2 reference sample show plateau values S_{ref}=0.371±0.002, W_{ref}=0.079±0.001 associated to annihilation at non-vacancy defects [94]. These non-vacancy defects were predicted to be negative ions (oxygen interstitials O_i^{2-} or valence II and III impurities) that could be dissolved in UO_2 [94].

For He 1 MeV irradiated UO_2 [96], previous SPB-DB results plotted in *S(W)* curves showed experimental points aligned on the same D1 line with different position depending on the damage from the S_{ref}, W_{ref} point for no damage to the point with a maximum S_{max} value and minimum W_{min} obtained for a mean damage dose around 0.014 dpa in the positron probed region (0-1100 nm) for the ^3He fluency of $1{\cdot}10^{16}$ cm^{-2} [97]. S_{max} and W_{min} do not change when He fluency increases up to $1{\cdot}10^{17}$ cm^{-2} or damage dose up to 0.14. It is called He saturation point in the following and the associated annihilation characteristics are S_{HeSat} W_{HeSat} (S_{HeSat}=0.398±0.002, W_{HeSat}=0.069±0.001*)*. All the experimental points on this line D1 have been associated to positron annihilations as trapped in U vacancy related complexes by comparison with irradiation performed with electrons with sufficiently high energy to allow

displacements in the U sublattice [94, 98]. Up to now, no oxygen related vacancy defects could be detected probably due to their positive charge state.

5.2.3 Nuclear reaction analysis (NRA)

The He release was measured as a function of temperature in ^{3}He implanted samples (UO_2 and $(U,Ln)O_x$) using NRA and the $^3He(^2H, ^1H)\alpha$ nuclear reaction. The experiments were realised in DIADDHEM set-up installed on one beam line of the Pelletron accelerator in CEMHTI schematised in Figure 31. The set-up and the technique is described in the reference [97]. The incident ^{2}H ions energy was fixed at 900 keV allowing measuring the He amount in the first 3 µm depth in UO_2. The protons generated by nuclear reaction on ^{3}He are counted using a detector. For each experiment, standard samples implanted with well-known amount of ^{3}He are measured and used to calibrate the proton signal. These measurements were performed after ex situ annealing of ^{3}He implanted samples during 1 to 6 hours in Ar-H_2 (10%) atmosphere in CEMHTI at different temperatures, from 300 (573 K) to 1100 °C (1373 K).

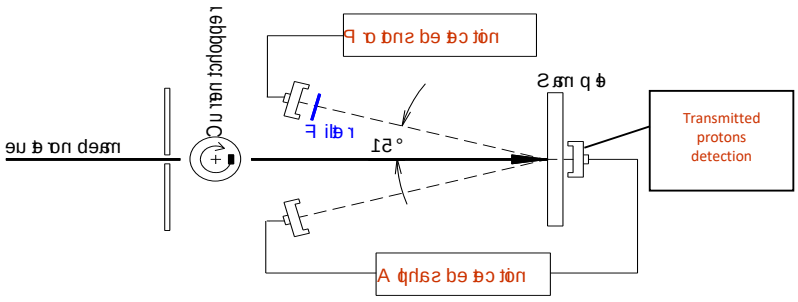

Figure 31 Schematic view of the DIADDHEM set-up used to measure the ^{3}He content in UO_2.

5.3 Results on the Helium release in UO_2 under interim storage conditions

In the following, the main results obtained in this study are reported. It has to be underlined that our studies are not finished due to COVID-19 pandemic. Our first results are described in the three following parts dedicated to:

1) the PAS characterisations.

2) the microstructure (grain size, roughness, crystallinity) and chemical composition characterisation of the samples that we carried the last months to try to understand the He release data.

3) the He release.

5.3.1 PAS characterizations of Ln doped uranium oxides

The Ln doped UO_2 from the three sets were characterized using PAS in as-received state after

annealing in various conditions and after He implantation.

5.3.1.1 As-received state

In the Figure 32.a, we show the results (*S(E)* and *W(E)* and *S(W) curves)* obtained in the ten as-received La (6%) doped UO_2 of the set 2 (Table IX). For all the samples, the S and W values are above the ones of UO_2 reference indicating the detection of vacancy defects. S and W evolve with positron energy suggesting that the depth defect distribution is not homogeneous. The *S(E)* and *W(E)* curves can be associated with three different groups: G1 with the highest *S* and lowest *W* values, G2 the median *S* and *W* values and G3 with the lowest *S* and highest *W* values. It indicates that the defects concentration is not the same in all the samples of the same set.

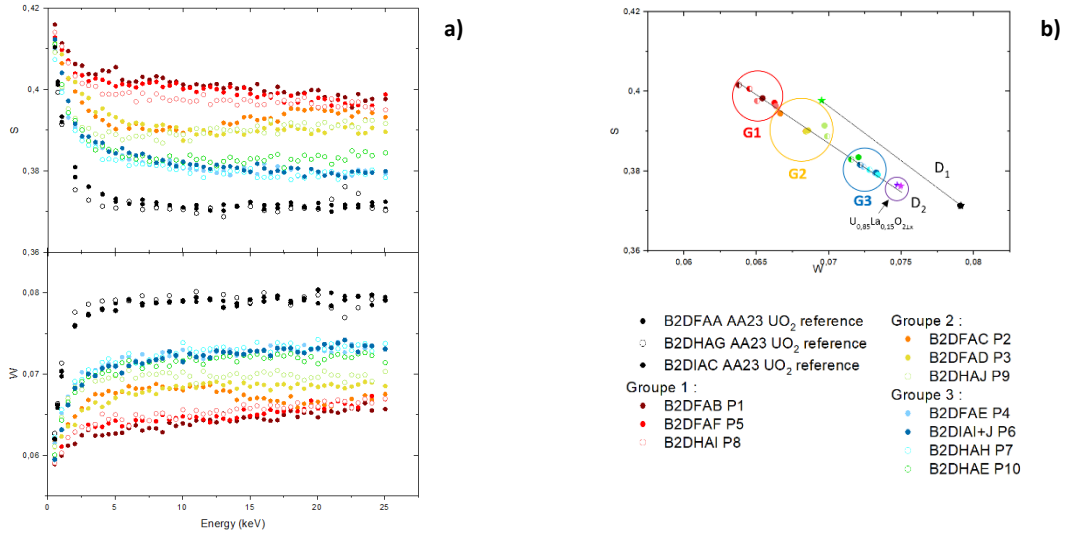

Figure 32 a) Low momentum fraction S and High momentum fraction W as a function of probing positron's energy; b) S as a function of W measured in the ten as-received La (6%) doped UO_2 of the set 2 compared to UO_2 reference samples and with the three La (15%) doped UO_2 annealed at 1600 °C/2h/Ar-H_2 (10%) of the set 1 . The half-full symbols correspond to the average of S and W in the 8-12 keV energy range and the full ones to the 18-25 keV range. The green star is the S_{HeSat} W_{HeSat} point and the D1 line is characteristic of annihilations at Vu related complexes.

In the Figure 32.a, we can distinguish two regions to be analysed: (1) a near-surface region corresponding to the 8-12 keV energy range (up to around 500 nm deep) and, (2) a deeper region (called 'bulk' around 1600 nm deep) representing the volume of the sample for an energy range of 18-25 keV. Interestingly the *S(E)* and *W(E)* curves of sample P9 follow the trend of group G2 in the low-energy range (from 0.5 to 12 keV) and then follow the trend of group G3. In the Figure 32.b, the average values in both regions are reported in a *S(W)* plot. They are compared to the S_{HeSat} W_{HeSat} green point and to the D1 line characteristic of annihilations at Vu related complexes (see section 5.2.2).

The SW points relating to samples doped with 6% La are more or less aligned on line D2, indicating that they contain the same defects whose concentration varies from the lowest for G3 to the highest for G1. It is interesting to note that the annealed (1600 °C/2h/Ar-H_2 (10%)) 15% La doped samples of set 1 are also aligned on the same D2 line and show a lower concentration of defects than the G3 group of as-received 6% La doped samples.

All the as-received samples from set 3 were measured by SPB-DB. As in set 2, *S* and *W* evolve with positron energy suggesting that the depth defect distribution is not homogeneous. In the Figure 33, the *SW* points corresponding to the average *S* and *W* in the 18-25 keV energy range are shown as representative of annihilation characteristics at a depth of around 1µm. Positrons detect defects in all set 3 samples whatever the Ln and its concentration. The defect distribution is sample-dependent.

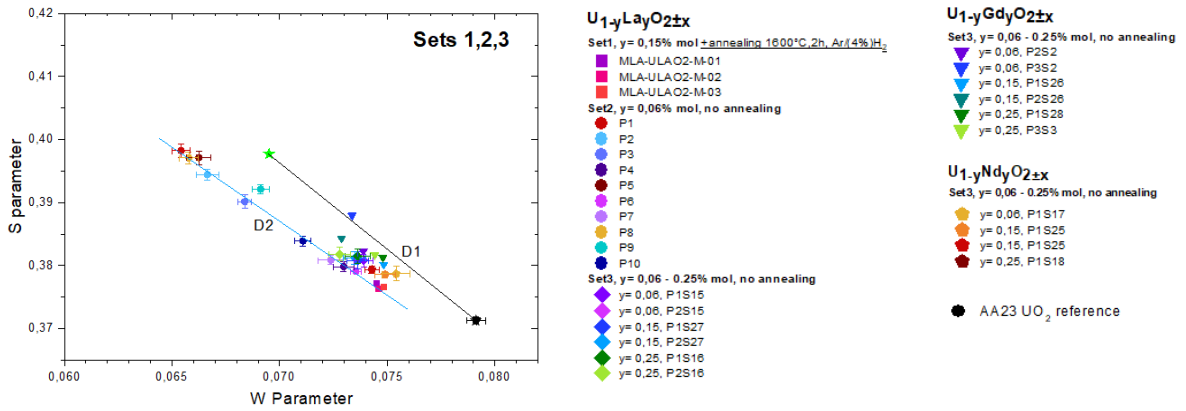

Figure 33 S as a function of W measured in the Ln doped UO_2 of the 3 sets in as-received state for the set 2 (La (6 mol %)) and Set 3 (La, Nd and Gd, 6-25 mol %) and after annealing at 1600 °C/2h/Ar-H_2 (10%) for the set 1 compared to UO_2 reference samples. The symbols correspond to the average of S and W in the 18-25 keV energy range. The green star is the S_{HeSat} W_{HeSat} point and the D1 line is characteristic of annihilations at Vu related complexes.

5.3.1.2 After annealing 1500 °C/5h/Ar-H_2 (10%) with an unintentional H_2O leakage

Some La-doped UO_2 from sets 1 and 2 were annealed at high temperature. After a first annealing 1500 °C/5h/Ar-H_2 (10%) with unintentional H_2O leakage from the cooling circuit, the annihilation characteristics evolved depending on the La concentration (see Figure 34).

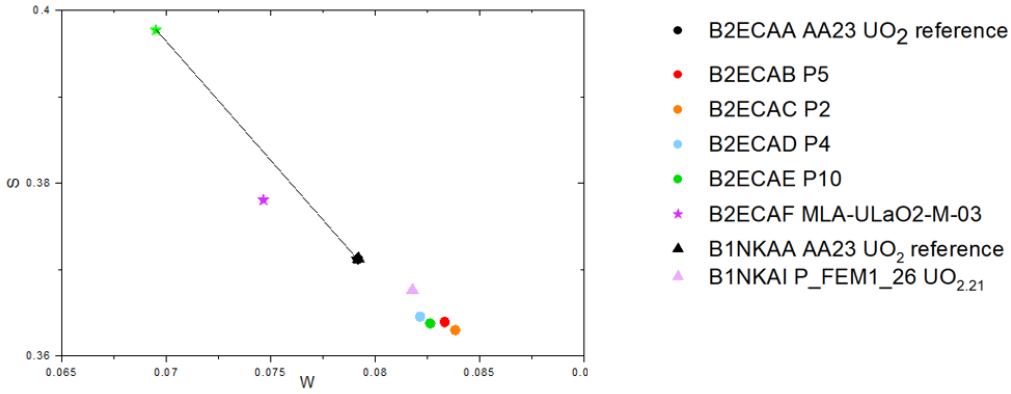

Figure 34 S as a function of W measured in the La 6 and 15 mol % doped UO_2 of the Set 1 and 2 after annealing at 1500 °C/5h/Ar-H_2 (10%) with unintentional H_2O leakage compared to UO_2 reference samples. The symbols correspond to the average of S and W in the 18-25 keV energy range. The green star is the S_{HeSat} W_{HeSat} point and the D1 line is characteristic of annihilations at Vu related complexes. The pink triangle correspond to the SW values recorded for an intentionally over-oxidized $UO_{2.21}$ sample [99].

For samples with 6% La (set 2) the values measured at depth (in the 10-25 keV energy range, *i.e.* deeper than 1µm) decrease strongly for *S* and increase for *W*. They become lower and higher than the *S* and *W* values for UO_2 reference respectively and close to the *SW* values recorded for an intentionally over-

oxidized $UO_{2.21}$ sample [99]. This change can be attributed to the oxidation of the 6% La doped samples as it was also observed in Raman spectroscopy (see Figure 40a). Interestingly, the evolution of the 15% La doped sample is not similar to that of the 6% La doped ones: *S* has increased and *W* has decreased compared to their values before this atypical annealing.

5.3.1.3 After annealing at 1500 °C/5h/Ar-H_2 (10%)

After repairing the furnace, the same samples were annealed at 1500 °C/5h/Ar-H_2 (10%) and characterized again. The *SW* points corresponding to the average *S* and *W* in the 18-25 keV energy range, representative of annihilation characteristics at a depth of around 1µm are shown in Figure 35.

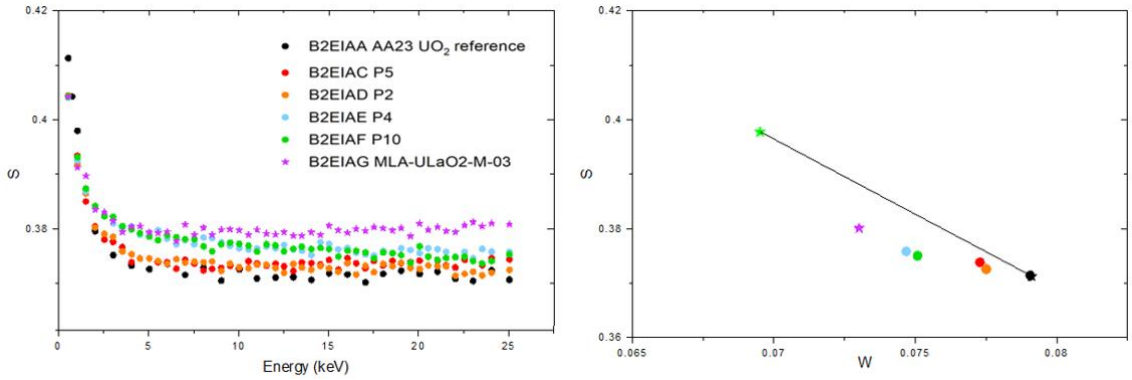

Figure 35 a) Low momentum fraction S as a function of probing positron's energy; b) S as a function of W measured in the La (6% and 15 mol %) doped UO_2 of the set 1 and 2 after the second annealing at 1500 °C/5h/Ar-H_2 (10%) compared to UO_2 reference samples. The symbols correspond to the average of S and W in the 18-25 keV energy range. The green star is the S_{HeSat} W_{HeSat} point and the D1 line is characteristic of annihilations at Vu related complexes.

After this further annealing, *S* increased and *W* decreased compared to the values measured previously. They are closer to the UO_2 reference values without reaching them, indicating that the O/M ratio has returned to a value close to 2. They are more homogeneous as a function of depth. However, defect distribution is sample-dependent. *SW* values are very close for P4 and P10 from the same group G3. Very similar *SW* values are also obtained for P2 and P5, which are from the groups G1 and G2 respectively. It should be noticed that the grain sizes of the samples from these two groups G1 and G2 are similar (Figure 38). We will see later that these two groups can be combined. Furthermore, the *SW* values of these two pairs are different showing in particular a lower *W* value for samples P4, P10 than for samples P2, P5.

5.3.1.4 After implantation with 1 MeV ^{3}He

Two implantation campaigns were carried out in the same conditions, *i.e.* with 1 MeV ^{3}He ions at RT and the fluency of $1 \cdot 10^{16}$ cm^{-2}. For the first He release study (campaign 1), different La doped UO_2 from sets 1 and 2 were chosen (see Table X). They are from the various groups (G1, G2, G3) in as-received state (P8) or annealed at 1500 °C/5h/Ar-H_2 (10%).

Table X List of samples chosen for the first He release experiment campaign. (*) the concentration of dopant measured in samples from the same group using SEM/EDX is given in brackets (see section 5.3.2.2).

Implantation campaign	Sample	Set	Ln doping		Group	Mean grain size (µm)	Density ($g.cm^{-3}$)	Annealing 1500 °C/Ar-H_2(10%) (hours)
			type	Nominal concentration (mol %) *				
Campaign 1	P5	2	La	6 (1)	1	5.99±0.5	10.0±0.1	5
	P8	2	La	6 (1)	1	5.28±0.5	10.0±0.1	0
	P2	2	La	6 (1)	2 (à1)	6.59±0.5	10.0±0.1	5
	P4	2	La	6 (5)	3	3.68±0.5	9.8±0.1	5
	P7 (4 parts)	2	La	6 (5)	3	2.81±0.3	>9.20	5
	P10	2	La	6 (5)	3	3.24±0.3	9.8±0.1	5
	MLA-M03	1	La	15 (13)	-	1.08±0.1	8.9±0.1	5

As shown in section 5.2.1, a damage dose of 0.014 dpa was calculated in the first µm under the surface, *i.e.* the region probed by slow positrons.

a) In as-implanted samples

As expected from the results obtained in UO_2, *S* increases and *W* decreases due to the creation of vacancy defects even in the not annealed P8 sample. The SW points are no longer aligned on line D2, indicating that the nature of the defects induced by implantation is different from that of the defects detected in as-received samples. The SW values depend on the sample (see Figure 36) indicating different defect distribution. The defect distribution is the same for P2 and P5 from 2 different groups (G1 and G2 - which will be assimilated to G1 in the following -) prepared in the same conditions and is close to the one detected in UO_2. For the P4 and P10 from the same group G3 and prepared in the same conditions the annihilation characteristics are very close, showing a larger *S* and lower *W* compared to P2, P5 samples.

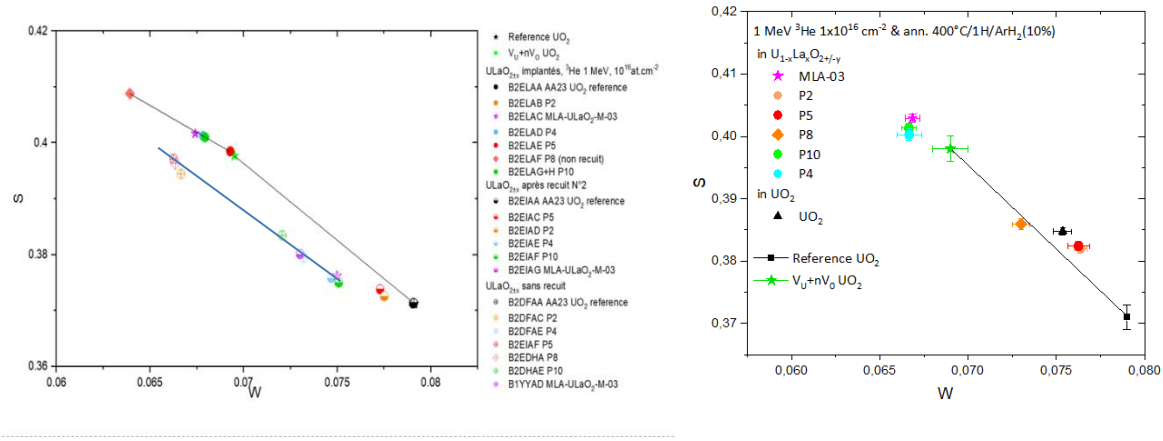

a) b)

Figure 36 S as a function of W measured in the La 6 and 15 mol % doped UO_2 of the Set 1 and 2 a) after implantation with 1MeV ^{3}He at $1{\cdot}10^{16}$ cm^{-2} (full circle) compared with the as-received state (crossed open circle) and the as-annealed state (after the second annealing at 1500 °C/5h/Ar-H_2 (10%), half-full circles) and to UO_2 reference samples; b) after implantation and annealing at 400°C/1h/Ar-H_2 (10%). The symbols correspond to the average of S and W in the 18-25 keV energy range. The green star is the S_{HeSat} W_{HeSat} point and the D1 line is characteristic of annihilations at Vu related complexes.

b) After implantation and annealing at 400 °C.

PAS measurements were performed in the samples implanted and annealed at 400 °C before NRA measurements. We observed two different behaviours (Figure 36b). In P2, P5 and P8 samples show strong changes in *S* and *W*. *S* decreases and *W* increases tending towards the UO_2 reference values, indicating the recombination of a large fraction of the implantation induced defects. In contrast for P4, P10 (La 6 mol %) and MLA-03 (La 15mol %) the changes are negligible at 1 µm depth indicating that the implantation induced defects are still present. It has to be underlined that for implantation of He in the same conditions we observed a clear decrease of the vacancy defects concentration in UO_2 after annealing at 400 °C/1h/Ar-H_2 (10%) [100].

We will see later (see section 5.3.2.2) that the concentration of La is not the same in all the P samples from set 2. It is close to 1mol % in samples P1 and P3 from the P5 and P2 group (G1) and about 5mol % for the samples P6 and P9 of the same group (G3) as P4 and P10. It is too early to conclude that the difference of behaviours can be attributed to the concentration of La in the samples.

To summarise, these first PAS investigations show that the Ln doped UO_2 studied here are not similar in the as-received state and present various unknown vacancy defect distribution. After annealing at high temperature (1500 °C/5h/Ar-H_2 (10%)) the concentration of defects decreases. After He implantation only U vacancy defects are detected in some samples (P2, P5) whereas other defects are also detected in P4 and P10. Annihilation at these U vacancy defects decreases strongly in P2 and P5, whereas no change is observed in P4 and P10, after annealing at 400 °C. The origin of these variable behaviours is not yet known, further investigations are required, in particular, a more detailed and systematic characterisation of the sample's microstructure and chemical composition which we have recently undertaken as part of this project.

5.3.2 Microstructure and chemical composition

The general aspect of the samples is very variable. Some of them are homogeneous while others are heterogeneous and show cracks, various distribution of grain size, chemical enrichments.

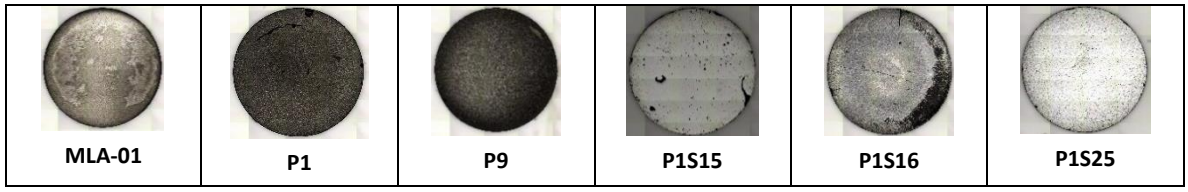

Figure 37 Some examples of the general aspects of the Ln doped UO_2.

The roughness was checked using AFM in some samples. It is very different from one sample to another. The Root Mean Square (RMS in 20 µmx20 µm squares) ranges from 0.013 µm for P2S2 or 0.06 µm for P1S16, the best-polished samples characterized. For most of the samples, roughness is not homogeneous. RMS varies from 0.12 µm to a maximum value at 0.23 µm in some places where grains are missing for P1, P6 and P9.

5.3.2.1 Grain size distribution in the La doped uranium oxides from sets 1 and 2.

The grain size was measured in the La doped UO_2. They have been extracted from analysis using ImageJ software of optical images for set 2. For set 1, the grains are too small and SEM had to be used. The images were recorded in a zone considered as representative of the sample, most of the time, in the centre of the disk. The grain size distributions are given in Figure 38. Three grain size distributions can be distinguished. The smaller grains are found in the MLA 15% La doped samples from set 1 with a mean value of 1 µm. In set 2, the four samples from the group G3 and P9 from the group G2 have a mean grain size of around 3 µm, while for the other samples, *i.e.* the three samples from group G3 and two from group G2 it increases up to 6 µm.

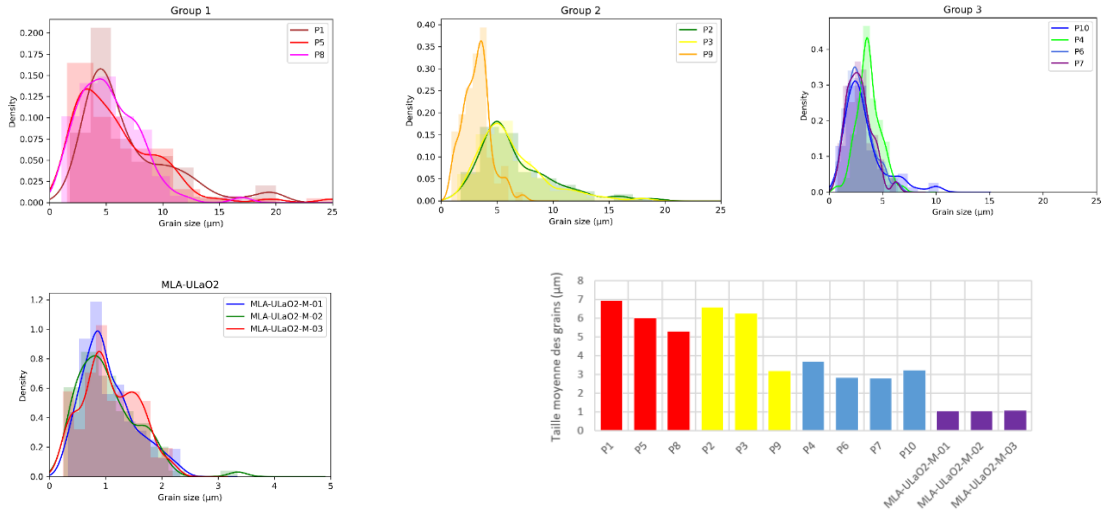

Figure 38 Grain size distribution and mean size in the La doped UO_2 of the set1 and 2.

It can be observed that the sample P9 can be associated to the group 3 as far as the size of grain is

concerned. It confirms that this sample show some bulk annihilation characteristics close to the group G3. Moreover we will see later (section 5.3.2.3) that La concentration of some samples of the group G1 is low (~1mol %) compared to nominal one. Our first data suggest that the grain size distribution decreases with the La concentration in the La doped UO_2 from the sets 1 and 2, as it has been already observed in [52].

5.3.2.2 Raman spectroscopy in Ln doped uranium oxides

a) As-received La doped uranium oxides from set 2

Several Raman spectra were measured by focusing the laser beam in the centre of one grain in different places in as-received La doped UO_2 from set 2. The spectra representative of each sample are plotted in Figure 39a.

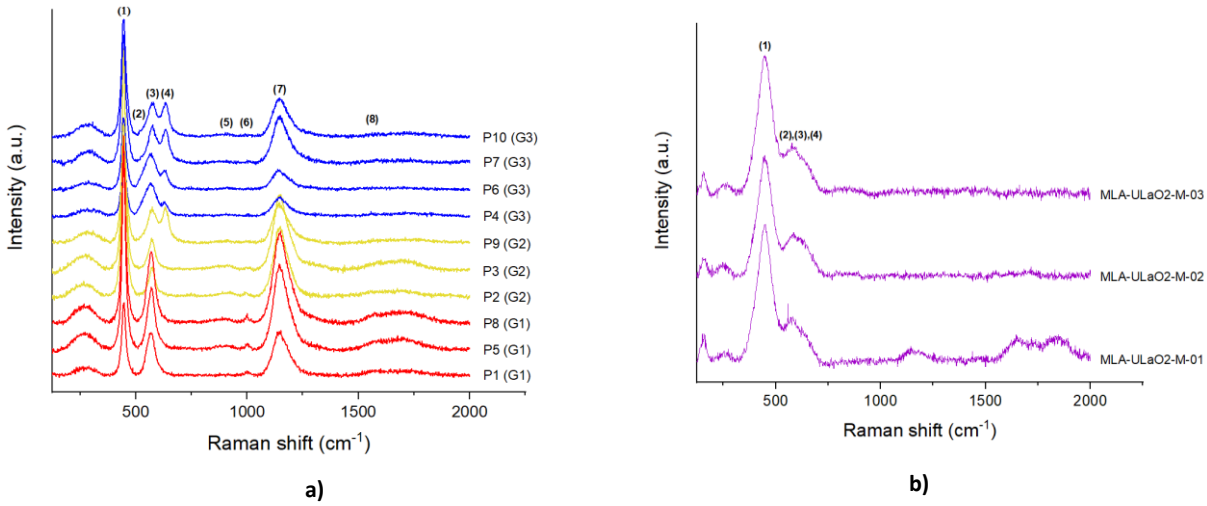

Figure 39 Raman spectra in the La doped samples from a) set 1 in as-received state and b) from set 2 after annealing at 1600 °C/2h/Ar-H_2 (10%).

Several peaks or bands are detected. Two categories of spectra can be distinguished, mainly around group G1 samples for the first category and around group G3 samples for the second category. Interestingly, the spectrum measured in P9 resembles that of group G3, while the spectra of P2 and P3 belong to the first category *i.e.* group G1. These results confirm the classification, which can be based on grain size and La concentration, as we will see later.

The main bands can have discussed as follows. In all spectra (Figure 39), we observe an intense band at 445 cm^{-1} (1) corresponding to the T_{2g} mode characteristic of the stoichiometric fluorite structure. This mode is due to the vibration of the oxygen atoms present in the lattice. A band at around 570 cm^{-1} (3) is present in all spectra. It corresponds to the optical longitudinal mode (1LO) forbidden in Raman by fluorine symmetry [101]. This symmetry break comes from the dopant (lanthanum) introduced into the samples. This band has also been observed in helium-implanted UO_2 [102]. It is therefore the signature of a disorder caused by implantation or by the addition of dopants. It is not observed in the spectra from G1 and P2 and P3 may be due to the lower concentration of La as we will see later. The band at 630 cm^{-1} (4) is visible in the following spectra: P4, P6, P7 and P10 from G3 and P9. It is linked

to local oxygen over-stoichiometry [101], which may be associated with the presence of oxygen-enriched chemical defects of the cuboctahedral type [103]. Samples with this band have an average grain size of around 3 µm. These smaller grains would facilitate oxidation of the samples. The band at around 1150 cm^{-1} (7), represents the second-order optical longitudinal mode (2LO). This mode is active at low lanthanum concentrations and should no longer appear at concentrations above 6mol % [52].

Other low intensity bands can be detected:

- Around 540 cm^{-1} (2) could correspond to oxygen vacancies [52]. It is essentially present in Group 3 spectra and P9. However, PAS indicates that this is the group with the fewest lacunar defects. The annihilation characteristics of this defect are not known and oxygen vacancy is expected to be positively charged *i.e.* difficult to detect using positron.

- Bumps can be seen in the spectra of the as-received samples P5, P8, P2, P3, P10, P7 P6 and MLA-ULaO2-M-03 at around 800-900 cm^{-1} (marked as (5) in Figure 39). Such band has been attributed to the presence of phases containing uranyl ions caused by slight oxidation of the sintered samples [52].

- The band at 1000 cm^{-1} (6) is clearly visible for G1 samples, less visible for G2 samples and almost non-existent for G3 samples. Drawing a parallel with PAS, we can speculate that bands (6) could be linked to a certain type of defect.

- Finally, bands above 1500 cm^{-1} (8) are signatures of trace amounts of carbon [104-106]. The carbon comes from the synthesis of the precursors used to manufacture the pellets. Their intensities are larger in the samples from G1.

b) La doped uranium oxides from set 1 annealed at 1600 °C/2h/Ar-H_2 (10%)

Measurements were also carried out on La (15%) doped UO_2 after annealing at 1600 °C/2h/Ar-H_2 (10%). In this case, the laser spot has a diameter identical to or even larger than the average grain size of these samples. As a result, the acquired Raman signal originates from different grains and grain boundaries (see Figure 39b). The T_{2g} band (1) is clearly larger than in the spectra measured in samples from set 2, probably due to the higher concentration of dopants. The bands 3 (570 cm^{-1}) and 4 (630 cm^{-1}) are also visible.

c) La doped uranium oxides from sets 1 and 2 after annealing at 1500 °C/5h/Ar-H_2 (10%)

The Raman spectra measured in La doped UO_2 from sets 1 and 2 after annealing at 1500 °C/5h/Ar-H_2 (10%) are shown in Figure 40. They are compared with results obtained in a Uranium oxide sample (P-FEM1-26) which has been intentionally oxidized to reach an oxygen to metal ratio of 2.21 [99].

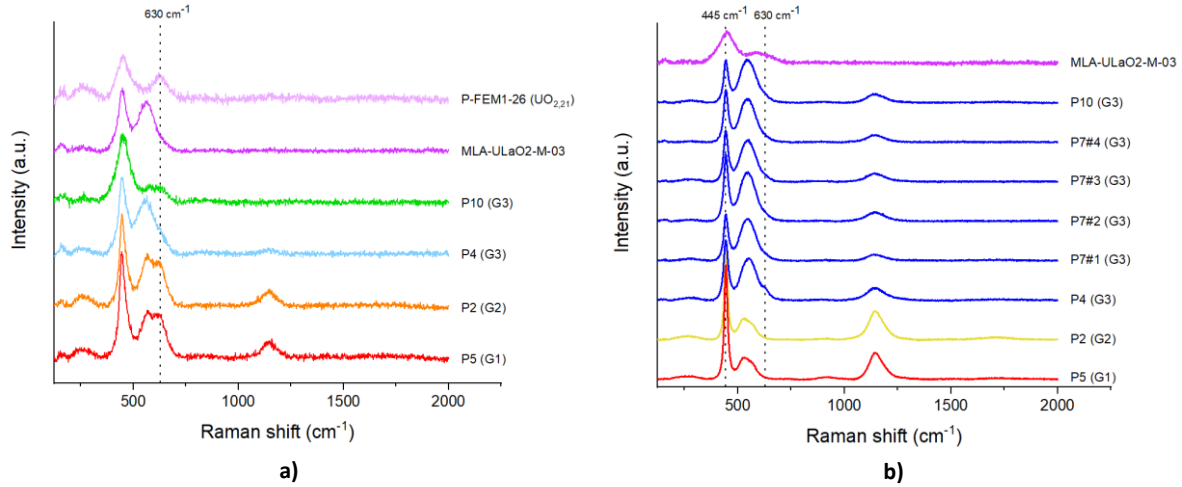

Figure 40 Raman spectra in the La doped UO_2 samples from sets 1 and 2 after annealing at 1500 °C/5h/Ar-H_2 (10%) a) first annealing with unintentional oxidation, b) second annealing in reducing conditions.

Raman spectroscopy analyses show that the band at 630 cm^{-1} detected after the first annealing carried out with an unintentional H_2O leakage has disappeared for samples P2 and P5 from the G1 group. Interestingly, this band is also observed in the over-oxidized $UO_{2.21}$ sample. Changes in the samples from set 1 and group G3 from set 2 are less clear. The intensity of the band at 630 cm^{-1} is weaker in these last samples than what we observed in the samples from set 2 G1. The band at 575 cm^{-1} has increased in MLA-03 (set 1) and in P4 (set 2, G3) but was reduced for P10 (set 2, G3) compared to Raman analyses before this first annealing.

After the second annealing in reducing atmosphere, the band at 530-540 cm^{-1} appeared for samples P2 and P5, suggesting the appearance of oxygen vacancies while the band at 630 cm^{-1} disappeared. However, the band at 630 cm^{-1} seems to be reduced but has not disappeared for G3 samples, nor for MLA-03. As we will see later the La concentration in G3 (~5mol %) samples is larger than in G1 (~1mol %). The reducing atmosphere would have eliminated the excess oxygen in the samples doped with the lowest La concentration. The results are less clear for the samples with the highest La concentration. This could be due to the smaller grain size for higher La mol %, making it difficult to probe the intra-grain.

d) La doped uranium oxides from sets 1 and 2 after annealing at 1500 °C/5h/Ar-H_2 (10%) and He implantation.

The Raman spectra measured in La doped UO_2 from sets 1 and 2 after annealing at 1500 °C/5h/Ar-H_2 (10%) and implantation with 1 MeV ^3He ions at RT and a fluency of $1 \cdot 10^{16}$ cm^{-2} are shown in Figure 41.

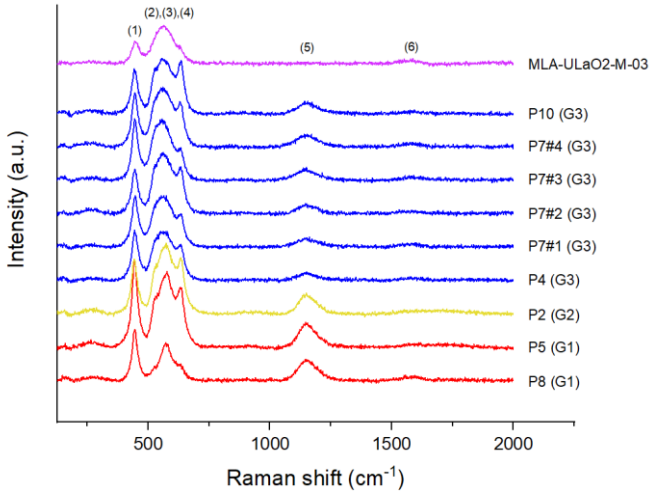

Figure 41 Raman spectra measured in La doped UO_2 from sets 1 and 2 after annealing at 1500 °C/5h/Ar-H_2 (10%) and implantation with 1 MeV ^{3}He ions at RT and a fluency of $1{\cdot}10^{16}$ cm^{-2}

The T_{2g} mode is still observed and its intensity has strongly decreased. These three bands U1 (520-530 cm^{-1} (2)), U2 (570 cm^{-1} (3)) and U3 (635 cm^{-1} (4)) correspond to modes generated by ion implantation [102]. However, the intensity of the bands varies from spectra to spectra, with the exception of the U2 mode, which remains the most intense of the triplet (U1, U2, U3) for all spectra. It is important to note that the intensity ratio between the U2 and T_{2g} modes has increased compared to the Raman analyses performed prior to implantation due to the disorder introduced into the samples.

The triplet U1, U2, U3 is a signature of the defects generated by the implantation. Guimbretière *et al.* observed these same bands in He^{2+}-implanted UO_2 samples [102]. The U3 band seems to be the result of cuboctahedral chemical defects, *i.e.* a phase containing an excess of oxygen atoms. However, these oxygen atoms do not come from oxidation during the experiment, as the samples are under high vacuum and kept at RT (the sample holder is cooled using water circulation). It suggests that these oxygen interstitials are therefore atoms initially present in the material that have been displaced by the interaction between ^{3}He and oxygen atoms. On the other hand, if there is a region with a surplus of oxygen, by reciprocity, there is another with a lack of oxygen. The U1 mode would then be an activated mode for oxygen-depleted regions. As for the U2 mode, it would be identified as the 1LO mode already present in $ULaO_{2\pm x}$ samples.

Raman spectra measured in small-grained samples - as set 1 and some samples from set 3 - are difficult to interpret in details. We recently decided to make mapping. In the figure below (Figure 42) we summarised the main results obtained by Raman spectroscopy focusing on the T_{2g} band. The T_{2g} band position shifts towards higher wavenumbers when the concentration of Lanthanum increases. At the same time the width and intensity increases and decreases, respectively. These changes are most probably related to the evolution of the lattice parameter that has been observed in La-doped UO_2 [52]. Systematic analysis of peaks characteristics is under progress for the triplet modes U1, U2 and U3. These first Raman analyses show that T_{2g} band characteristic of fluorine structure is still observed in the doped oxides. Its position, width and intensity varies as a function of the La concentration. The triplet U1, U2, U3 is a signature of the defects generated by the ^{3}He-implantation. U2, (around 570 cm^{-1}) is the signature of a disorder caused by implantation or by the addition of dopants. U3 (around 635 cm^{-1}) band seems to be the result of oxygen interstitials displaced by collisions induced ^{3}He

implantation. The U1 (around 520-540 cm^{-1}) mode could be an activated mode induced by lattice distortion of oxygen-depleted regions as it has been suggested by Desgranges et al. [107].

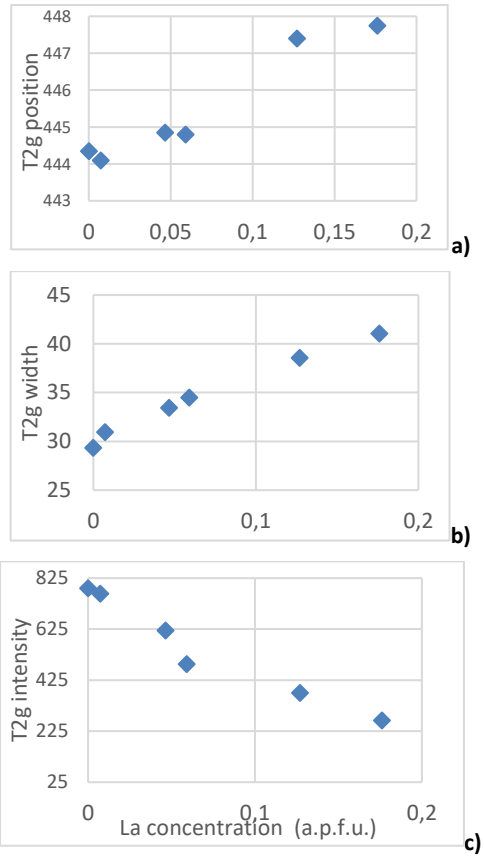

Figure 42 T_{2g} position (a), width (b) and intensity (c) in La doped UO_2 as a function of the La concentration in a.p.f.u (atomic proportion per formula *unit).*

5.3.2.3 Chemical composition characterisations using SEM/EDX

Several samples from the three sets were characterised using SEM/EDX (see Table XI). The main first results are as follows:

- Al and Si peaks have been found in the EDX spectra for all the samples. Al concentration changes from 8 to 11 mol %. The origin of such elements is not yet known. It could be contamination in the microscope or due to alumina sintering crucibles.

- The concentration of La is much less (~1mol %) than the expected value (6) in some samples (P1 and P3) from set 2. These two samples belong to groups G1 and G2 showing the same large grain size distribution.

- The concentration of Ln in the other characterised samples is close to the nominal value. This is the case for P6 and P9, which belong to group G3 with the smallest UO_2 grains in set 2. La concentration in the MLA-01 is also closed to the nominal value.

- Some Ln enrichment can be observed before or after high temperature annealing depending

on the samples. New phases are detected containing larger amount of Ln than in the matrix. They can be observed either on a large area at the periphery of sample or at very localized positions most of the time close to grain boundaries.

Table XI SEM/EDX analysis in Ln doped UO_2.

Sample	Nominal Ln doping		Set	Group	Mean grain size (µm)	Measured mean concentration (mol %)			Heterogeneities	
	Ln type	Conc. (mol %)				Ln	Al	Si	Before annealing	After annealing at 1500 °C/5h/Ar-H_2(10%)
P1	La	6	2	1	6	1	9	4	minor	minor
P3	La	6	2	2→1	6	1	11	1		minor
P6	La	6	2	3	3	5	9	1		minor
P9	La	6	2	2→3	3	5	9	1	minor	minor
MLA-01	La	15	1		1	13	9	1	Ln enriched-crystals at the surface	More Ln enriched-crystals at the surface
P1S15	La	6	3			6	11	1	minor	Ln enriched-crystals at the surface
P1S16	La	25	3			18	9	1	2 Ln-enriched phases dispersed in the matrix, a zone predominantly composed of those phases	No obvious changes
P2S2	Gd	6	3			5	9	3	Clumpy: well-polished groups of crystals are separated by deep groves	
P1S28	Gd	25	3			19	9	3	Ln-enriched crystals dispersed throughout the matrix	
P1S25	Nd	15	3			13	8	1		Ln-enriched crystals at the surface and in the matrix that tend to occur in segregations
P2S25	Nd	15	3			11	9	1	Clumps separated by thin cracks, occasional Ln-enriched crystals	More Ln-enriched crystals at the surface
P1S18	Nd	25	3			20	8	1		Clumpy, Ln-enriched crystals near grooves separating individual clumps

5.3.3 He release measurements

We used the $^3He(d,\alpha)^1H$ Nuclear Reaction Analysis (NRA) method to determine the ^3He helium amount in the samples after implantation and annealing performed in Ar-H_2 (10%) atmosphere at increasing temperature from 400 to 1100 °C during 1 to 6 hours depending on the temperature. The NRA measurements were performed in a mm-size spot close to the centre of the samples.

For the ***first He release campaign***, various samples from the sets 1 and 2 were implanted with 1 MeV ^3He ions at the fluency of $1 \cdot 10^{16}$ cm^{-2}. They are listed in Table X.

The evolution of the ^3He amount remaining in the samples after each annealing step is shown in Figure 43a for the implanted samples from sets 1 and 2. The full symbols correspond to 1 hour thermal treatment. P7-1, P7-2 and P7-4 are three pieces of the P7 sample. It should be noted that the error bar on the measured values is around 2 % and due to sample heterogeneity (density, grain size or porosity), an additional discrepancy can be observed in Figure 43 that can reach ± 5%.

These results can be compared to the He release measured in UO_2 for experiments performed under same conditions for two batches. The first (AA) is a disk cut in a pellet sintered at 1700 °C, polished and annealed at 1700 °C/24 hours/Ar-H_2 (5%). The mean grain size in this sample is larger than 10 µm. The second disk (B) is made of thin powder sintered at low temperature allowing keeping the grain size at a mean value of 400 nm before annealing at 700 °C at which grain growth was observed. The disk was polished but not annealed before implantation.

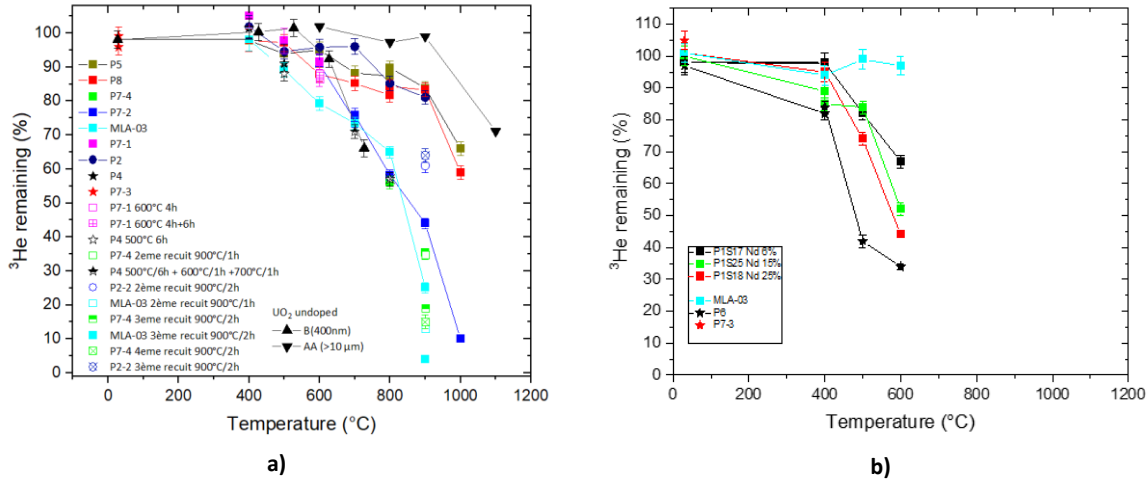

Figure 43 ^3He amount remaining in the (a) La doped UO_2 from the set 1 and 2 after annealing in Ar-H_2 (10%) atmosphere at increasing temperature during 1 to 6 hours and compared to UO_2 samples and (b) Ln doped UO_2 from the sets 1, 2 and 3 after annealing in Ar-H_2 (10%) atmosphere at increasing temperature during 1 hour.

No release is observed after annealing at 400 °C. Very slight He release is beginning to be observed at 500 °C that remains close to the sensitivity of the technique as shown for La doped UO_2 with grain size from 3 to 7 µm [108]. Then release increases with temperature at annealing duration depending on the sample. The remaining He amount is very close for all the 6% La doped samples after 600 °C and starts to be distinct from 700 °C. From this temperature, two major behaviours can be distinguished in this first experiment campaign. For all the P7 pieces and P4 belonging to the group G3, He release increases quickly when temperature increases and reach close to 90% at 1000 °C. In P5, P2 and P8 samples belonging to the group G1, the release decreases slowly up to 900 °C (reaching around 15% less of He) and then more quickly at 1000 °C to reach around 35 % and remain at a close value of 40% for 1100 °C. Two of the major differences, known to date, between the two groups are the concentration of La and the size of the grains: (1) the grains of the group G3 are smaller (mean value of ~3 µm) than for the group G1 (mean value of ~6 µm) and; (2) La concentration is lower for samples of the group G1 (~ 1mol %) than for G3 (~5mol %).

These results can be compared with the He release measured in infused La doped UO_2 with grain size from 3 to 7 µm [108]. As in our experiments, the release is the highest between 900 and 1200 °C for all La concentration. It is larger for the highest concentration of La (11 and 22mol % In [108], and 5 and about 15mol % in our study). However there is still more than 50% He in the 6mol % infused samples with grain size of 3 µm [108] at 1320 °C. In our study, the He content for the 5% doped and 3 µm grained samples becomes negligible after 900 °C whereas it is still 80% for the 1% La doped and 6 µm grained samples.

On the other hand, in the un-doped AA sample with large grain UO_2, He release starts for annealing at temperature higher than 900 °C and remains low (~30%) at 1100 °C, while for the B disk with smaller grains (400 nm) He release starts at 600 °C.

It is not possible to infer from the initial experiments which parameters control He release in these La-doped UO_2.

A ***second He release campaign*** was carried out to investigate the impact of the type of Ln dopant and its concentration. For this new campaign, Nd doped samples from the set 3 with doping concentration from 6 to 25 mol % were selected together with one La doped UO_2 (P6) from set 2, group G3. None of these samples were annealed before implantation. We have added sample MLA-03, which has already undergone the first He release campaign and whose He concentration after the last annealing (at 900 °C) is lower than 10% (see the list in Table XII). The results are shown in Figure 43b.

Table XII List of samples chosen for the second He release experiment campaign. (*) nominal concentration of dopant as expected from the sample preparation

Implantation campaign	Sample	Set	Ln doping		Group	Mean grain size (µm)	Density ($g.cm^{-3}$)	Annealing 1500 °C/Ar-H_2 (10%) (hours)
			type	Nominal concentration (mol %) *				
Campaign 2	P1S17	3	Nd	6	-	1.15±0.5	10.22	0
	P1S25	3	Nd	15	-	0.8±0.4	9.96	0
	P1S18	3	Nd	25	-	0.4±0.3	9.00	0
	MLA-03	2	La	15	-	1.08	-	After last NRA measurement (1100 °C/1h/Ar-H_2 (10%)
	P6	2	La	6	3	2.84	9.82	0

He amount after annealing depends on the location where the NRA analysis was performed and changes from 90 to 85 % as it can be seen for the P1S25 sample. He release begins at 500 °C for most of the samples except for P6 and MLA-03. At 600 °C, the He amount remaining in the samples is significantly lower (~68% at the maximum) in this new campaign than in the first (~80% at the minimum). In the Nd doped samples, the remaining He amount at 600 °C decreases from 68 to 45 % while the Nd concentration increases from 6 to 15 and 25% (as nominal values, corresponding to measured values of 13 and 20mol % for the two latest). It can be in agreement with the data obtained

in La-doped samples in [108]. Note that the overall density of these disks also decreases as the Nd concentration increases.

In the case of P6 (from group G3 of set 2), He release begins at 400 °C and increases very quickly to reach 60% while temperature increases at 500 °C. This result is radically different from that obtained for samples of the same group G3 (P4, or P7) during the first NRA campaign (see Figure 43a).

It is interesting to observe that Helium is not released in MLA-03 for temperatures up to 600 °C contrary to what might have been expected from the results of the first campaign for which a release of 20% was measured. This change could be due to the modification of the microstructure induced by the first implantation and successive annealing. He bubbles may have been created during this first campaign. These were partially emptied during high-temperature annealing to become bubbles with a low gas density, but sufficient to retain them at the end of the heat treatments (900 °C). These bubbles can trap the helium implanted during the second campaign and annealing at higher temperature is required for re-solution and diffusion to the surface.

In summary, these first studies in La and Nd doped UO_2 show that helium can be released at different temperatures depending on the samples. The lowest release temperature observed is 400 °C, and the highest is 700 °C. The evolution of release as a function of temperature depends on the samples and the remaining He amount in samples after annealing at the highest temperature (1100 °C) varies from less than 10% to 65%. At this stage, it is difficult to conclude on the origin of these differences: grain size and dopant concentration cannot be ruled out, but maybe other parameters can play a role such as roughness or porosity. Recent chemical and microstructural characterisations show that we need to carry out new experiments, including systematic sample analysis in our approach, and that the location of the NRA measurements needs to be controlled.

We have begun a new He release campaign, adopting this new approach.

5.4 Discussion and outcomes

Initial PAS studies show that the Ln-doped UO_2 studied here are not equivalent to each other. All of them contain vacancy defects of unknown nature, whose distribution depends on the sample. After annealing at high temperature (1500 °C/5h/Ar-H_2 (10%)) the concentration of defects decreases. After He implantation only U vacancy defects are detected in some samples (P2, P5) whereas other defects are also detected in P4 and P10. Annihilation of positrons in these U vacancy defects decreases strongly in P2 and P5. Whereas no change is observed in P4 and P10. The origin of these variable behaviours is not yet known, further investigations are required, in particular, a more detailed and systematic characterisation of the sample's microstructure and chemical composition, which we have recently undertaken as part of this project.

First Raman analyses show that T_{2g} band characteristic of fluorite structure is always observed in La-doped oxides. Its position, width and intensity vary with La concentration. The triplet U1, U2, U3 is a signature of the defects generated by the implantation. U2 (around 570 cm^{-1}) is the signature of a disorder caused by implantation or by the addition of dopants. The U3 band (around 635 cm^{-1}) seems to be the result of oxygen interstitials displaced by collisions induced by ^3He implantation. The U1

mode (around 520-540 cm^{-1}) could be an activated mode for oxygen-depleted regions.

The following main conclusions can be drawn from the first chemical characterisations carried out using SEM/EDX:

- Al and Si peaks have been found in the EDX spectra for all the samples. Al concentration changes from 8 to 11 mol % The origin of such elements is not yet known. It could be contamination in the microscope or due to alumina sintering crucibles.

- The concentration of La is much less (~1 mol %) than the expected value (6 mol %) in some samples (P1 and P3) from set 2. These two samples belong to groups G1 and G2 showing the same large grain size distribution.

- The concentration of Ln in the other characterised samples is close to the nominal value. This is the case for P6 and P9, which belong to group G3 with the smallest grains in set 2. La concentration in the MLA-01 is also closed to the nominal value.

- Some Ln enrichment can be observed before or after high temperature annealing depending on the samples.

Finally, the first studies of He behaviour in La and Nd doped UO_2 show that helium can be released at different temperatures depending on the samples. The lowest release temperature observed is 400 °C, and the highest is 700 °C. The evolution of release as a function of temperature depends on the samples and the remaining He amount in samples after annealing at the highest temperature varies from less than 10% to 65%. At this stage, it is difficult to conclude on the origin of these differences: grain size and dopant concentration cannot be ruled out, but maybe other parameters can play a role such as roughness or porosity. Recent chemical and microstructural characterisations show that we need to carry out new experiments, including systematic sample analysis in our approach, and that the location of the NRA measurements needs to be controlled. We have begun a new He release campaign, adopting this new approach, making:

- Systematic chemical and microstructural characterisations of the doped-UO_2 samples are indispensable to be developed.

- New experiments and controlled NRA measurements are needed to check the effect of the heterogeneity of the samples.

- Systematic analysis of Raman characteristic bands from He implanted samples in La-doped UO_2 samples is under progress for the triplet modes U1, U2 and U3 and will have to be correlated with PAS results.

- Based on current results, complementary analysis could be considered in a near future to have a clear interpretation about the dependence of He release with concentration of Ln and the grain size.

6. Summary of results

This report concludes the results of the experimental behaviour of simulated SNF pellets both under (ab-) normal dry interim storage conditions and under conditions of water contact, *i.e.* container or cladding failure scenarios, performed by EURAD WP8 subtask 3.2 participants. In particular, this report provides detailed information from the various groups involved in WP8 subtask 3.2 on the solid samples used in the experiments, the experimental conditions, and the experimental observations in a structured and coherent way. The behaviour of the "model materials" was studied on pellet and powder samples, which were prepared by the various participants by different approaches. Particularly, the preparation of the doped UO_2 samples led to a set of materials, covering most likely found in real SNF in terms of ranges of dopants, contents and microstructures. This range of material features will support the interpretation of such effects (microstructure, type of dopant and concentration) on the behaviour in single-effect and multi-parametric studies in a variety of interim storage relevant conditions. Thus, this deliverable provides a solid basis for future activities within this EURAD programme or future European projects.

6.1 Dry-type experiments

The main outcomes of the undertaken ***dry-type experiments*** are the following.

6.1.1 CIEMAT

A series of UO_2 pellets doped with different amounts of Eu_2O_3 (0–2 $^w/_o$) have been sintered, and analysed by XRD, BET, Raman and SEM. The XRD data showed that an increase in Eu dopant concentration produces a contraction of the fluorite structure possibly due to the joint effects of smaller cation size of Eu and shorter U/Eu-O bonds and/or by hypo-stoichiometry [67]. Powdered samples were also analysed by XRD, finding no differences compared to the initial pellets. Additionally, powders were also characterised by Raman spectroscopy, which confirmed the presence of oxygen vacancies in the structure as a consequence of Eu doping, demonstrated by increasing intensity of the so-called "defects band" with Eu concentration.

The impact of Eu doping on the thermal stability of UO_2 was investigated. For this purpose, powdered samples were subjected to a thermal treatment consisting of a heating ramp up to 900 °C at two oxygen concentrations (1% and 21% O_2). These studies showed that adding Eu to UO_2 slightly retards UO_2 oxidation to orthorhombic U_3O_8. Kinetic data confirm this trend, and likewise verify that lowering the oxygen concentration available delays the oxidation.

6.1.2 HZDR

In this study, the UO_2 based SIMFUEL and UO_2 samples have been prepared, characterised and used as an analogue material for SNF for oxidation studies. New synthesis methods (*i.e.* co-precipitation) have been designed and investigated. The composition of SIMFUEL was 0.6 % wt. for Mo, Zr and Ru; 0.3 % for Zr and Ba; and 1 % wt. for Nd. The as-fabricated compounds have been characterised by several multi-scale techniques to study the secondary phases and both actinide and FP speciation. The as-synthesized materials have been subjected to oxidative environment in air at 300

˚C during 1 week to study the effect of the oxidation. Apparently, the oxidised SIMFUEL sample prepared by co-precipitation seems a bit less oxidised than the other obtained by solid-state route, however this work is still undergoing.

Considering that the SNF presents a heterogeneous grain size distribution along its radius, the effect of the grain size on the UO_2 oxidation behaviour has been studied. No U_3O_8 was detected in the nano grain sized sample after about 11 h oxidation in air, while the micro and sub-µ samples were almost fully converted to U_3O_8. This could have positive implications in the safety of SNF storage, as the formation of U_3O_8 involves a 36% volume expansion, detrimental for the rod integrity, and will trigger cracking of the material. Such a finding is particularly important considering that the peripheral region of SNF is constituted of the high-burnup structure (HBS), whose grain size is in the order of magnitude of the nano sample used in this work.

6.1.3 CEMHTI/CNRS

First chemical and microstructure characterization of various La and Nd doped uranium oxide samples show that the real concentration (in mol %) of dopant can be different from the nominal one (four different La mol % of 1, 5, 15 and ~20, and 5, 13 and 20 mol % for Nd doping). Local Ln enrichment is observed in some samples. The grain size increases while the concentration of Ln increases.

Concerning the characterization of defects, first PAS investigations show that the Ln-doped UO_2 samples studied here are not similar in the as-received state and exhibit various distributions of unknown vacancy defects that depend on La concentration. PAS is sensitive to the stoichiometry deviation (when O/M >2) when high-temperature annealing is carried out in oxidized atmosphere, as confirmed using Raman. After high-temperature annealing in a reducing atmosphere (1500 °C/5h/Ar-H_2 (10%)), the concentration of defects decreases. After He implantation, PAS detects only U vacancy defects in samples containing the lowest concentration of La (~ 1 mol %), while other types of vacancy defects are also detected for higher La concentrations. The positron signals measured in these samples are not referenced in current databases, which do not incorporate the presence of lanthanides in UO_2. It would be desirable to calculate these signals for mixed oxides $(U,Ln)O_x$ to help identify these unknown defects. Raman measurements show an increase of the three bands associated to U displacement in UO_2. Annihilation at these U vacancy defects decreases strongly in samples with La concentration of 1 mol %, whereas no change is observed in samples with a concentration of 5 mol %. After implantation of ^{3}He, the results of Helium release showed a dependence on the temperature as a function of the samples, La and Nd doped UO_2. The lowest release temperature observed is 400 °C, and the highest is 700 °C. It is difficult to conclude on the origin of these differences (grain size and dopant concentration, or other parameters such as roughness or porosity). More detailed and systematic characterisation of the samples are required in the as-received Ln doped UO_2 to obtain conclusions from PAS results, and then, to better understand the behaviour of gaseous fission products, particularly He, in prediction of the fuel (UO_2) performance in dry storage.

6.2 Wet-type experiments

The main outcomes of the undertaken ***wet-type experiments*** are the following.

6.2.1 CIEMAT

Static dissolution experiments were performed at CIEMAT with UO_2 pellets doped with different amounts of Eu_2O_3 (0–2 $^w/_o$) under two boric acid concentrations (1600 and 3500 ppm), reproducing some relevant wet storage conditions (spent fuel pools). The trend and values in both systems for U concentrations and specific surface area (SSA) normalised dissolution rates for U are similar, *i.e.* a decrease of dissolution rate with increasing Eu content in the solid solution. Post-leaching examinations by SEM of the pellets´ surface reveal that, for the samples containing 2 $^w/_o$ Eu_2O_3, some kind of aggregates appears for both boric acid concentrations, even after 1 day of dissolution. These formed phases on the surface need further characterisation in order to be fully understood. Nevertheless, the results point out that the trivalent dopant is directly related to the formation of such aggregates.

6.2.2 ICSM/CNRS

A series of UO_2 pellets and UO_2 doped with FP (PGM; Ln: Lanthanides: Y, La, Pr, Ce, Nd; Mo) samples were prepared using wet chemistry route. The following conclusions are drawn from dissolution experiments:

- Several types of well-densified materials representative of used fuels were prepared by wet chemistry route and then sintered at 1600°C.

- Developed surface areas, determined by image analysis (SESAM method) were evaluated to range between $2{\cdot}10^{-2}$ and 10^{-1} $m^2{\cdot}g^{-1}$. From Iglesias et al 2008 [109], it was referred a value for a fuel pellet from Forsyth et al 1995 of 0.007 – 0.015 $m^2{\cdot}g^{-1}$ using the BET method with Kr sorption, larger than the calculated geometrical surface area. Within the same review article of Iglesias et al, one can found values of geometric area (roughness factor) 0.0002 m^2 g^{-1} or even lower. As is generally known, differences might be attributed to the approach used (sorption gas by BET, the application of a roughness factor or not), the preparation of the samples and the different precedence of the material (as sintering conditions or the history of the material). All of the mentioned issues can significantly affect the final densification rates, and thus the porosity and the specific surface area.

- Sintered samples (UO_2, $(U,Ln)O_2$, UO_2:PGM, UO_2:PGM+Mo and $(U,Ln)O_2$: PGM+Mo+Ln) were submitted to long-term dissolution tests in air, at 50°C and 70°C, in deionized water, in solutions containing boric acid (2500 ppm, *i.e.* $2.3{\cdot}10^{-4}$ $mol{\cdot}L^{-1}$ H_3BO_3, pH = 5) and in solutions containing boric acid and lithin ($2.3{\cdot}10^{-4}$ $mol{\cdot}L^{-1}$ H_3BO_3, LiOH, pH = 7).

- Dissolution tests performed on UO_2 and $(U,Ln)O_2$ suggests a beneficial impact of Ln elements on the chemical durability of the ceramics for the three conditions examined (with a decrease by a factor of 5 to 20 of the normalised dissolution rate).

- For UO_2:PGM ceramics, a plateau was observed after 250 days suggesting the formation of neo-formed phase. The direct comparison of the dissolution rates

obtained for UO_2 and UO_2:PGM showed no significant effect of PGM elements when dissolution at pH =7 and an increased by a factor of 4 to 5 at pH = 5. UO_2:PGM pellet dissolved 25 to 30 times more slowly at pH = 7 than at pH = 5 whatever the presence (or not) of boric acid in the leaching solution.

- Comparison of dissolution of UO_2:PGM with that of UO_2:PGM+Mo in the three studied media did not reveal any significant impact of molybdenum on the chemical durability of the leached samples.

- The direct comparison of the dissolution tests performed for UO_2:PGM+Mo and UO_2:PGM+Mo+Ln revealed that the normalised dissolution rates were reduced by about one decade for the three studied leaching solutions in the presence of Ln elements. This could result from the U speciation in the sintered materials, which is strongly affected by the presence of Ln elements.

- Saturation phenomena were observed at pH = 7 for $(U,Ln)O_2$ and UO_2:PGM for dissolution test longer than 60 and 250 days, respectively.

- Small nodules (less than a few tens of nanometres in size), not yet identified, were formed at the surface of $(U,Ln)O_2$ solid solutions (with 6 mol % Ln).

- Operando monitoring by ESEM during dissolution of UO_2:PGM samples at 50 °C and pH = 7 revealed the formation of platelets type crystals onto the surface of the leached material in the presence of lithine. Formation of Li-compreignacite $Li_2[(UO_2)_6O_4(OH)_6]\cdot 8H_2O$ was suggested by XRD and Raman spectroscopy.

- Dissolution the UO_2:PGM samples at 50°C and pH = 5 revealed the formation of meta-shoepite $(UO_2)_8O_2(OH)_{12}\cdot 10H_2O$ or U hydroxide β-$UO_2(OH)_2$, with the formation of bigger crystals compared to that obtained for Li-compreignacite.

7. General conclusions

This report is a result of a collaboration of various nuclear research organisations (CIEMAT, ICSM, CNRS, HZDR and CEMHTI) and provides new data on different aspects of predisposal management of SNF, particularly focused on interim storage, using an empirical approach. Since there is no universal solution for SNF management applicable to all countries, it is necessary to consider general approaches and boundary conditions in a range of realistic scenarios that can be constructive as a basis for a good integration in each RWM strategy. Interim storage solutions for SNF are needed regardless of the fuel cycle strategy.

The changes in physico-chemical attributes of irradiated UO_2, in comparison with pristine UO_2, is established to be mostly influenced by: 1) the increase of solid FP (both as solid solutions and precipitates); 2) formation and diffusion of fission gas bubbles and; 3) radiation damage. All these microstructural changes in the fuel become progressively more marked with increasing fuel burnup. The understanding of SNF behaviour in whatever phase of the back-end of the nuclear fuel cycle (with decoupled and synergic effects) is incomplete for safety assessment. In addition, due to well-known radiation constraints, associated to experiments with real irradiated fuels, makes it necessary to use "designed" systems (also called "model materials"). By means of non-irradiated simplified surrogates it is possible, on one hand, to optimize and validate analytical procedures for being applied to irradiated fuel. On the other hand, the experimental approaches developed can be "conservatively" demonstrated (conservative in terms of "corrosion resistance"). The potential contact between fuel pellets and gaseous atmosphere [110-116] or aqueous environment [117, 118] during its temporary storage has been studied in the past to some extent. Nevertheless, important gaps in the knowledge of interactions between UO_2 with oxidising agents (gas or aqueous) in the event of an undetected cladding breach still exist. To test the scientific hypothesis of FPs effect hindering UO_2 matrix corrosion, the use of model materials with trivalent dopants may clarify this isolated effect or other overlapping and synergistic phenomena by abductive reasoning. This speculation, whether the doping effect of FPs in UO_2 alteration reduces corrosion, requires in-depth examination for confirmation. Those are the principal aims of this subtask 3.2, devoted to study the role of FP and the microstructure on oxidation/dissolution of UO_2 under dry interim storage and pool water conditions. The main outcomes for each type of experiment are presented below.

<u>Dry oxidation experiments:</u>

Here, we have examined the impact of dopants and grain size distribution on the thermal stability of UO_2, which is known to be related to the burnup. Using UO_2 based model materials the presence of different ranges of dopants, contents and microstructures can be assessed. In general, lanthanide doping retards oxidation of UO_2 to U_3O_8. Specifically, the influence of Eu doping and oxygen concentrations on matrix oxidation was investigated in-situ as a function of temperature. The investigated thermal treatments of UO_2 doped with Eu_2O_3 (0–2 $^{w}/_{o}$) showed that Eu slightly delays the oxidation of UO_2 to U_3O_8. Kinetic data confirm this trend, and also verify that lowering the oxygen concentration delays the oxidation (CIEMAT). The oxidation behaviour in air at 300 ˚C during 1 week of as-prepared SIMFUEL (0.6 % wt Mo, Zr and Ru; 0.3 % Zr and Ba; and 1 % wt for Nd) by wet-route seems a bit less oxidised than the doped UO_2 obtained by solid-state route (HZDR). Differences in the

formation of U_3O_8 at isothermal conditions between the micro-, sub-µ- and nano-UO_2 samples, appear to indicate that nano-sized sample, whose grain size is in the order of magnitude of the peripheral region (HBS) of SNF, inhibits U_3O_8 formation (HZDR). The results from the influence of the He implantation on the formation of vacancy defects and the Helium release showed a dependence on the temperature as a function on Ln concentration, in La and Nd doped UO_2. The lowest He-release temperature observed is 400 °C, and the highest is 700 °C. However, it is difficult to conclude on the origin of these differences; apparently it depends on grain size, dopant concentration, or other parameters such as roughness or porosity (CEMHTI). Model development is underway to assess the effect of microstructure-related parameters.

Wet dissolution experiments:

Here, we have examined the role of FP on microstructure and chemical durability of UO_2 under aqueous conditions, i.e. wet interim storage conditions (pool). The work carried out with UO_2 pellets doped with different amounts of Eu_2O_3 (0–2 $^w/_o$) corroded in solutions with two boric acid concentrations (1600 and 3500 ppm) shown that the trend and values in both systems for U concentrations and normalized dissolution rates for U were quite similar. A decrease of dissolution rate with increasing Eu content in the solid solution was observed. Post-leaching examinations by SEM of the pellets´ surface reveal that, for the samples containing 2 $^w/_o$ Eu_2O_3, some kind of aggregates appears for both boric acid concentrations, even after 1 day of dissolution. These newly formed phases on the surface need further characterisation in order to be fully understood. Nevertheless, the results point out that the trivalent dopant is directly related to the formation of these aggregates (CIEMAT). In relation to the studies carried out by ICSM/CNRS, long-term dissolution experiments were performed with UO_2 pellets and UO_2 doped with FP (PGM; Ln: Lanthanides: Y, La, Pr, Ce, Nd; Mo) samples. These experiments were done in air, at 50°C and 70°C, in: 1) deionised water; 2) solutions containing boric acid (2500 ppm, *i.e.* $2.3 \cdot 10^{-4}$ mol·L^{-1} H_3BO_3, pH = 5); and 3) in solutions containing boric acid and lithin ($2.3 \cdot 10^{-4}$ mol·L^{-1} H_3BO_3, LiOH, pH = 7). The corrosion tests on UO_2 and (U,Ln)O_2 suggests a beneficial impact of Ln elements on the chemical durability of the ceramics for the three conditions examined, as these elements incorporated into the fluorite structure can influence U release. Obtained results from the comparison of the dissolution rates for UO_2 and UO_2:PGM demonstrated no significant effect of PGM elements when leaching at pH =7, and 4 to 5 times higher at pH =5. In addition, when the dissolution rate of UO_2:PGM is compared to UO_2:PGM+Mo, no significant impact of molybdenum on the chemical durability of the leached samples was observed. However, when comparing the dissolution rate of UO_2:PGM+Mo with UO_2:PGM+Mo+Ln revealed dissolution rates by about one decade lower (in the presence of Ln elements). The analysis of the surface of the (U,Ln)O_2 and UO_2:PGM leached samples showed saturation phenomena at 50 °C, pH = 7 and leaching time longer than 60 and 250 days, with the formation of neo-formed phases containing U (ICSM/CNRS). These findings show the important role of trivalent lanthanides, such as La, Ce, Pr, Nd, and Eu, on the reduced oxidative dissolution of fuel matrix when pellets are exposed to pool waters over extended periods after cladding breach. Ln-doped UO_2 fuel pellets have been observed to remain stable for periods from 30 to almost 700 days. Based on these experimental data, relatively low dissolution rates of uranium were exhibit in those samples where lanthanides are present, from "3 10^{-6} to 5 10^{-4} g.m^{-2}.d^{-1}".

Previous projects like DISCO, were focused on the redox reactivity of UO_2 doped with trivalent

additives with H_2O_2. Those studies showed that additions of trivalent elements, reduce the redox reactivity of UO_2, and therefore confirms our reduced oxidative dissolution rate under boric acid system.

Our goal was to find correlations between lanthanides doping (as FP) and fuel matrix degradation, not so obviously related, which would make it possible to study separate effects and to predict the SNF behaviour. The SNF behaviour has been studied in many previous projects funded by Euratom (SFS (2001-2004), NF-PRO (2004-2007), MICADO (2006-2009), REDUPP (2011-2014), FIRST-Nuclides (2012 -2014) and DISCO (2017-2021)) [5-10]; however, all of them were focused on the quantitative understanding of key processes affecting the SNF under geological repository conditions. An important difference of EURAD project from the research performed in those projects is that the central issue relates to interim storage. Therefore, we focused on examining the chemical reactions under dry or wet interim conditions, considering several individual and joined factors that influence the UO_2 corrosion: environment or medium (temperature, gas composition and water chemistry) and inner attributes of fuel (composition and microstructure). While these analyses focused to evidence the FPs effect hindering UO_2 matrix corrosion add to knowledge of safety assessment during predisposal, some questions and uncertainties remain, as is usually the situation in research. Firstly, this work does not aim to accurately reproduce all features and experimental behaviour of SNF, but allows to estimate effects of: dopant, microstructure and He effects on fuel pellet durability to degradation by oxidant gases or water. To bridge the gap between “model materials” and the complex real SF systems, inter-comparative analysis should be done to definitively verify the experimental conclusions reached and with associated uncertainties, or data obtained could be validated through the response of predictive models applied for irradiated fuel. Secondly, from our knowledge, we are sure that with these empirical data combined with computational approaches handling both kinetics and thermodynamics, we have progressed towards an understanding of the role of trivalent lanthanides and microstructure within the context of traditional LWR fuels interim storages. At this stage, it is not possible to conclude the agreement between the empirical tests by using model materials, the real SNF and the predictions of chemical codes. The quantitative reproduction of the large experimental data with the conceptual models would help to explain key chemical reaction mechanisms. Overall, it is emphasised the need to be further addressed on reliable behaviour characterisation of SNF at long-term in different environments. The findings and conclusions reached from these investigations constitute a comprehensive study that should be accounted by different stakeholders including research organisations, decision-makers, WMOs, regulators and the broader public in Europe.

8. Acknowledgements

The authors express their gratitude to Paul Carbol /JRC for their extremely valuable contributions to reviewing the manuscript.

The research leading to these results has received funding from the European Commission Horizon 2020 Research and Training Programme of the European Atomic Energy Community (EURATOM) (H2020-NFRP-2016-2017-1) under grant agreement n° 847593 (EURAD project).

The authors acknowledge all the colleagues at CIEMAT, CNRS, JRC, HZDR and ESRF who contribute to this work.

References

[1] NEA, "Safety of Long-term Interim Storage Facilities: Workshop Proceedings Munich, Germany 21-23 May 2013," OECD Publishing, Paris2014.

[2] IAEA, "Predisposal Management of Radioactive Waste," Viena2009.

[3] IAEA, *Predisposal Management of Radioactive Waste from Nuclear Power Plants and Research Reactors*. Vienna: INTERNATIONAL ATOMIC ENERGY AGENCY, 2016.

[4] NEA, "Multifactor Optimisation of Predisposal Management of Radioactive Waste: Proceedings of the NEA Joint Workshop," 2021.

[5] C. Poinssot, C. Ferry, M. Kelm, J. M. Cavedon, C. Corbel, C. Jegou*, et al.*, "Spent fuel stability under repository conditions - final report of the european project," France2005.

[6] EC, "Understanding and Physical and Numerical Modelling of the Key Processes in the Near Field and their Coupling for Different Host Rocks and Repository Strategies (NF-PRO). Final report.," 2008.

[7] B. Grambow, J. Bruno, L. Duro, J. Merino, A. Tamayo, C. Martin*, et al.*, "MICADO: Model Uncertainty for the Mechanism of Dissolution of Spent Fuel in Nuclear Waste Repository, EURATOM Final activity report (Contract No.: FI6W-036366)," Brussels, Belgium2010.

[8] L. Z. Evins, P. Juhola, and M. Vähänen, "REDUPP. Final report.," Posiva Oy2014.

[9] B. Kienzler, L. Duro, K. Lemmens, V. Metz, J. D. Pablo, A. Valls*, et al.*, "Summary of the Euratom Collaborative Project FIRST-Nuclides and Conclusions for the Safety Case," *Nuclear Technology,* vol. 198:3, pp. 260-276, 2017.

[10] L. Z. Evins, Bosbach D, Duro, L., Farnan I, Metz V, Riba O., "DISCO Final Scientific Report. Grant Agreement: 755443.," 2021.

[11] IAEA, *Storage of Spent Nuclear Fuel*. Vienna: INTERNATIONAL ATOMIC ENERGY AGENCY, 2020.

[12] A. Milena-Pérez, N. Rodríguez-Villagra, F. Feria, C. Aguado, and L. E. Herranz, "Critical review of fuel oxidation database under dry storage conditions," *Progress in Nuclear Energy,* vol. 165, p. 104914, 2023/11/01/ 2023.

[13] A. Milena-Pérez, L. J. Bonales, N. Rodríguez-Villagra, and H. Galán, "Exploring the impact of temperature and oxygen partial pressure on the spent nuclear fuel oxidation during its dry management," *Scientific Reports,* vol. 13, p. 1966, 2023/02/03 2023.

[14] M. G. Bunn, J. Weeks, J. P. Holdren, A. M. Macfarlane, S. E. Pickett, A. Suzuki*, et al.*, "Interim Storage of Spent Nuclear Fuel: A Safe, Flexible, and Cost-Effective Approach to Spent Fuel Management," 2001.

[15] D. Endres, "From wasteland to waste site: the role of discourse in nuclear power's environmental injustices," *Local Environment,* vol. 14, pp. 917-937, 2009/11/01 2009.

[16] D. W. Shoesmith, "Fuel corrosion processes under waste disposal conditions," *Journal of Nuclear Materials,* vol. 282, pp. 1-31, 2000.

[17] E. C. Buck, B. D. Hanson, and B. K. McNamara, "The geochemical behaviour of Tc, Np and Pu in spent nuclear fuel in an oxidizing environment," *Geological Society, London, Special Publications,* vol. 236, pp. 65-88, 2004.

[18] R. C. Ewing, "Long-term storage of spent nuclear fuel," *Nat Mater,* vol. 14, pp. 252-257, 2015.

[19] C. Corkhill and N. Hyatt. (2018). *Nuclear Waste Management*. Available: https://dx.doi.org/10.1088/978-0-7503-1638-5

[20] H. Charlton, G. Baldinozzi, and M. Patel, "A review of the oxygen vacancy ordering in surrogate structures simulating Pu-based nuclear ceramics," *Frontiers in Nuclear Engineering,* vol. 1, 2023-January-04 2023.

[21] B. Kienzler and H. Geckeis, "Radioactive wastes and disposal options," *EPJ Web Conf.,* vol. 189, p. 00014, 2018.

[22] J. Bruno, L. Duro, and F. Diaz-Maurin, "13 - Spent nuclear fuel and disposal," in *Advances in Nuclear Fuel Chemistry*, M. H. A. Piro, Ed., ed: Woodhead Publishing, 2020, pp. 527-553.

[23] K. Spahiu, " State of the Knowledge Report - Spent Nuclear Fuel Domain 3.1.1. EURAD - European Joint Programme on Radioactive Waste Management (847593)," 2021.

[24] S. Caruso, E. Vlassopoulos, R. Dagan, L. Fiorito, M. Herm, P. Jansson*, et al.*, "EURAD project Deliverable 8.1: State-of-the-art report. Work Package 8," NAGRA2022.

[25] A. Sjöland, P. Christensen, L. Z. Evins, D. Bosbach, L. Duro, I. Farnan*, et al.*, "Spent nuclear fuel management, characterisation, and dissolution behaviour: progress and achievement from SFC and DisCo," *EPJ Nuclear Sci. Technol.,* vol. 9, p. 13, 2023.

[26] D. A. Rochman, F. Álvarez-Velarde, R. Dagan, L. Fiorito, S. Häkkinen, M. Kromar*, et al.*, "On the estimation of nuclide inventory and decay heat: a review from the EURAD European project," *EPJ Nuclear Sci. Technol.,* vol. 9, p. 14, 2023.

[27] R. J. McEachern and P. Taylor, "A review of the oxidation of uranium dioxide at temperatures below 400°C," *Journal of Nuclear Materials,* vol. 254, pp. 87-121, 1998/04/01/ 1998.

[28] A. Milena-Pérez, N. Rodríguez-Villagra, S. Fernández-Carretero, and A. Núñez, "Thermal air oxidation of UO2: Joint effect of precursor's nature and particle size distribution," *Progress in Nuclear Energy,* vol. 159, p. 104629, 2023/05/01/ 2023.

[29] P. Taylor, D. D. Wood, D. G. Owen, and G.-I. Park, "Crystallization of U3O8 and hydrated UO3 on UO2 fuel in aerated water near 200°C," *Journal of Nuclear Materials,* vol. 183, pp. 105-114, 1991/07/01/ 1991.

[30] N. Rodríguez-Villagra, L. J. Bonales, A. Milena-Pérez, and H. Galán, "A snapshot review on uranyl secondary phases formation in aqueous systems," *MRS Advances,* vol. 8, pp. 207-213, 2023/06/01 2023.

[31] W. B. Wilson, C. A. Alexander, and A. F. Gerds, "Stabilization of UO2," *Journal of Inorganic and Nuclear Chemistry,* vol. 20, pp. 242-251, 1961/12/01/ 1961.

[32] L. E. J. Roberts, "The actinide oxides," *Quarterly Reviews, Chemical Society,* vol. 15, pp. 442-460, 1961.

[33] D. C. Hill, "Phase Relations and Crystal Chemistry in the System Uranium Oxide–Lanthanum Oxide," *Journal of the American Ceramic Society,* vol. 45, pp. 258-263, 1962.

[34] K. Suresh Kumar, T. Mathews, H. P. Nawada, and N. P. Bhat, "Oxidation behaviour of uranium in the internally gelated urania–ceria solid solutions – XRD and XPS studies," *Journal of Nuclear Materials,* vol. 324, pp. 177-182, 2004/01/15/ 2004.

[35] C. Jégou, R. Caraballo, S. Peuget, D. Roudil, L. Desgranges, and M. Magnin, "Raman spectroscopy characterization of actinide oxides (U1−yPuy)O2: Resistance to oxidation by the laser beam and examination of defects," *Journal of Nuclear Materials,* vol. 405, pp. 235-243, 2010/10/30/ 2010.

[36] R. Eloirdi, P. Cakir, F. Huber, A. Seibert, R. Konings, and T. Gouder, "X-ray photoelectron spectroscopy study of the reduction and oxidation of uranium and cerium single oxide compared to (U-Ce) mixed oxide films," *Applied Surface Science,* vol. 457, pp. 566-571, 2018/11/01/ 2018.

[37] C. Ferry, C. Poinssot, C. Cappelaere, L. Desgranges, C. Jegou, F. Miserque*, et al.*, "Specific outcomes of the research on the spent fuel long-term evolution in interim dry storage and deep geological disposal," *Journal of Nuclear Materials,* vol. 352, pp. 246-253, 6/30/ 2006.

[38] B. Grambow, J. Bruno, L. Duro, J. Merino, A. Tamayo, C. Martin*, et al.*, *Final Activity Report : Project MICADO Model for Uncertainty for the mechanism of dissolution of spent fuel in nuclear waste repository*, 2010.

[39] A. C. Scheinost, J. Claussner, J. Exner, M. Feig, S. Findeisen, C. Hennig*, et al.*, "ROBL-II at ESRF: a synchrotron toolbox for actinide research," *Journal of Synchrotron Radiation,* vol. 28, pp. 333-349, 2021.

[40] S. Fernandez, M. I. Nieto, J. Cobos, and R. Moreno, "CeO2 pellet fabrication as spent fuel matrix analogue," *Journal of the European Ceramic Society,* vol. 36, pp. 3505-3512, 2016.

[41] A. Milena-Pérez, L. J. Bonales, N. Rodríguez-Villagra, S. Fernández, V. G. Baonza, and J. Cobos, "Raman spectroscopy coupled to principal component analysis for studying UO2 nuclear fuels with different grain sizes due to the chromia addition," *Journal of Nuclear Materials,* vol. 543, p. 152581, 2021/01/01/ 2021.

[42] N. Rodríguez-Villagra, O. Riba, A. Milena-Pérez, J. Cobos, L. Jimenez-Bonales, S. Fernández-Carretero*, et al.*, "Dopant effect on the spent fuel matrix dissolution of new advanced fuels: Cr-doped UO2 and Cr/Al-doped UO2," *Journal of Nuclear Materials,* vol. 568, p. 153880, 2022/09/01/ 2022.

[43] S. Brunauer, P. Emmet, and E. Teller, "Adsorption of Gases in Multimolecular Layers," *Journal of the American Chemical Society,* vol. 60, p. 309, 1938.

[44] E. Iglesias and J. Quiñones, "Analogous materials for studying spent nuclear fuel: The influence of particle size distribution on the specific surface area of irradiated nuclear fuel," *Applied surface science,* vol. 254, pp. 6890–6896, 2008.

[45] "ASTM E112-13 . Standard Test Methods for Determining Average Grain Size," in *ASTM International: West Conshohocken, PA, USA.*, ed, 2013.

[46] J. Kim, J. Lee, Y.-S. Youn, N. Liu, J.-G. Kim, Y.-K. Ha*, et al.*, "The Combined Influence of Gadolinium Doping and Non-stoichiometry on the Structural and Electrochemical Properties of Uranium Dioxide," *Electrochimica Acta,* vol. 247, pp. 942-948, 2017/09/01/ 2017.

[47] R. Venkata Krishnan, R. Babu, A. Senapati, G. Jogeswararao, and K. Ananthasivan, "Thermophysical properties of uranium–europium mixed oxides," *Journal of Advanced Ceramics,* vol. 4, pp. 253-259, 2015.

[48] R. Venkata Krishnan, G. Jogeswararao, G. Panneerselvam, M. P. Antony, and K. Ananthasivan, "Solid solubility and thermal expansion studies of uranium–europium mixed oxides," *Journal of Nuclear Materials,* vol. 465, pp. 719-723, 2015.

[49] E. K. Papynov, O. O. Shichalin, I. Y. Buravlev, A. S. Portnyagin, V. Y. Mayorov, A. A. Belov*, et al.*, "UO2-Eu2O3 compound fuel fabrication via spark plasma sintering," *Journal of Alloys and Compounds,* vol. 854, p. 155904, 2021/02/15/ 2021.

[50] K. Iwasaki, T. Matsui, K. Yanai, R. Yuda, Y. Arita, T. Nagasaki*, et al.*, "Effect of Gd2 O3 Dispersion on the Thermal Conductivity of UO2," *Journal of Nuclear Science and Technology,* vol. 46, pp. 673-676, 2009.

[51] J. Lee, J. Kim, Y.-S. Youn, N. Liu, J.-G. Kim, Y.-K. Ha*, et al.*, "Raman study on structure of U1−yGdyO2−x (y=0.005, 0.01, 0.03, 0.05 and 0.1) solid solutions," *Journal of Nuclear Materials,* vol. 486, pp. 216-221, 2017/04/01/ 2017.

[52] Z. Talip, T. Wiss, P. E. Raison, J. Paillier, D. Manara, J. Somers*, et al.*, "Raman and X-ray Studies of Uranium–Lanthanum-Mixed Oxides Before and After Air Oxidation," *Journal of the American Ceramic Society,* vol. 98, pp. 2278-2285, 2015.

[53] J. M. Elorrieta, L. J. Bonales, N. Rodríguez-Villagra, V. G. Baonza, and J. Cobos, "A detailed Raman and X-ray study of UO2+x oxides and related structure transitions," *Physical Chemistry Chemical Physics,* vol. 18, pp. 28209-28216, 2016.

[54] J. Lee, J. Kim, Y.-S. Youn, J. W. Kim, and S. Lim, "Surface characterization of (U,Nd)O2: the influence of trivalent-dopant on structure of UO2," *Progress in Nuclear Science and Technology,* vol. 5, pp. 33-36, 2018.

[55] H. He and D. Shoesmith, "Raman Spectroscopic Studies of Defect Structures and Phase Transition in Hyper-Stoichiometric UO2+x," *Physical Chemistry Chemical Physics,* vol. 12, pp. 8108-17, 2010.

[56] T. Livneh, "Resonant Raman scattering in UO_2 revisited," *Physical Review B,* vol. 105, p. 045115, 01/11/ 2022.

[57] IAEA, "Storage of Spent Nuclear Fuel," International Atomic Energy Agency, Vienna2012.

[58] IAEA, "Storage of Spent Fuel from Power Reactors - Proceedings of a symposium held in Vienna, 9-13 November 1998," Vienna1999.

[59] *ASTM-E1582-14 "Standard Practice for Calibration of Temperature Scale for Thermogravimetry"ed. West Conshohocken, PA, USA*, 2017.

[60] D. R. Costa, M. Hedberg, S. C. Middleburgh, J. Wallenius, P. Olsson, and D. A. Lopes, "Oxidation of UN/U2N3-UO2 composites: an evaluation of UO2 as an oxidation barrier for the nitride phases," *Journal of Nuclear Materials,* vol. 544, p. 152700, 2021/02/01/ 2021.

[61] R. D. Scheele, B. D. Hanson, and A. M. Casella, "Effect of added gadolinium oxide on the thermal air oxidation of uranium dioxide," *Journal of Nuclear Materials,* vol. 552, p. 153008, 2021.

[62] D. Bosbach, C. Cachoir, E. Myllykylä, C. Jegou, N. Rodríguez-Villagra, I. Farnan*, et al.*, "DISCO Project Report - Model materials experiments: Final dissolution results," European Commission2021.

[63] A. Casella, B. Hanson, and W. Miller, "The effect of fuel chemistry on UO2 dissolution," *Journal of Nuclear Materials,* vol. 476, pp. 45-55, 2016.

[64] A. Barreiro Fidalgo and M. Jonsson, "Radiation induced dissolution of (U, Gd)O2 pellets in aqueous solution – A comparison to standard UO2 pellets," *Journal of Nuclear Materials,* vol. 514, pp. 216-223, 2019.

[65] K. Park and D. R. Olander, "Defect models for the oxygen potentials of gadolinium-and europium-doped urania," *Journal of Nuclear Materials,* vol. 187, pp. 89-96, 1992/03/01/ 1992.

[66] J.-G. Kim, Y.-K. Ha, S.-D. Park, K.-Y. Jee, and W.-H. Kim, "Effect of a trivalent dopant, Gd3+, on the oxidation of uranium dioxide," *Journal of Nuclear Materials,* vol. 297, pp. 327-331, 2001.

[67] T. A. Olds, S. E. Karcher, K. W. Kriegsman, X. Guo, and J. S. McCloy, "Oxidation and anion lattice defect signatures of hypostoichiometric lanthanide-doped UO2," *Journal of Nuclear Materials,* vol. 530, p. 151959, 2020/03/01/ 2020.

[68] J. Martinez, N. Clavier, A. Mesbah, F. Audubert, X. F. Le Goff, N. Vigier*, et al.*, "An original precipitation route toward the preparation and the sintering of highly reactive uranium cerium dioxide powders," *Journal of Nuclear Materials,* vol. 462, pp. 173-181, 2015/07/01/ 2015.

[69] T. Cordara, "Effect of the presence of fission products on the dissolution mechanisms of model compounds based of uranium dioxide. Effet de la présence de produits de fission sur les mécanismes de dissolution de composés modèles à base de dioxyde d'uranium," Université Montpellier, France 2017.

[70] C. Poinssot, P. Toulhoat, J. P. Grouiller, J. Pavageau, J. P. Piron, M. Pelletier*, et al.*, "Synthesis on the long term behavior of the spent nuclear fuel," in *CEA Rapport*. vol. I, CEA, Ed., ed: CEA, 2001.

[71] F. Tocino, "Contrôle microstructural des reactions rédox à l'interface solide/solution lors de la dissolution d'oxydes mixtes à base d'uranium (IV)," Univ Montpellier, France, 2015.

[72] E. Giffaut, M. Grivé, P. Blanc, P. Vieillard, E. Colàs, H. Gailhanou*, et al.*, "Andra thermodynamic database for performance assessment: ThermoChimie," *Applied Geochemistry,* vol. 49, pp. 225-236, 2014/10/01/ 2014.

[73] T. Barral, L. Claparede, R. Podor, and N. Dacheux, "Understanding the solid/liquid interface evolution during the dissolution of Nd-doped UO2 by macro-/microscopic dual approach," *Corrosion Science,* vol. 222, p. 111380, 2023/09/01/ 2023.

[74] M. Massonnet, L. Claparede, J. Martinez, P. M. Martin, M. Hunault, D. Prieur*, et al.*, "Influence of Sintering Conditions on the Structure and Redox Speciation of Homogeneous (U,Ce)O(2+δ) Ceramics: A Synchrotron Study," *Inorg Chem,* vol. 62, pp. 7173-7185, May 15 2023.

[75] T. Barral, "Etude multiparamétrique de la dissolution d'oxydes mixtes (U,Ln)O2 en milieu nitrique : impact de la composition et de la microstructure", PhD thesis.," Chimie Séparative Matériaux et Procédés, Institut De Institut Chimie Séparative De Marcoule (ICSM), University of Montpellier, France, 2023.

[76] T. Cordara, S. Szenknect, R. Podor, V. Trillaud, L. Claparede, X. Le Goff*, et al.*, "Microstructural evolution of UO2 pellets containing metallic particles of Ru, Rh and Pd during dissolution in nitric acid solution: 3D-ESEM monitoring," *Hydrometallurgy,* vol. 188, pp. 182-193, 2019/09/01/ 2019.

[77] T. Kaczmarek, S. Szenknect, L. Claparède, M. Cabié, X. Le Goff, A. Mesbah*, et al.*, "Impact of ruthenium metallic particles on the dissolution of UO2 in nitric acid," *NPJ Materials Degradation,* vol. 6, p. 39, 2022/05/03 2022.

[78] M. K. Pagoaga, D. E. Appleman, and J. M. Stewart, "Crystal structures and crystal chemistry of the uranyl oxide hydrates becquerelite, billietite, and protasite," *American Mineralogist,* vol. 72, pp. 1230-1238, 1987.

[79] J. R. Bartlett and R. P. Cooney, "On the determination of uranium • oxygen bond lengths in dioxouranium(VI) compounds by Raman spectroscopy," *Journal of Molecular Structure,* vol. 193, pp. 295-300, 1989/02/01/ 1989.

[80] P. G. Lucuta, R. A. Verrall, H. Matzke, and B. J. F. Palmer, "Microstructural features of SIMFUEL - Simulated high-burnup UO_2-based nuclear fuel," *Jounal of Nuclear Materials,* vol. 178 pp. 48-60, 1991.

[81] V. Tyrpekl, M. Naji, M. Holzhäuser, D. Freis, D. Prieur, P. Martin*, et al.*, "On the Role of the Electrical Field in Spark Plasma Sintering of UO2+x," *Scientific Reports,* vol. 7, p. 46625, 2017/04/19 2017.

[82] E. De Bona, K. Popa, O. Walter, M. Cologna, C. Hennig, A. C. Scheinost*, et al.*, "Oxidation of Micro- and Nanograined UO2 Pellets by In Situ Synchrotron X-ray Diffraction," *Inorganic Chemistry,* vol. 61, pp. 1843-1850, 2022/01/31 2022.

[83] R. Caprani, P. Martin, D. Prieur, J. Martinez, M. O. J. Y. Hunault, F. Lebreton*, et al.*, "Fission products speciation in nuclear fuel: Synthesis and characterisation of mixed oxide (U,Pu)O2 SIMfuel," *Journal of Nuclear Materials,* vol. 585, p. 154607, 2023/11/01/ 2023.

[84] C. L. Gall, "Contribution to the study of fission products release from nuclear fuels in severe accident conditions : effect of the pO_2 on Cs, Mo and Ba speciation," Université Grenoble Alpes, 2018.

[85] E. De Bona, L. Balice, L. Cognini, M. Holzhäuser, K. Popa, O. Walter*, et al.*, "Single-step, high pressure, and two-step spark plasma sintering of UO2 nanopowders," *Journal of the European Ceramic Society,* vol. 41, pp. 3655-3663, 2021/06/01/ 2021.

[86] L. Desgranges, G. Baldinozzi, G. Rousseau, J.-C. Nièpce, and G. Calvarin, "Neutron Diffraction Study of the in Situ Oxidation of UO2," *Inorganic Chemistry,* vol. 48, pp. 7585-7592, 2009/08/17 2009.

[87] L. Quémard, L. Desgranges, V. Bouineau, M. Pijolat, G. Baldinozzi, N. Millot*, et al.*, "On the origin of the sigmoid shape in the UO2 oxidation weight gain curves," *Journal of the European Ceramic Society,* vol. 29, pp. 2791-2798, 2009/10/01/ 2009.

[88] G. Leinders, "Low-temperature oxidation of fine UO_2 powders," KU Leuven, Belgium, 2016.

[89] D. Horlait, N. Clavier, N. Dacheux, R. Cavalier, and R. Podor, "Synthesis and characterization of Th1−xLnxO2−x/2 mixed-oxides," *Materials Research Bulletin,* vol. 47, pp. 4017-4025, 2012/12/01/ 2012.

[90] N. Clavier, Y. Cherkaski, J. Martinez, S. Costis, T. Cordara, F. Audubert*, et al.*, "Synthesis and Direct Sintering of Nanosized (MIV,MIII)O2-x Hydrated Oxides as Electrolyte Ceramics," *Chem Phys Chem,* vol. 18, pp. 2666-2674, 2017.

[91] J. F. Ziegler, M. D. Ziegler, and J. P. Biersack, "SRIM – The stopping and range of ions in matter (2010)," *Nuclear Instruments and Methods in Physics Research Section B: Beam Interactions with Materials and Atoms,* vol. 268, pp. 1818-1823, 2010/06/01/ 2010.

[92] J. Soullard, "Mise en evidence de boucles de dislocation imparfaites dans des echantillons de bioxyde d'uranium irradies," *Journal of Nuclear Materials,* vol. 78, pp. 125-130, 1978/11/01/ 1978.

[93] P. Hautojärvi and C. Corbel, "Positron Spectroscopy of Defects in Metals and Semiconductors," in *Proceedings of the International School of Physics "Enrico Fermi"*, 1995, pp. 491 - 532.

[94] P. Desgardin, L. Liszkay, M. F. Barthe, L. Henry, J. Briaud, M. Saillard, *et al.*, "Slow Positron Beam Facility in Orléans," *Materials Science Forum,* vol. 363-365, pp. 523-525, 2001.

[95] T. Schwarz, A. Redinger, S. Siebentritt, Z. Peng, B. Gault, D. Raabe, *et al.*, "Variable chemical decoration of extended defects in Cu-poor $Cu_2ZnSnSe_4$ thin films," *Physical Review Materials,* vol. 3, p. 035402, 03/19/ 2019.

[96] H. Labrim, M. F. Barthe, P. Desgardin, T. Sauvage, G. Blondiaux, C. Corbel, *et al.*, "Vacancy defects induced in sintered polished UO2 disks by helium implantation," *Applied Surface Science,* vol. 252, pp. 3256-3261, 2006/02/28/ 2006.

[97] F. Chamssedine, T. Sauvage, and S. Peuget, "DIADDHEM set-up: New IBA facility for studying the helium behavior in nuclear glasses," *Nuclear Instruments and Methods in Physics Research Section B: Beam Interactions with Materials and Atoms,* vol. 268, pp. 1862-1866, 2010/06/01/ 2010.

[98] R. Mohun, L. Desgranges, C. Jégou, B. Boizot, O. Cavani, A. Canizarès, *et al.*, "Quantification of irradiation-induced defects in UO2 using Raman and positron annihilation spectroscopies," *Acta Materialia,* vol. 164, pp. 512-519, 2019/02/01/ 2019.

[99] Y. Ma, "A study of point defects in UO_{2+x} and their impact upon fuel properties," Materials Science, Université Aix-Marseille, Marseille, France, 2017.

[100] H. Labrim, M. F. Barthe, P. Desgardin, T. Sauvage, G. Blondiaux, C. Corbel, *et al.*, "Thermal evolution of vacancy defects induced in sintered UO2 disks by helium implantation," *Applied Surface Science,* vol. 252, pp. 3262-3268, 2006/02/28/ 2006.

[101] A. Canizarès, "Spectroscopie de diffusion Raman en conditions extrêmes," Techniques de l'Ingénieur Editions T.I., 2013.

[102] G. Guimbretière, L. Desgranges, A. Canizarès, G. Carlot, R. Caraballo, C. Jégou, *et al.*, "Determination of in-depth damaged profile by Raman line scan in a pre-cut He2+ irradiated UO2," *Applied Physics Letters,* vol. 100, p. 251914, 2012.

[103] L. Desgranges, G. Baldinozzi, P. Simon, G. Guimbretière, and A. Canizares, "Raman spectrum of U4O9: a new interpretation of damage lines in UO2," *Journal of Raman Spectroscopy,* vol. 43, pp. 455-458, 2012.

[104] Y. Wang, D. C. Alsmeyer, and R. L. McCreery, "Raman Spectroscopy of Carbon Materials: Structural Basis of Observed Spectra," *Chemistry of Materials,* vol. 2, pp. 557-563, 1990.

[105] M. Marton, M. Vojs, E. Zdravecká, M. Himmerlich, T. Haensel, S. Krischok, *et al.*, "Raman Spectroscopy of Amorphous Carbon Prepared by Pulsed Arc Discharge in Various Gas Mixtures," *Journal of Spectroscopy,* vol. 2013, p. 467079, 2012/11/25 2013.

[106] E. F. Sheka, Y. A. Golubev, and N. A. Popova, "Graphene Domain Signature of Raman Spectra of sp2 Amorphous Carbons," *Nanomaterials,* vol. 10, p. 2021, 2020.

[107] L. Desgranges, Y. Pontillon, P. Matheron, M. Marcet, P. Simon, G. Guimbretière, *et al.*, "Miscibility Gap in the U–Nd–O Phase Diagram: a New Approach of Nuclear Oxides in the Environment?," *Inorganic Chemistry,* vol. 51, pp. 9147-9149, 2012/09/03 2012.

[108] Z. Talip, T. Wiss, A. Janssen, J. Y. Colle, J. Somers, and R. J. M. Konings, "The dissolution of helium in La-doped UO2 as a surrogate of hypo-stoichiometric UO2," *Nuclear Materials and Energy,* vol. 3-4, pp. 12-16, 2015/07/01/ 2015.

[109] E. Iglesias and J. Quiñones, "Analogous materials for studying spent nuclear fuel: The influence of particle size distribution on the specific surface areaof irradiated nuclear fuel," *Applied surface science,* vol. 254, pp. 6890–6896, 2008.

[110] J. S. Anderson, L. E. J. Roberts, and E. A. Harper, "The oxides of uranium. Part VII. The oxidation of uranium dioxide," *Journal of the Chemical Society (Resumed),* pp. 3946-3959, 1955.

[111] S. Aronson, R. Roof, and J. Belle, "Kinetic Study of the Oxidation of Uranium Dioxide," *The Journal of Chemical Physics,* vol. 27, pp. 137-144, 1957.

[112] R. E. Einziger and J. A. Cook, "Behavior of Breached Light Water Reactor Spent Fuel Rods in Air and Inert Atmospheres at 229°C," *Nuclear Technology,* vol. 69, pp. 55-71, 1985.

[113] R. E. Einziger and R. V. Strain, "Behavior of breached PWR spent-fuel rods in an air atmosphere between 250ºC and 360ºC," *Nuclear Technology,* vol. 75, pp. 82-95, 1986.

[114] B. Hanson, "The burnup dependence of light water reactor spent fuel oxidation," Pacific Northwest National Laboratory, Richland, Washington 993521998.

[115] G. Leinders, J. Pakarinen, R. Delville, T. Cardinaels, K. Binnemans, and M. Verwerft, "Low-Temperature Oxidation of Fine UO2 Powders: A Process of Nanosized Domain Development," *Inorganic Chemistry,* vol. 55, pp. 3915-3927, 2016/04/18 2016.

[116] G. Leinders, T. Cardinaels, K. Binnemans, and M. Verwerft, "Low-Temperature Oxidation of Fine UO2 Powders: Thermochemistry and Kinetics," *Inorganic Chemistry,* vol. 57, pp. 4196-4204, 2018/04/02 2018.

[117] *Durability of Spent Nuclear Fuels and Facility Components in Wet Storage*. Vienna: INTERNATIONAL ATOMIC ENERGY AGENCY, 1998.

[118] J. Johnson, A. B., "Behavior of spent nuclear fuel in water pool storage," United States1977.